

Probing Many Body Effects in Semiconductor  
Nanostructures

A thesis presented

by

Ron M. Potok

to

The Department of Physics

in partial fulfillment of the requirements

for the degree of

Doctor of Philosophy

in the subject of

Physics

Harvard University

Cambridge, Massachusetts

January 2006

© 2005 by Ron M. Potok

All rights reserved.

Thesis Advisors:

Author:

Charles M. Marcus

Ron M. Potok

David Goldhaber-Gordon

# Probing Many Body Effects in Semiconductor Nanostructures

## Abstract

This thesis describes two sets of experiments performed in quantum dots and quantum point contacts fabricated in *GaAs/AlGaAs* 2D electron gases. First, we investigate the role of interactions in determining the ground state of a quantum dot. Transport spectroscopy reveals both spin-increasing and spin-decreasing transitions, as well as higher-spin ground states. We then compare ground and excited state transport spectroscopy to direct measurements of the spin polarization of emitted current by developing the first mesoscopic spin polarizer/analyzer system using spin-selective transverse electron focusing.

A transverse electron focusing geometry is used to couple current from an emitter (either a quantum point contact or quantum dot) into a collector point contact. In a magnetic field, the collector point contact can be biased to transmit only a single spin, which allows a direct measure of spin polarization of the current incident on it. Spin polarization of  $> 70\%$  is found for a quantum point contact, while the spin of emitted current in the Coulomb blockade regime of a quantum dot is found to be polarized along the direction of the applied magnetic field regardless of the ground state spin transition.

In the second set of experiments, we realize a highly correlated electron system, the two channel Kondo system, in a specific geometry of coupled quantum dots. The two channel Kondo model, in which a local magnetic moment is screened by two *independent* conduction reservoirs, is created in a double quantum dot system based on a proposal by Oreg and Goldhaber-Gordon [1]. Using electrostatic gates we demonstrate *in situ* control of the parameters of the two channel Kondo model. We tune continuously between two distinct Fermi-liquid regimes, which are characterized by different values of conductance through the nanostructure. We investigate the properties of this quantum phase transition and the associated two channel Kondo quantum critical point.

[1] Y. Oreg and D. Goldhaber-Gordon, Physical Review Letters 90, 133602 (2003).

# Contents

<b>1</b>	<b>Introduction</b>	<b>1</b>
1.1	The many body problem and mesoscopic physics . . . . .	1
1.2	Electrons in a box . . . . .	6
1.3	A direct measurement: Spin polarizer/analyzer experiment . . . . .	10
1.4	Kondo effect . . . . .	12
1.5	Building Two Channel Kondo Physics into Semiconductor Nanostructures	16
1.6	Quantum Phase Transitions . . . . .	18
<b>2</b>	<b>Spin Measurements of GaAs Quantum Dots</b>	<b>20</b>
2.1	The Quantum Dot . . . . .	21
2.2	Spin Properties of Closed Quantum Dots . . . . .	25
2.2.1	Probing Ground State Spin Transitions . . . . .	25
2.2.2	Excited state measurements of quantum dots . . . . .	29
2.3	Focusing measurements . . . . .	32
2.3.1	Measuring Spin Polarized Current in Semiconductor Nanostructures . . . . .	32
2.3.2	Measuring Spin Polarization in Quantum Dots . . . . .	43
2.4	Future of spin in quantum dots . . . . .	45

<b>3</b>	<b>Kondo Effect in Quantum Dots</b>	<b>48</b>
3.1	Introduction to Kondo Effect . . . . .	50
3.2	Anderson Model and the Kondo effect . . . . .	53
3.3	Quantum Dots as Artificial Impurities . . . . .	57
3.4	Kondo Effect in a Three Lead Quantum Dot . . . . .	63
3.5	The Kondo Effect Out of Equilibrium . . . . .	68
<b>4</b>	<b>Background of the Single Channel and Two Channel Kondo Problem</b>	<b>74</b>
4.1	Prior Kondo Variants in Quantum Dots . . . . .	75
4.2	Properties of the Two Channel Kondo Effect . . . . .	81
4.3	Previous Experimental Work into Two Channel Kondo . . . . .	86
<b>5</b>	<b>Implementation of Two Channel Kondo Effect in Semiconductor Nanos-</b>	
	<b>tructures</b>	<b>90</b>
5.1	Proposal . . . . .	90
5.2	Implementation . . . . .	95
<b>6</b>	<b>Two-Channel Kondo Effect and Quantum Phase Transitions</b>	<b>108</b>
6.1	Observation of the Two-Channel Kondo Effect . . . . .	108
6.2	Supplementary Information for 2CK . . . . .	121
	<b>Bibliography</b>	<b>125</b>
<b>A</b>	<b>Wiring and Filtering in Oxford TLM Dilution Refrigerator</b>	<b>141</b>
A.1	Oxford TLM dilution refrigerator . . . . .	142
	A.1.1 Basics . . . . .	142
	A.1.2 Thermometry and temperature control . . . . .	142
A.2	Electronics and room temperature filtering . . . . .	143

A.2.1	DAC properties . . . . .	143
A.2.2	DAC filtering . . . . .	146
A.2.3	Measurement electronics . . . . .	150
A.2.4	Breakout box . . . . .	153
A.2.5	Shielding at room temperature . . . . .	154
A.3	Low temperature wiring and filtering . . . . .	155
A.3.1	Oxford wiring . . . . .	155
A.3.2	PC board mounted RC filters . . . . .	155
A.3.3	Resistive coax filters . . . . .	157
A.3.4	Chip carrier and socket and the presence of magnetic materials .	159
A.3.5	Shielding in the refrigerator . . . . .	161
A.3.6	Building the coldfinger . . . . .	161
A.3.7	Measurement details . . . . .	164
A.3.8	Coulomb blockade thermometry . . . . .	165
A.4	Appendix references . . . . .	165

# List of Figures

1.1	Basic Fermi Liquid Theory . . . . .	5
1.2	Drawing of basic devices . . . . .	7
1.3	Filling electrons into a box . . . . .	8
1.4	Spin orbit coupling in GaAs . . . . .	10
1.5	Filling in a magnetic field . . . . .	11
1.6	Transverse electron focusing geometry . . . . .	12
1.7	Quantum dot as an artificial magnetic impurity . . . . .	14
1.8	Kondo effect . . . . .	14
1.9	Two channel Kondo effect . . . . .	17
1.10	Phase diagram of a High $T_c$ superconductor . . . . .	19
1.11	Phase diagram for 2CK Hamiltonian . . . . .	19
2.1	<i>GaAs/AlGaAs</i> 2D electron gas . . . . .	21
2.2	SEM image of quantum dot . . . . .	22
2.3	Constant interaction model . . . . .	24
2.4	Ground state spin of a quantum dot . . . . .	28
2.5	Nonlinear transport in quantum dots . . . . .	29
2.6	Excited spin states in quantum dots . . . . .	31
2.7	Measuring spin polarization in ballistic nanostructures . . . . .	34

2.8	Magnetic field and temperature dependence of spin polarized current from a QPC . . . . .	39
2.9	Spin polarization as a function of QPC conductance . . . . .	41
2.10	Focusing from a quantum dot . . . . .	44
2.11	Spin polarization of current emitted from a quantum dot . . . . .	46
3.1	Resistivity of metals with magnetic impurities . . . . .	50
3.2	Possible charge configurations of the Anderson impurity model . . . . .	54
3.3	$2^{nd}$ order perturbation processes in the Anderson model. . . . .	55
3.4	Drawing of increased scattering at low temperature due to Kondo effect. . . . .	56
3.5	Quantum dot and the Anderson model . . . . .	58
3.6	Kondo effect in a quantum dot . . . . .	59
3.7	Kondo effect out of equilibrium . . . . .	63
3.8	Conductivity of a three lead quantum dot . . . . .	66
3.9	Single valued $T_K$ in a three lead quantum dot . . . . .	67
3.10	Kondo effect in a three lead quantum dot . . . . .	70
3.11	Measuring the out of equilibrium DOS of the Kondo effect . . . . .	71
3.12	Calculation of Enhanced Density of States . . . . .	73
4.1	Exotic Kondo effects in quantum dot devices . . . . .	75
4.2	Local degeneracy and the Kondo effect . . . . .	77
4.3	Local degeneracy and the Kondo effect . . . . .	79
4.4	RKKY interaction in quantum dots . . . . .	80
4.5	Multichannel Kondo effect . . . . .	83
4.6	Probing the out of equilibrium properties of 2CK . . . . .	85
4.7	Phase diagram of 2CK . . . . .	86

4.8	Local degeneracy in a narrow metal constriction . . . . .	87
4.9	Possible realization of 2CK effect in narrow metal constrictions . . . . .	88
4.10	Possible realization of 2CK effect in certain heavy Fermion materials . . . . .	89
5.1	Drawing of Matveev's original proposal for 2CK behavior in nanostructures. . . . .	91
5.2	Oreg and Goldhaber-Gordon's 2CK proposal in quantum dots . . . . .	92
5.3	Energetics of a 2CK system in quantum dots . . . . .	93
5.4	Coulomb blockade at finite temperature . . . . .	96
5.5	Charging energy and energy level spacing of a quantum dot as a function of area . . . . .	97
5.6	Selecting the size of the finite reservoir . . . . .	98
5.7	SEM images of the devices to implement 2CK . . . . .	99
5.8	Thouless and quantum dots, $\Gamma/\Delta$ . . . . .	100
5.9	Double quantum dot charge stability diagram . . . . .	102
5.10	Parameters of the antiferromagnetic coupling constants . . . . .	104
5.11	Calculation of 2CK physics in a double quantum dot . . . . .	105
5.12	Effects of finite $\Delta J$ and temperature . . . . .	107
6.1	2CK in quantum dots . . . . .	112
6.2	Artificial magnetic impurity . . . . .	114
6.3	Formation of two independent 1CK states . . . . .	116
6.4	Energy dependence of Kondo effect . . . . .	118
6.5	2CK effect . . . . .	120
6.6	$T_K$ of the small quantum dot . . . . .	123
6.7	Conductance of double dot system . . . . .	124

6.8	Scaling of 1CK . . . . .	125
A.1	Fridge circuit . . . . .	145
A.2	Photographs of setup for DACs . . . . .	147
A.3	Feedthrough filter . . . . .	147
A.4	High and low Harvard filter . . . . .	148
A.5	Harvard filter . . . . .	149
A.6	60 Hz filter and divider . . . . .	149
A.7	Photographs of measurement circuit . . . . .	151
A.8	AC + DC adder box . . . . .	151
A.9	Breakout box switch . . . . .	154
A.10	PC board filter . . . . .	156
A.11	PC board filter attenuation . . . . .	157
A.12	Resistive coax cable . . . . .	158
A.13	Building the pc board . . . . .	162
A.14	Coax connectors . . . . .	162
A.15	Attaching the coax to the pc board . . . . .	163
A.16	Putting the finished pcboards onto the pentagon . . . . .	163
A.17	Wrapping the coaxial cable . . . . .	163
A.18	Model circuit . . . . .	165
A.19	CB peak temperature . . . . .	166

# List of Tables

A.1	Heater power . . . . .	143
A.2	Attenuation of resistive coax . . . . .	159
A.3	Wiring of dilution refrigerator . . . . .	160

# Papers and Publications

R. M. Potok, I.G. Rau, D. Goldhaber-Gordon, and H. Shtrikman, “Observation of the Two-Channel Kondo Effect”, in preparation (2006).

R.M. Potok and D. Goldhaber-Gordon, “Nanotechnology: New spin on correlated electrons”, *Nature* **434**, 451 (2005).

S. K. Watson, R. M. Potok, C. M. Marcus, and V. Umansky, “Experimental Realization of a Quantum Spin Pump”, *Phys. Rev. Lett.* **91**, 258301 (2003).

R. M. Potok, J. A. Folk, C. M. Marcus, V. Umansky, M. P. Hansen, A. C. Gossard, “Spin and Polarized Currents from Coulomb Blockaded Quantum Dots”, *Phys. Rev. Lett.* **91**, 016802 (2003).

J. A. Folk, R. M. Potok, C. M. Marcus, and V. Umansky, “A Gate-Controlled Bidirectional Spin Filter Using Quantum Coherence”, *Science* **299**, 679 (2003).

R. M. Potok, J. A. Folk, C. M. Marcus, and V. Umansky, “Detecting Spin Currents in Ballistic Nanostructures”, *Phys. Rev. Lett.* **89**, 266602 (2002).

## Acknowledgements

My term as a Ph.D. student at Harvard and Stanford University was very intense and full of marvel and discovery. I crossed paths with many fine people and I hope the words below convey a little of the depth of my gratitude to them.

First and foremost I would like to thank my advisors, Professor Charlie Marcus and Professor David Goldhaber-Gordon. I had the unique opportunity to work with *two* excellent experimentalists during my Ph.D., which has benefitted me in more ways than I can express here.

I began my research in Charlie's lab the day I arrived at Harvard in September of 2000. It happened that day the lab also arrived from Stanford University. With Charlie's leadership, the lab was constructed and the measurement apparatus was operational in time to submit abstracts for March meeting - an amazing accomplishment.

The most valuable lesson I learned from Charlie was how to run an experiment. If ever there was an experimental problem, Charlie would have a solution. Under his guidance, I learned how to remain on task with the experiment at hand. Almost daily, he posed exact questions for me to answer about an experiment. If I did not have the answer yet, he would insist the experiment answer the question in a timely manner. I was never lost under his guidance - there was always a goal in taking a piece of data. This was an amazingly powerful asset to have when I began the second set of experiments at Stanford, which had a larger set of possibilities that I could have imagined. His training enabled me to be successful in lab.

Charlie also built a unique lab with the graduate students he hired. My fondest memories of my time at Harvard were working out new experiments on a whiteboard late at night in the coffee room, many times with Charlie present. Charlie truly motivated his lab members to learn from each other by talking about physics. This created

a unique environment in lab - although intense, I learned more physics in those two years than I could have ever imagined. Charlie also constantly brought visitors to the coffee room to bring us new perspectives on physics. I feel I need to say again what an amazing two years that was. In addition, even while I was at Stanford, Charlie has always been supportive - something I truly appreciate.

My learning was also guided substantially by a more experienced graduate student at Harvard, Josh Folk. Josh is an amazing friend and truly a fantastic experimentalist. His guidance over the last five years has effected me more than any other single person.

It was a pleasure to work with all graduate students in Charlie's lab, especially Alex Johnson, Jeff Miller, Heather Lynch, Sara Cronenwett, Dominik Zumbuhl, Andrew Houck, Leo DiCarlo, Edward Laird, and Mike Biercuk. The postdocs were also amazing, Douwe Monsma and Nadya Mason, along with a Junior Fellow I spent a bit of time with, David Goldhaber-Gordon. In addition, the first experiment I ran at Harvard was in collaboration with Leo Kouwenhoven while he was on sabbatical from Delft University. I also benefited greatly from conversations with the Westervelt lab and the Tinkham lab. At the time, I had no idea how lucky I was to learn from such great experimentalists.

By the time I moved to Stanford to begin a new experiment in David Goldhaber-Gordon's lab, Charlie had prepared me to take on any experimental challenge. In fact, I needed everything I learned from Charlie accomplish the next set of experiments. Without that two years, I am confident I would not have been able to accomplish the experiments at Stanford in a timely manner.

Working with David Goldhaber-Gordon for the second half of my Ph.D. has been truly great. I knew from my interactions with him at Harvard that he was a great experimentalist, but he has also become a great advisor during my time at Stanford.

He challenged me in new ways – both experimentally and theoretically. David was always excited about completely thinking through a problem. In his lab, he allowed me to take over an experiment from the beginning and carry it through to the end. Working with him on the two channel Kondo experiments changed me as a person, giving me the confidence to overcome any challenge. I truly appreciate that.

In David's lab, I attempted to mentor a graduate student, Ileana Rau, in much the same manner Josh Folk did for me. I truly enjoyed working with such a bright and talented young physicist, and I can only hope I inspired you half as much as Josh inspired me. I also enjoyed working with Lindsay Moore, Charis Quay, Greg Tseng, Hungtao Chou, Silvia Folk, and Mark Topinka who were in the lab when I started at Stanford. Also, the newer group of graduate students have truly inspired me, Joey Sulpizio, Mike Jura, and Ileana. I also had the pleasure of working with two other postdocs at Stanford, John Cummings and Mike Grobis. Mike, in particular, joined only in the last few months of my tenure, but we had many enlightening and fun conversations. Working together with Ileana, I expect many more interesting results on the Kondo effect from them.

I would also like to mention the others in the McCullough basement who helped me in many ways, but in particular Ophir Auslaender, Nick Koshnick, Hendrick Bluhm, Rafael Dinner, Clifford Hicks, and Myles Steiner (although the entire Moler Lab and KGB lab were always helpful).

Throughout my time at Stanford, I have collaborated with a number of graduate students and faculty in order to understand the theory of the two channel Kondo physics. Most of all, I would like to thank Avi Schiller for his insight into this experiment. In addition, Fritjof Anders, Eran Lebanon, Yuval Oreg, and Leonid Glazman have enlightened me with a number of useful discussions.

Also, in building the electronics and wiring for the dilution refrigerator, I received helpful advice from Andre Kogan and Keith Schwab.

Special thanks are due to my committee, Bert Halperin, Michael Tinkham and Hongkun Park, with whom it was a pleasure to discuss science. Also, the Harvard staff, especially Sheila Ferguson, Kathy Ryan, and David Norcross, deserve special thanks for taking care of the many details involved in pursuing my PhD at two universities.

All of my studies at Harvard and Stanford, though, would have been impossible without the faith my undergraduate research advisor, John Keto, at the University of Texas at Austin had in me. He gave me this opportunity. In addition, Mel Oakes gave me constant encouragement while serving as my undergraduate academic advisor. Without these two people, I would have never made it this far.

Finally, special thanks to all my family and friends for constant support. In my time at Harvard, I made many friends which made Harvard such an enjoyable place to learn, including Ross Perak, Aaron Handler, Jae Hur, Bill Anderson, Ryan Barnett, Bola George, Ania Blezynski and especially my great friends from UT and Harvard, Scott Nguyen and Eric Devroe. At Stanford, I also made many great friends including Adam Edwards, John Paul Strachan, Mike Preiner, Kai Mei Fu, Nick Koshnick, Matt Pyle, Pete Santizo, Mirthala Santizo, Beth Craig, Dan Sandberg, Kevin Yarritu, Brian Foster, Nick Cizek, and Jon Schuller.

The support I could always count on came from my large family in Texas, especially my mother, father and sister. I grew up with a large extended family in Texas held together by my grandmother – truly the strongest person I have ever met, and a large extended family in Michigan. In addition, my friends in Houston have always treated me like family, and I am proud to acknowledge John Quevedo, Juice Newsom, Ryan Carey and the whole Carey family, Steve Bosze, Patrick McCabe, Mark Nierode, Stuart

Malone, Tim Wise, and Michael Cook. Without any of you, this PhD would have been impossible.

# Chapter 1

## Introduction

### 1.1 The many body problem and mesoscopic physics

How much physics is left to discover about the building block of computers, the transistor? In electronics courses, electricity is described as flowing like water through circuits. This concept leads to a variety of extremely useful predictions, such as conservation of electrical current and energy conservation (Kirchoff's laws); however, we also know that electricity comes in discrete packets, electrons. Quantum effects associated with this discreteness are even creeping into room temperature semiconductor device physics[1]. (For example, tunneling and ballistic transport are quantum phenomena.)

While the electronics industry views these phenomena as potential problems as devices decrease in size, physicists have become excited about the possibility of controlling and manipulating electron systems whose properties are at least partially or completely dominated by geometry. A new field known as mesoscopic physics has emerged. In a normal transistor, a single gate voltage is used to turn the transmittance (and thus conductance) of a single channel completely on or off. Instead, we use multiple gates in designer structures to isolate small droplets of electrons from their

conducting leads. With many gate voltages, we can then finely control each droplet's coupling to conducting leads and the coupling between the electron droplets. We then study how electrons behave in these reduced size, low dimensional structures.

In this dissertation, I report experiments which take advantage of current lithographic techniques, advances in semiconductor materials science, and the maturation of low temperature physics to study physics of the many body electron system. The true goal of this research is to help explicate Phil Anderson's statement that, "More is different"[2], especially at low energies when interactions between particles govern their position and motion.

The way in which particles arrange themselves changes as a function of many parameters, such as temperature. Phase transitions between different states are common occurrences in nature; one of the more common of these is the gas - liquid - solid transition as function of temperature. At high temperatures, a group of atoms usually can be considered as a continuous density instead of occupying discrete locations. As temperature decreases interactions become more important - atoms may find it energetically favorable to undergo a phase transition and occupy discrete sites in a lattice, as with many solids. This state is only available to a group of particles - phase transitions are a uniquely many body phenomenon where the arrangements of atoms can differ dramatically from one phase to another.

The same is true for the arrangement of the millions of electrons in solids - which have even more exotic behavior due to long range Coulomb interaction and very light mass. At the same time, as the temperature of a solid with mobile electrons (a metallic system) is lowered, quantum mechanical coherence becomes increasingly important. The combination of these trends can produce new phenomena such as the Kondo effect[3]. In fact, the importance of interactions can be tuned by a variety of different

methods. In this dissertation, I tune interactions in electron systems with the simple application of a gate voltage to a transistor.

How does a group of electrons arrange themselves? Solids are composed of electrons, protons, and neutrons, and we know the laws that govern their interaction. It is tempting to try to calculate their properties from first principles. In practice, however, this approach is completely impractical: undergraduate physics majors routinely calculate the quantum states of a hydrogen atom, but even a two-electron helium atom has only been described in detail in the last decade, and it turns out to have complex and chaotic dynamics [4].

So to calculate anything we must compromise by making approximations and simplifying assumptions. The most microscopic approach is “first principles” calculations – so-called because they are based on calculable parameters of the individual atoms in a material, and of mobile electrons. These remain unwieldy for describing typical bulk solids: calculating electron behavior in a 10 nanometer long nanotube composed of only 1000 carbon atoms is already a tour de force. These methods are also notoriously unreliable when correlations among many electrons are important.

At a greater level of abstraction, models invoke localized sites and delocalized electron reservoirs, plus transitions between these states. Interactions are treated as being relatively local: repulsion between electrons on a single site, or between near neighbors. This class of models includes such dramatic successes as the Hubbard model and the BCS theory of superconductivity (which also incorporates interactions with bosons). Nonetheless, the approach has several limitations. First, there is no good way to decide *a priori* which set of electronic states will be important in determining a particular material’s properties. Second, electrons on many sites can interact with each other, making calculations impractical. Next, real materials are not perfectly

periodic, and any physical measurement will reflect some average over a disordered ensemble of sites. Finally, the phenomenological parameters (tunneling rates, strength of interactions) are not tunable, and can be difficult even to measure precisely, making theories difficult to test. As we will see, all these limitations can be remedied using nanotechnology, allowing powerful and direct tests of the theoretical ideas at this level.

Before continuing with the physics, I would like to make a brief comment on the developments in technology and their role in new methods and materials for this type of research. In particular, in this dissertation we study high quality *GaAs/AlGaAs* structures grown by our collaborators using molecular beam epitaxy. The layer structure and dopants of this semiconductor compound are specifically designed for a near atomically perfect *GaAs/AlGaAs* interface, creating an extremely high mobility electron gas at low temperature. (Electrons can have mean free paths of 10's of micrometers.)

At low magnetic field, this electron gas behaves very nearly like an ideal electron gas. Excitations are single-particle-like, having the  $1/E^2$  lifetime predicted by Fermi liquid theory (see Fig. 1.1)[5]. The electron density in these materials yields a reasonably long Fermi wavelength and a correspondingly long screening length. (A typical Fermi wavelength is  $\sim 50nm$  for the systems studied here.) With current electron beam lithography techniques, the semiconductor can be patterned to a precision on the order of the wavelength of the conduction electrons we study, and electrons beneath the gate electrodes can be depleted by applying  $\sim 10$ 's of millivolts of gate voltage.

Finally, due to the growth of work at low temperature, the major low temperature apparatus, a dilution refrigerator, is a commercial item. The combination of collaborating with materials specialists, using current state of the art lithography techniques, and a commercial refrigerator has allowed the field of mesoscopic physics to flourish. The physics in these projects was truly enabled by new technology. (My only major

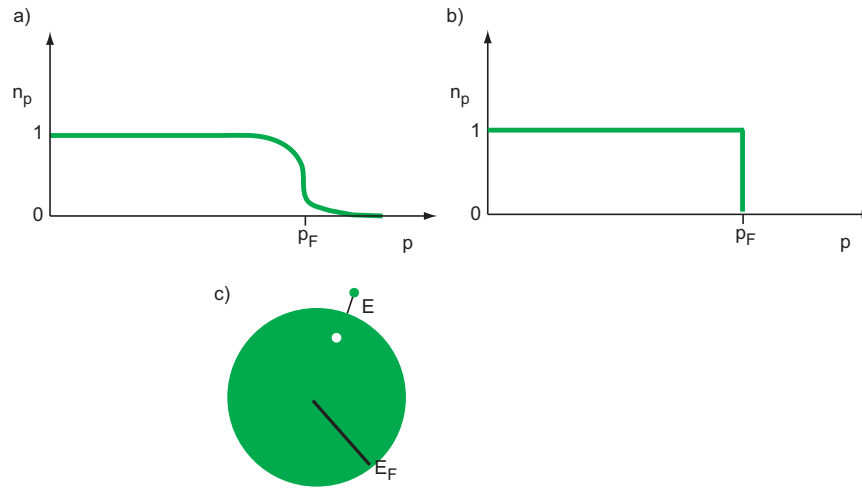


Figure 1.1: Interactions in a many-electron system dramatically effect the energy distribution of the electrons. In a metallic system (one containing mobile electrons with momentum  $p$ ), there are a variety of liquid-like phases available - electrons are still mobile, but the lowest energy configuration of particles may not be a noninteracting Fermi gas, as in (b). A more realistic distribution of interacting electrons,  $n_p$ , is shown in (a). The major modifications occur around the Fermi energy,  $E_F = p_F^2/2m$ . The energy spectrum,  $E_F(n_p)$ , is an even more complicated function. However, the simplest liquid does begin from the distribution of a noninteracting Fermi gas, (b). According to Landau Fermi liquid theory, the properties of an interacting Fermi liquid are very similar to those of an ideal degenerate Fermi gas. Landau assumed that when increasing interactions slowly to move from ideal Fermi gas to a liquid, the particles of the electron gas and excitations (quasiparticles) of the liquid have a one to one correspondence. Shown in (c) is a distribution of quasiparticles with a single excitation, energy  $E$  above the Fermi energy  $E_F$ . Though the quasiparticles will have a material dependant renormalized mass and g-factor, all Landau quasiparticles are single-particle-like and have a distinctive lifetime,  $\gamma$ , (inverse of scattering rate) which is inversely proportional to square to the distance from the Fermi surface,  $\gamma \sim 1/E^2$ .

technological accomplishment was the development of a dilution refrigerator electrical filtering and grounding system which produced electron temperatures  $T_e = 12mK$ .)

In fact, these advantages have allowed me to study how electrons arrange themselves in several experiments with two slightly different motivations. Both approaches rely on the simplicity (Fermi liquid behavior) of the underlying semiconductor.

1. I use lithography to create nanostructures to study how a group of electrons in a specific geometry arrange themselves.
2. I create a series of coupled nanostructures whose properties individually are simple and well understood. However, when coupled together in a specific manner they undergo a phase transition into a more complex state of matter, a non-Fermi liquid.

## 1.2 Electrons in a box

In the first approach (Ch. 2), we pattern the semiconductor to contain a one dimensional (1D) conducting channel (quantum point contact) or confine a group of electrons to zero dimensional (0D) box (quantum dot). In Fig. 1.2, imagine electrons (yellow) confined to a narrow sheet in the plane of the page, known as a two dimensional electron gas or 2DEG. They can then be further confined by gates (light grey) and the depletion region surrounding the gates (dark grey). (No electrons are allowed in the grey regions.) The gates can be patterned into a narrow channel, as in Fig. 1.2(a) or a confined droplet, Fig. 1.2(b). This dissertation will concentrate on the properties of the confined droplet of electrons, also known as a quantum dot. Transport measurements provide information into how electrons arrange themselves in the confining potential. In particular, we study how spin and Fermi statistics influence the confined electrons.

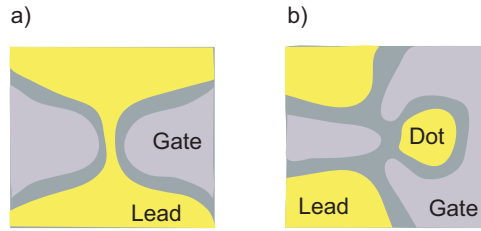


Figure 1.2: Drawing of typical devices studied in this dissertation. Electrons are contained in the yellow regions and are absent (depleted) from the grey regions. In (a), a narrow channel connects two conducting leads. In (b), two channels isolate a region of charge, or quantum dot, from the leads. The transport properties of these devices can be probed by measuring current from one lead to another (top to bottom or opposite).

Since the bulk 2D electron gas is spin degenerate, one may expect the confined region to also be spin degenerate. In Fig. 1.3(a), the naively expected filling of electrons in a box is shown. However, more complex arrangements are possible, ranging from higher spin states due to interactions or a spatial symmetries Fig. 1.3(b), or even polarization due to a Stoner instability (c)[5].

One useful parameter describing the relative importance of interactions between electrons is  $r_s$ , defined as the potential energy divided by the kinetic energy:

$$r_s = \frac{P.E.}{K.E.} = \frac{e^2 m^* r^2}{r \hbar^2} = \frac{r}{a_{Bohr}}. \quad (1.1)$$

Using the effective mass ( $m^* = 0.067m_e$ ) and bulk density for 2DEGs studied here  $n_e \sim 2 \times 10^{11}$  (determines  $r$ , the average spacing between electrons), we get a  $r_s$  of  $\sim 1$ . A higher (lower) electron density leads to a smaller (larger)  $r_s$ . At  $r_s \gg 1$ , electrons tend towards a solid lattice to minimize Coulomb interactions, known as a Wigner crystal[7, 8]. For comparison, an atom with electrons bound to a centrally symmetric central potential  $r_s \sim 1$  also. Even for this relatively low  $r_s$ , ground state for some atoms is spin polarized: degeneracy in orbital states allows the electrons to

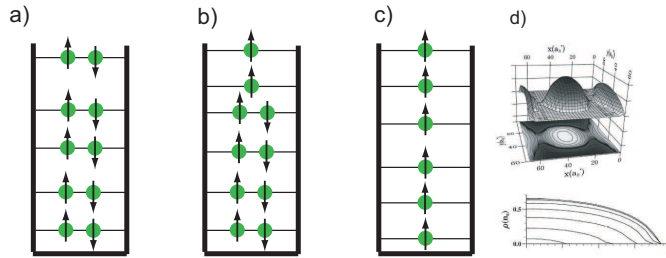


Figure 1.3: Different filling for many particles in a box. In (a), the expected filling for noninteracting spin-1/2 particles is shown. A quantized energy level spectrum exists due to confinement and spin degeneracy exists due to lack of interactions. With interactions (Coulomb repulsion for electrons) the filling can become more complicated, as shown in (b). If interactions completely dominate, states of full spin polarization are possible (c). In (d, top), a calculated density profile for a 2D box is shown (from [6]). Horizontal cuts through the quantum dot (d, bottom), show the electron density profile in the dot. Notice the density in the droplet is less than the bulk density (for this calculation,  $n_e(dot) \sim 0.5n_e(leads)$ ).

fill spin states based only on interactions.

In these devices, electric fields between the gate electrodes and the electron gas are used to confine electrons. Self consistent calculations give density profiles, as shown in Fig. 1.3(d). Notice the electron density in the dot is lower than the bulk 2DEG, indicating  $r_s$  would actually be larger in the dot than in bulk and opening the possibility for interactions play a larger role in the organization of the confined electrons. The *possibility* of probing the local density of a quantum dot has been demonstrated recently[9, 10]. In fact, it is certainly possible that reduced density in the quantum dot or the channels connecting it to the leads could lead to a completely different quantum state. Interactions could even cause a local phase transition into an intermediate phase between Wigner crystal and Fermi liquid[11].

Electron transport data presented in this dissertation indicate that interactions are important in determining the orbits of electrons filling a potential. In a quantum dot

of  $\sim 40e^-$ , we find that both cases Fig. 1.3(a) and (b) exist. These types of filling are readily explained by random matrix theory combined with electron interactions[12]. Although interactions occasionally lift spin degeneracy, the quantum dot remains very near  $S = 0$ . This is in contrast to a potential with a few electrons, also presented here, where we only find the simplest behavior, Fig. 1.3(a).

This analysis relies on electron spin being a good quantum number in the device. If there is significant spin-orbit coupling in the device,  $H_{s.o.} = \kappa L \cdot S$ , where  $L$  is momentum operator,  $S$  is spin operator, and  $\kappa$  is the coupling, then  $J = L + S$  becomes a good quantum number. Spin-orbit coupling is known to exist in *GaAs*, from bulk measurements  $g = -0.44$  instead of 2 (which have now been observed in low dimensional *GaAs* devices also [13]). (Spin orbit coupling causes the electronic energy levels not to be purely spin-up or spin-down, and thus they reduce the g-factor for Zeeman splitting below the free-electron value of 2.) Recently, spin-orbit coupling in *GaAs* 2DEGs has been extensively studied[14, 15]. One signature of spin orbit coupling in transport is weak antilocalization (maximum of conductance at zero magnetic field) as opposed to weak localization (minimum conductance at zero magnetic field), as shown in Fig. 1.4. At the electron densities studied in this dissertation,  $n_e \sim 2 \times 10^{11}e^-/cm^2$ , spin orbit coupling is expected to be a small perturbation, so spin is expected to be a good quantum number. (At low density, the Fermi velocity is lower, thus  $L$  is smaller.) All data presented here are consistent with this assumption.

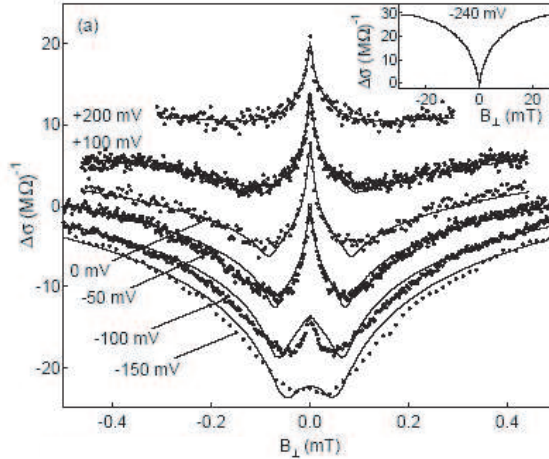


Figure 1.4: From [15]. Weak localization and antilocalization in a *GaAs* 2DEG for a range of gate voltages. At high electron density (positive gate voltage) spin orbit interaction becomes relevant, causing enhanced conductance at zero magnetic field. As the density is lowered, spin orbit interaction becomes less important and the peak in conductance at zero magnetic field turns into suppressed conductance due to weak localization.

### 1.3 A direct measurement: Spin polarizer/analyzer experiment

Given the relatively simple filling of quantum dots (Fig. 1.3) and small spin-orbit coupling, we should be able to predict the spin of an electron transmitted through a quantum dot. In a magnetic field, the states in Fig. 1.3 will split according to the Zeeman effect,  $H_Z = g\mu B_\perp \cdot S$ , where  $\mu$  is the Bohr magneton and  $B_\perp$  is the magnetic field, according to Fig. 1.5. At low energy, transport occurs only via the highest occupied state, (see Section 2.1). (In Fig. 1.5, we predict only spin up electrons will be transmitted.)

I present the first spin polarizer/analyzer experiment based on semiconductor nanostructures in Section 2.3.1 to directly measure the spin of electrons emitted from quan-

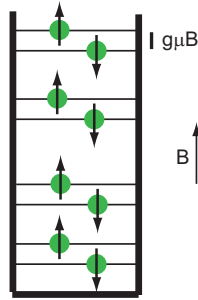


Figure 1.5: Filling of a spin degenerate quantum dot (as in Fig. 1.3(a)) in a magnetic field,  $B_{\perp}$ . The energy levels are split by the Zeeman energy,  $E_Z = g\mu B_{\perp}$ , where  $g$  is the g-factor and  $\mu$  is the Bohr magneton. For *GaAs*, the g-factor is negative, so we adopt the convention that spin down is lower in energy.

tum dots. We adapt a common technique to measure effective mass of carriers in metals known as transverse electron focusing [16, 17]. In the geometry shown in Fig. 1.6, electrons can be bent and focused from the emitter to the collector with the application of a magnetic field. (The magnetic field,  $B$ , affects the trajectory of the electrons through the Lorentz force,  $F = ev_F \times B$ , where  $e$  is the charge of the electron.) At the magnetic fields  $B_{\perp} = \frac{nm^*v_F}{se}$  ( $n$  integer and the distance between emitter and collector is  $2s$ ) and when  $s \ll l_{el}$  (mean free path  $l_{el}$ ), electrons will be ballistically injected into the collector region. If the collector is then made to be spin selective, the number of electrons injected into the collector provides a bound for the polarization of electrons leaving the emitter[18].

These measurements indicate a more complex picture needs to be formed for the filling of quantum dots[13]. A simple behavior corresponding to alternating spin up and spin down electrons is not observed. In fact, in our data set, the dot was never observed to emit electrons with spin aligned with the field (higher energy spin,  $g$  factor is negative). These measurements have not been explained nor has anyone to our knowledge attempted to reproduce them.

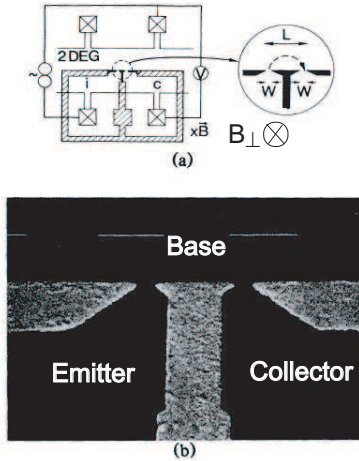


Figure 1.6: From [19]. Original electron focusing experiment in *GaAs* heterostructure. Electrons are bent and focused from the emitter to collector by a magnetic field out of the page.

Although these measurements possibly complicate the picture of transport through the quantum dot, other types of measurements, including our own, indicate a relatively simple behavior of spin in a *GaAs* quantum dot [20, 21].

Furthermore, many experiments which require both simple spin transport and relatively simple filling have now been performed. Perhaps the most extensively studied phenomenon in this realm is the Kondo effect in *GaAs* quantum dots, a complex many body effect first discovered in metals in the 1900's. In most cases, the Kondo effect involves conduction electrons coherently screening a local spin degenerate state.

## 1.4 Kondo effect

A grand challenge in correlated electron systems is to build experimental realizations of arbitrary interesting Hamiltonians. Materials physicists have long approached this problem by tailoring complex materials to realize Hamiltonians of known theoretical interest [22]. This approach is very successful and important, but suffers from several

limitations. Parameter values such as the energy of localized states or the coupling between adjacent sites are often varied only in discrete steps by changing a material's structure or chemical composition. (The main continuous parameters used are magnetic field and pressure.) *Every* parameter changes with any given change in structure, so an individual parameter is not usually tunable independent of the rest. Often only one or a few sets of parameter values can be achieved without totally changing the effective Hamiltonian. In consequence, some quantum phase transitions are manifested as one material in one phase and another related material in another phase: suggestive but not as revealing as tuning a parameter through the transition. For the same reason, one often cannot sit right at a quantum phase transition, where interesting behavior might occur. Worse still, absolute parameter values are often hard to measure precisely, making quantitative connection between theory and experiment tenuous.

But changing material composition is not the only way to vary physical properties. Recently, it has been recognized an arbitrary geometry of semiconductor droplets can provide the same physics as complex and exotic materials [23, 24, 25]. As opposed to exotic materials, the underlying semiconductor, *GaAs* in this case, has simple and well-understood properties (also assume the physics of *GaAs* quantum dots is simple, as discussed in Chapter 2).

Using lithography, one can create arbitrary and controllable barriers between an island of electrons and its reservoirs. For example, imagine creating an island containing a single electron, as in Fig. 1.7. The localized electron has a spin, which looks like a tiny magnet. At low temperature, the spin of the localized moment is screened by the surrounding conduction electrons via the Kondo effect, as in Fig. 1.8 (also Chapter 3). As temperature is reduced, the combined magnetic impurity and metal system goes from a paramagnetic state at high temperature to a nonmagnetic state

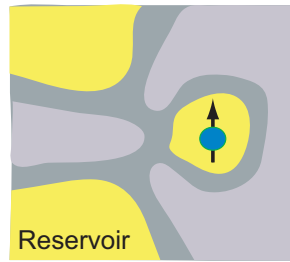


Figure 1.7: A quantum dot containing a single electron. The spin-1/2 electron is coupled to electrical leads (yellow top left and bottom left) which act as reservoirs of electrons.

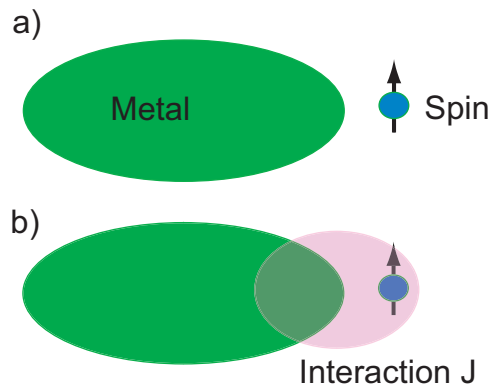


Figure 1.8: In the Kondo effect, a localized magnetic moment or spin, blue, exists in or near a reservoir of electrons, such as a metal, green. Through an interaction ( $J$ , pink) the magnetic moment is screened by the metal's conduction electrons.

at low temperature. The so-called Kondo effect, a complex many body phenomenon, dramatically affects transport through the quantum dot.

Even more exciting than the simple observation of the Kondo effect in nanostructures, the control and tunability of nanostructures has allowed the nature of the Kondo effect to be studied in new ways and with unprecedented precision. Previously, the Kondo effect was studied in bulk samples with many millions of uncorrelated magnetic impurities. Thermodynamic quantities, such as susceptibility and specific heat, indicated a transition from a magnetic state to a nonmagnetic state [26].

A phenomenological model (the Kondo model) successfully accounted for the thermodynamic and transport properties [3]. However, this model contained no information of the nature of the interaction or its dependencies on underlying material properties. More microscopic models were necessary - theories which have as their fundamental constituents electrons with Coulomb interactions.

The Anderson model provided this for the Kondo effect[27]. Fundamentally, this model contains delocalized (conduction) and localized (magnetic impurity) electrons and transitions between the two. This level of abstraction offers much insight into the fundamental nature of the Kondo effect (see section 3.2). Although both the Kondo model and Anderson model have been explored theoretically for  $\sim 40$  years, certain aspects were left relatively untested until the advent of nanotechnology.

Single artificial magnetic impurities have now been lithographically patterned and individually studied, providing new and important insight into one of the oldest many body problems. The interaction governing the Kondo effect (between the localized electron and delocalized electrons) can be finely tuned and measured. These experiments have three main advantages over previous studies in materials:

1. A single localized site is studied.
2. Measurements can be performed out of equilibrium.
3. Many model parameters can be measured, and even tuned precisely: in the Kondo effect in quantum dots, we have fine control of the interaction  $J$  from Fig. 1.8.

Since the first tunable Kondo impurity was created experimentally[28], a variety of new and exotic Kondo systems have been fabricated artificially from semiconductors, see Chapter 3 and 4.

## 1.5 Building Two Channel Kondo Physics into Semiconductor Nanostructures

The success of these experiments has motivated the next experiment of my dissertation research: use nanolithography to carve a semiconductor into arbitrary structures of coupled electron droplets designed to match a specific Hamiltonian of interest. For my dissertation research, I have chosen to build a two channel Kondo (2CK) Hamiltonian. Local gate electrodes are then used to tune important parameters of the Hamiltonian.

At first, the 2CK effect seems very similar to the single channel Kondo (1CK) effect. In its simplest form, it involves a single magnetic impurity coupled to *two* independent reservoirs of electrons, as shown in Fig. 1.9. The two reservoirs form two independent screening channels for the magnetic impurity, hence the name. If the two independent reservoirs are equally coupled to the magnetic impurity ( $J_1 = J_2$ ), a dramatically new state is formed[29]. Most importantly, the 2CK effect exhibits non-Fermi liquid behavior – meaning the low energy excitations are collective rather than single-particle-like [30, 31]. The 2CK effect is very different from previous many body physics studied in nanostructures; with the exception of a few experiments in fractional quantum hall liquids and Luttinger liquids, the low-energy electron transport in nanostructures has always been described by Fermi liquid theory. Non-Fermi liquid behavior manifests in the lifetime of the low energy excitations - a  $1/\sqrt{E}$  energy dependence rather than  $1/E^2$  dependence of Fermi liquid theory, Fig. 1.1.

The non-Fermi liquid behavior of the 2CK effect distinguishes it from most experiments performed to date in nanostructures. However, we have multiple examples of non-Fermi liquids in “nature”: superconductors, Luttinger liquids, and Laughlin liquids to name a few. Interactions cause excitations to be collective: cooper pairs in

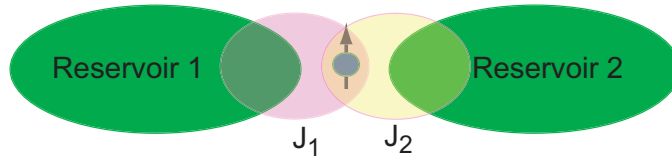


Figure 1.9: Picture of two channel Kondo effect. A single spin is coupled to two independent reservoirs of electrons, with couplings  $J_1$  and  $J_2$ .

superconductors, separate spin and charge excitations in Luttinger liquids, and fractionally charged quasiparticles in Laughlin liquids. Although qualitatively similar in complexity (often advanced quantum field theory techniques must be applied[31, 30]), each of these systems (including 2CK) have distinctive behavior making them interesting to study individually. To date, only a handful of these types of systems have been discovered theoretically, making the study of each even more worthwhile.

The 2CK effect has been proposed to explain exotic behavior of a few naturally occurring systems in nature, ranging from certain heavy Fermion compounds [32, 33] to atomic dislocations in narrow metal constrictions[34, 35] (application of the 2CK model to metal constrictions remains controversial [36]). As in previous studies of the 1CK effect, in these proposed 2CK systems many 2CK impurities exist, making quantitative predictions difficult to test.

Creating the 2CK effect in semiconductor nanostructures allows a single 2CK impurity to be studied. Perhaps more important is the ability to tune parameters of the 2CK Hamiltonian. In the previous section on Kondo effect, I mentioned that we have control of the antiferromagnetic coupling,  $J$ . Similarly, in our 2CK system, we have separate control of the interaction between one reservoir  $J_1$  and the magnetic impurity and the other reservoir and magnetic impurity  $J_2$  from Fig. 1.9[23].

## 1.6 Quantum Phase Transitions

If there is an asymmetry between the channels,  $J_1 \neq J_2$ , 2CK physics will not be present at very low energies. Instead, a 1CK effect forms with the more strongly coupled reservoir (for example, if  $J_1 > J_2$  1CK forms with reservoir 1). In the systems to which 2CK theory has previously been applied, there is a symmetry that forces  $J_1 \approx J_2$  and they are not independently tunable[37]. As mentioned above, in our 2CK system  $J_1$  and  $J_2$  are independently tunable. As we tune from  $J_1 > J_2$  to  $J_1 < J_2$ , a quantum phase transition occurs.

A quantum phase transition is one which occurs due to quantum fluctuation rather than thermal fluctuations[38]. In fact, quantum phase transitions occur even at zero temperature. Quantum phase transitions are driven by changing some parameter of the system, often pressure, magnetic field, or carrier density. One of the most studied is the quantum phase transition of the high temperature superconductor as a function of composition. The phase diagram for a typical high  $T_c$  superconductor is shown in Fig. 1.10. However, for the high  $T_c$  superconductor, a new sample must be grown and measured for each concentration (each point on the x-axis) in the phase diagram.

The phase diagram for 2CK also shows a quantum phase transition as in Fig. 1.11, this time as a function of the abstract coupling from Fig. 1.9. At the quantum critical point ( $J_1 = J_2$ ) at zero temperature, 2CK behavior exists. As temperature increases, 2CK behavior is expected to occur over a larger region:  $J_1 \approx J_2$  [24]. Since we have independent control of both  $J_1$  and  $J_2$ , at finite temperature we will not need to tune exactly to  $J_1 = J_2$  to observe 2CK behavior. In fact, in chapter 6, we demonstrate the quantum phase transition from phase 1 to phase 2 in Fig. 1.11. We also find behavior consistent with 2CK effect at the associated quantum critical point.

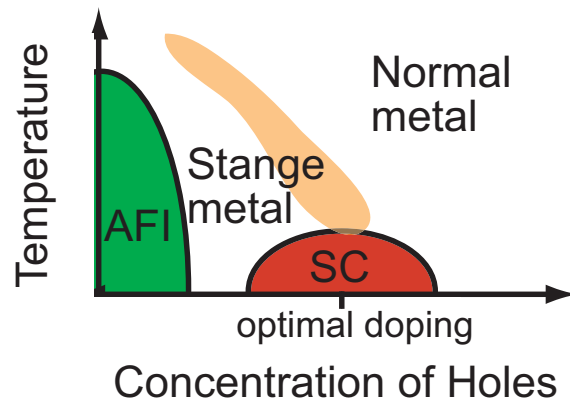


Figure 1.10: Phase diagram of the high temperature superconductor  $La_{2-x}Sr_xCuO_4$  as a function of hole doping. Increasing  $x$  increases the number of holes in the system, driving the system from an antiferromagnetic insulator (AFI, green) to a superconductor (SC, red).

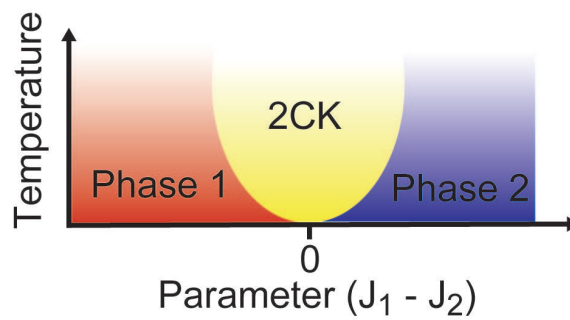


Figure 1.11: Phase diagram for 2CK Hamiltonian.

# Chapter 2

## Spin Measurements of GaAs

### Quantum Dots

To what extent is electron spin important in mesoscopic devices? Coulomb repulsion dramatically effects a device's electronic properties. However, the Fermi properties of electrons can also effect electron arrangements and correlations. Mesoscopic physics allows us to study how electrons arrange themselves over small length scales[39, 40].

In this section, I will introduce the main devices we use to probe electron interactions on short length scales. They include narrow (one dimensional) constrictions known as quantum point contacts and confined (zero dimensional) droplets of electrons known as quantum dots. I then discuss a collection of experiments to measure the spin properties of these mesoscopic structures. I present measurements of the spin properties of quantum dots and a direct measurement of the polarization of electrons emitted from mesoscopic devices. Much of this chapter is adapted from previously published work [13, 41], although here presented in an order to aid the flow of the dissertation.

One goal of this work was to address the question to what extent is spin a good quantum number in these devices, and if it is a good quantum number, can you trans-

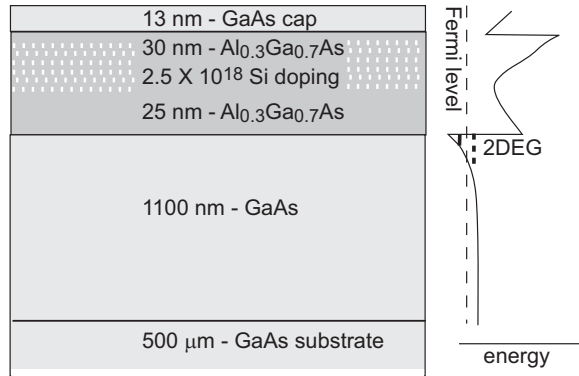


Figure 2.1: Typical layer structure of a *GaAs/AlGaAs* heterostructure. The silicon dopants donate electrons to the *GaAs/AlGaAs* heterointerface and at low temperature a potential well is formed in the vertical direction. Various parameters such as dopant concentration can be tuned so that electrons occupy only a single quantum state in the vertical direction.

port the spin information to a nonlocal readout? These types of questions may become important in future work in quantum computation and the understanding of the role of spin in determining device properties.

## 2.1 The Quantum Dot

The main device studied in this thesis is the quantum dot fabricated on a *GaAs/AlGaAs* heterostructure, with a two dimensional electron gas (2DEG) formed at the heterointerface, as shown in Fig. 2.1. In this thesis, the 2DEGs used have an electron density between  $1\text{-}2.5 \times 10^{11} \text{ cm}^{-2}$ . We use Hall effect to determine density of these wafers.

In this semiconductor system, we can isolate a droplet of electrons by electrostatic repulsion using nearby gate electrodes. One typical design is shown in Fig. 2.2. A multistep lithography process is used to deposit and anneal ohmic contacts to the 2DEG and then pattern and deposit gate electrodes.

Quantum dots have been studied in a variety of systems for many years. When

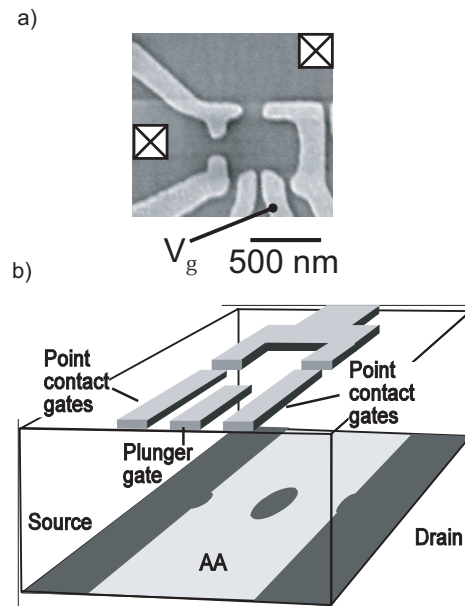


Figure 2.2: (a) SEM image of quantum dot with gate electrodes, one labeled  $V_g$ . Applying negative voltage to the gates depletes the electrons beneath, in this case isolating a small droplet of electrons from source (left) and drain (top) electrodes. In (b) a drawing shows the typical depletion regions in the 2D electron gas. All current from source to drain must travel through the small droplet.

the quantum dot is well isolated from its leads (explained further in Chapter 3) and in low magnetic field, transport through the quantum dot is well described by the constant interaction (CI) model presented in Fig. 2.3[42]. In the CI model, all electron interactions are taken into account by a classical charging energy,  $E_c = e^2/C$ , where  $C$  is the capacitance of the island. In a well isolated quantum dot (one whose leads have small transmission),  $E_c$  can be modeled by the self capacitance of a 2D metal disc,  $C = 8\epsilon\epsilon_0 l$ , where  $l$  is the radius of the disc. The confining potential produces a second energy scale due to quantum confinement,  $\Delta$ .  $\Delta$  can be modeled by particle in a 2D box (neglecting interactions but including spin degeneracy),  $\Delta = \frac{\hbar^2 \pi}{mL^2}$ .

The Hamiltonian most commonly used to describe this situation is (in second quantized notation)

$$H = \sum_{k,\sigma} \epsilon_{k\sigma} c_{k\sigma}^\dagger c_{k\sigma} + \epsilon_d \sum_{\sigma} d_{\sigma}^\dagger d_{\sigma} + E_c (n - N)^2 + \sum_{k,\sigma} V_k (c_{k\sigma}^\dagger d_{\sigma} + H.c.) \quad (2.1)$$

where the first term is a typical description of a Fermi sea (left and right reservoirs from figure 2.3). The second and third terms describe the quantum dot, where the quantum energy level spectrum is contained in the second term and the third term describes the interactions as a classical charging energy  $E_c$  associated with the addition of excess electrons on the dot.  $n$  measures the number of excess electrons on the quantum dot,

$$n = \sum_{n,\sigma} d_{n\sigma}^\dagger d_{n\sigma}, \quad (2.2)$$

and  $N$  denotes an effective interaction of a nearby gate voltage. Finally, the last term describes the coupling between the quantum dot and the Fermi reservoirs.

Many properties of the quantum dot can be studied by simply attaching electrical leads and probing transport. The gate electrodes both control the electrostatic energy of the quantum dot and form barriers to the leads of the quantum dot. (These barriers transmit or reflect electrons incident from the bulk onto the dot.) There are two

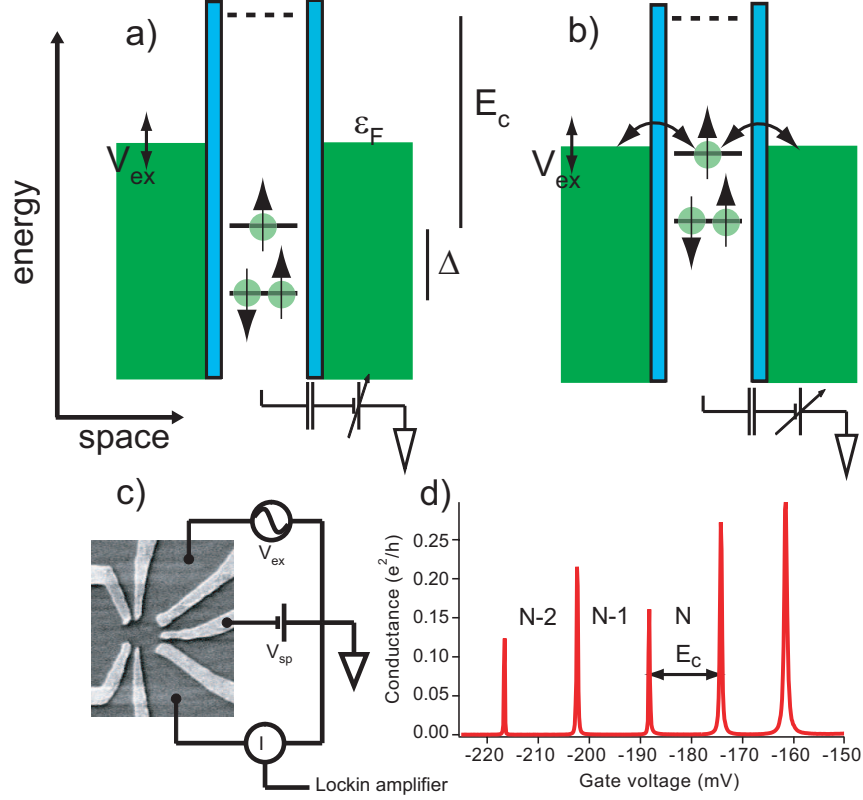


Figure 2.3: Constant interaction (CI) model. A useful way to describe the various parameters of the CI model is by drawing energy and occupation as a function of position, as in (a) and (b). On the left side and right side of (a), are Fermi reservoirs (green) with continuous density of states filled up to the Fermi energy,  $\epsilon_F$ . The two Fermi reservoirs are separated by two potential barriers (blue) which confine a defined number of electrons (3 in this case) to the quantum dot. It costs a maximum of energy  $E_c$  to add (remove) an electron to (from) the quantum dot. The quantum energy level spacing,  $\Delta$ , is also labeled. The quantum energy levels will also be broadened by energy  $\Gamma$  due to coupling to the leads ( $\Gamma$  is very small ( $\Gamma \ll kT$ ) in a well isolated quantum dot). We then apply a small ac signal ( $V_{ex}$ ) to one of the reservoirs, as in (c). In (a), no current flows across the quantum dot because there are no states of the dot in the energy window  $V_{ex}$ . By varying a gate voltage, such as  $V_{sp}$  in (c), we can change the energy of the dot, eventually making it favorable to have two electrons in the dot. At the charge degeneracy point (2 and 3 electrons are energetically degenerate in (b)), there is a state in the transport window and current will flow. An example trace of differential conductance ( $g$ ) as a function of  $V_{sp}$  is shown in (d).

different regimes we study in these experiments: a quantum dot well isolated from its leads and a quantum dot with a fully transmitting conducting channel separating it from the leads. In this dissertation, I will only include a discussion of the well isolated quantum dot. Refer to Appendix ?? or J. Folk dissertation for a discussion of the spin properties of a quantum dot with a single channel connected to the leads.

## 2.2 Spin Properties of Closed Quantum Dots

In this section, we measure spin properties of small quantum dots which are well isolated from their leads. Previous work has shown the importance of spin in quantum dot measurements [43, 44, 20, 45, 21], including the indications of higher spin states. In the measurements presented here (and all previous measurements), differences in energy as a function of magnetic field are used to measure spin transition in the quantum dot. We are able to observe spin transitions of an many electron ( $\sim 40e^-$ ) quantum dot and a few electron (down to zero  $e^-$ ) quantum dot.

### 2.2.1 Probing Ground State Spin Transitions

The device for probing spin was fabricated using *Cr/Au* surface depletion gates on the surface of a high-mobility *GaAs/Al<sub>0.36</sub>Ga<sub>0.64</sub>As* 2DEG lying 102 *nm* from the surface and contacted electrically via nonmagnetic *PtAuGe* ohmics. The high mobility of this sample ( $\mu = 5.5 \times 10^6 \text{ cm}^2/\text{Vs}$  for the unpatterned wafer in the dark, limited mostly by remote impurity scattering) was necessary to observe clear focusing peaks used in the second set of measurements, see section 2.3. This mobility and an electron density of  $1.3 \times 10^{11} \text{ cm}^{-2}$  yield a mean free path of 45  $\mu\text{m}$  and a Fermi velocity of  $v_F = 2 \times 10^7 \text{ cm/s}$ . Measurements were performed in dilution refrigerator with base electron temperature

of  $70mK$ . A standard superconducting solenoid was used to generate the Zeeman field ( $B_{\parallel}$ ), while an independent superconducting coil was used to generate perpendicular magnetic ( $B_{\perp}$ ) fields up to  $250mT$ .

In order to resolve individual ground state transitions, all other energies must be smaller than  $\Delta$ . In these experiments, the criterion  $eV_{ds}, kT, \Gamma < \Delta$  must be met, where  $eV_{ds}$  is the source-drain voltage applied to the device,  $kT$  is temperature, and  $\Gamma$  is the energy broadening of the quantum levels due to coupling to the leads, as in Fig. 2.3. In these devices, the temperature is given by a normal Fermi-Dirac distribution in the leads. When  $\Delta \gg kT$  the quantum dot can be considered to be always in its ground state (effectively at zero temperature).

In Fig. 2.4(a), the position of 6 consecutive CB peaks is plotted as a function of magnetic field. On a CB peak, transport through an  $N$ -electron dot occurs via the addition and removal of the  $N + 1$  electron, with the corresponding z-component of the dot spin,  $S_z(N)$ , changing to  $S_z(N + 1)$  and back again. The energy required for this transition as measured by CB peak position depends on the magnetic field  $B$  through the Zeeman term,  $-g\mu B(S_z(N + 1) - S_z(N)) = -g\mu B(\Delta S_z)$ . The spacing between  $N \rightarrow N + 1$  and  $N + 1 \rightarrow N + 2$  CB peaks is then given by  $-g\mu B[(S_z(N + 2) - S_z(N + 1)) - (S_z(N + 1) - S_z(N))]$ . (The effect of the magnetic field on the orbital energies is minimized in this experiment by changing only the in-plane component,  $B_{\parallel}$ .) A CB peak position that moves upward in gate voltage (upward in the energy required to add an additional electron) as a function of field indicates a spin-decreasing transition; downward motion in gate voltage indicates a spin-increasing transition. In terms of peak spacings, a spin-increasing transition of  $\Delta S_z$  followed by a spin-decreasing transition of  $-\Delta S_z$  yields a spacing that increases with field; for the opposite sequence, the peak spacing decreases with field. For the case of  $\Delta S_z = \frac{1}{2}$  transitions,

the slopes of the spacings will be  $\pm g\mu$ . Consecutive transitions of the same magnitude and in the same direction, for instance  $S_z = 0 \rightarrow \frac{1}{2} \rightarrow 1$ , yield a peak spacing that does not change with field.

Six consecutive CB peaks as a function of magnetic field for the larger dot are shown in Fig. 2.4 (b). The parabolic dependence of peak position on  $B_{\parallel}$  is believed to result from the effect of the field on the well confinement potential [20, 46]; this effect gives the same shift for all CB peaks, and so disappears when the peak spacing is extracted. Corresponding CB spacings, shown in Fig. 2.4(c), display linear motion with slopes  $\pm g\mu$  and zero, where the  $g$ -factor is consistent with the bulk value for *GaAs*,  $g = -0.44$ .

Beginning from an arbitrary value of spin for the  $N$  electron dot,  $S_z(N)$ , we can enumerate the ground state spin transitions for the dot as additional electrons are added (peak spacings provide no information on the absolute magnitude of spin, only spin transitions). For example, in Fig. 2.4(c) at  $2.5T$ , the spacing for the two peaks at the most negative gate voltage (fewest electrons) decreases with  $B_{\parallel}$ , suggesting that  $S_z(N+1) = S_z(N) + \frac{1}{2}$  and  $S_z(N) = S_z(N-1) - \frac{1}{2}$ . Taking  $S_z(N) = \frac{1}{2}$  gives a spin structure for the states shown in Fig. 2.4 (labeled  $N-1, N, \dots, N+5$ ) of  $(1, \frac{1}{2}, 1, \frac{1}{2}, 0, \frac{1}{2}, 1)$  at  $B = 2.5T$ . The occurrence of peak spacings with zero slope is evidence of higher-spin ground states. No two consecutive spacings both have slopes  $+g\mu$  or  $-g\mu$ . This indicates that spin changes of  $\frac{3}{2}$  or greater upon adding an electron are not seen. (Due to the negative  $g$ -factor in GaAs, the lower-energy spin state for a single electron will generally be anti-aligned with an external magnetic field; therefore we will define  $S_z = +\frac{1}{2}$  to be anti-aligned with the field, and for consistency the reader may then use a positive  $g$ -factor for energy calculations.)

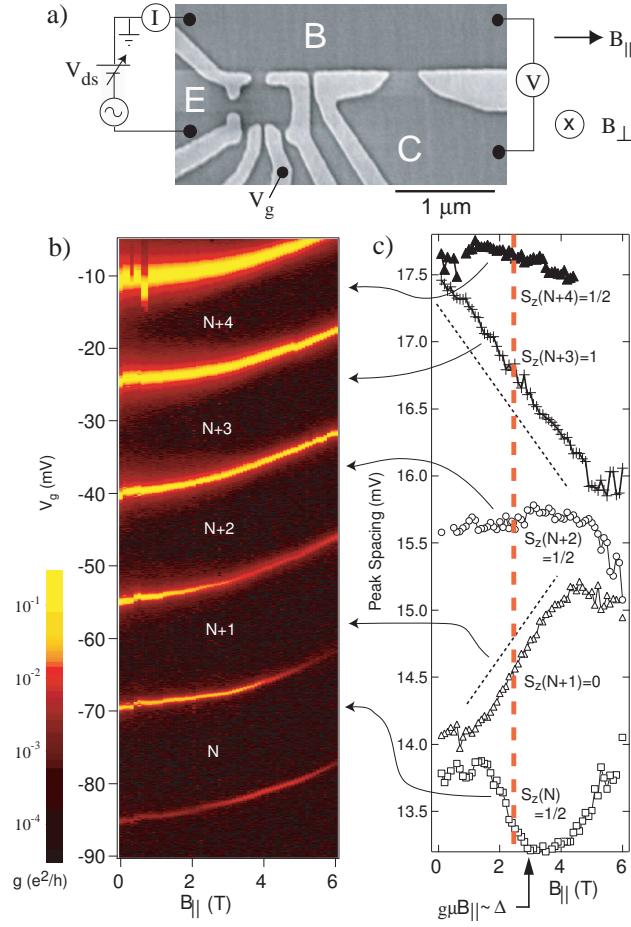


Figure 2.4: (a) Micrograph of a quantum dot, similar to the one measured, in a focusing geometry. A voltage is applied from emitter (E) to base (B) regions; emitter current and base-collector (B-C) voltage give dot conductance and focusing signal respectively. (b) Six consecutive Coulomb blockade peaks in the weak tunneling regime (valley conductance near zero), measured as a function of gate voltage,  $V_g$ , and in-plane magnetic field,  $B_{\parallel}$ . A hall bar fabricated on the same chip allows the perpendicular field,  $B_{\perp}$ , to be measured simultaneously and held at  $\sim -110mT$ . (c) Peak spacings (in  $V_g$ ) extracted from the data in (b). From the slopes of these lines in  $B_{\parallel}$ , the spin transition associated with each Coulomb blockade peak may be determined. For example, at  $B_{\parallel} = 2.5T$  (red dashed line) a possible sequence of ground spin states resulting from these transitions is shown. The dotted black lines indicate expected slopes of peak spacing for  $S_z(N) \rightarrow S_z(N) \pm \frac{1}{2}$  transitions, using  $g = 0.44$ . Spacings offset for clarity.

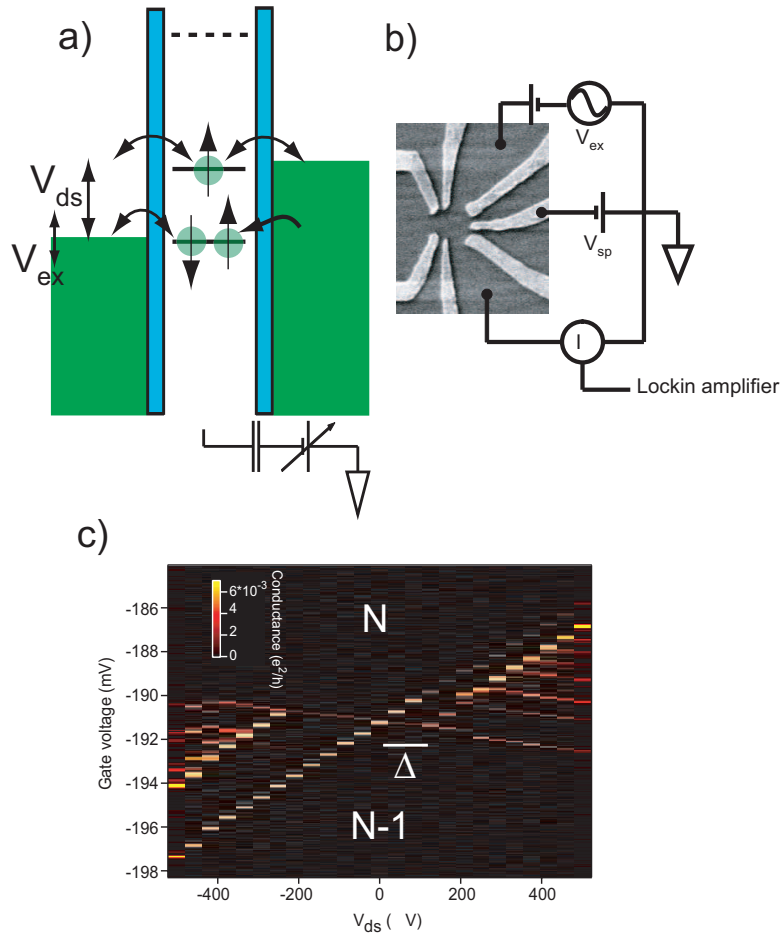


Figure 2.5: Figure of linear and nonlinear transport through quantum dot.

## 2.2.2 Excited state measurements of quantum dots

Nonlinear ‘spectroscopy’ reveals information about excited states of the same electron number transition. By applying a finite bias, as shown in Fig. 2.5, excited states normally energetically forbidden to contain (or lose) electrons can be accessed as a finite d.c. bias ( $V_{ds}$ ) is applied across the device. When an excited state enters the transport window ( $eV_{ds}$ ), it is allowed to participate in transport. This will change the current flowing through the device, and thus the differential conductance signal.

Excited state spin transitions can also be observed using finite dc drain-source bias

when  $V_{ds} > g\mu B$ . A change in spin between two states (either ground or excited) of the  $N$  and  $N + 1$  electron systems would be expected to cause the corresponding peak in differential conductance to shift with  $B$  [43, 44]. Furthermore, any transition which is spin degenerate at  $B = 0$  should split as a function of field. Excited state transitions from several consecutive Coulomb blockade peaks in the larger dot are shown at  $V_{ds} = 400\mu V$  as a function of  $B$  and  $V_g$  in Fig. 2.6(a). Splitting of excited state features with field is only occasionally observed, suggesting a lack of spin degeneracy for many of these transitions. At the same time, some distinct transitions move toward or away from each other with slopes  $\pm g\mu$ , possibly indicating differences in dot spin for initial and final states.

To eliminate the complicating effects of a many-electron system, we also measured spin transitions for the  $N = 0 \rightarrow 1$  electron transition using the smaller dot (Fig. 2.6(b), inset). Finite drain-source measurements were used to find the  $0 \rightarrow 1$  electron transition, see Fig. 2.6(b) [47]. This transition displays clear splittings for both the ground and first excited states (Fig. 2.6(c)), with  $g$ -factors measured to be  $g \sim 0.37$ . When more electrons were added to the device (for example, for the  $1 \rightarrow 2$  electron transition or even more clearly for  $2 \rightarrow 3$  or higher transitions) splittings were only occasionally observed (data not shown). The simpler behavior for the  $0 \rightarrow 1$  electron transition may indicate the important effect of interactions on the spin structure of multi-electron dots [48].

In the absence of spin blockade [46, 49], one would expect  $S_z$  of the dot to change by the spin  $s_z = \pm\frac{1}{2}$  of the electron added to it:  $S_z(N + 1) = S_z(N) + s_z$ . This would imply opposite polarization of transport current for spin-increasing and spin-decreasing transitions [50]. We examine this expectation experimentally by comparing the spin transitions determined by CB peak position to a direct measurement of the

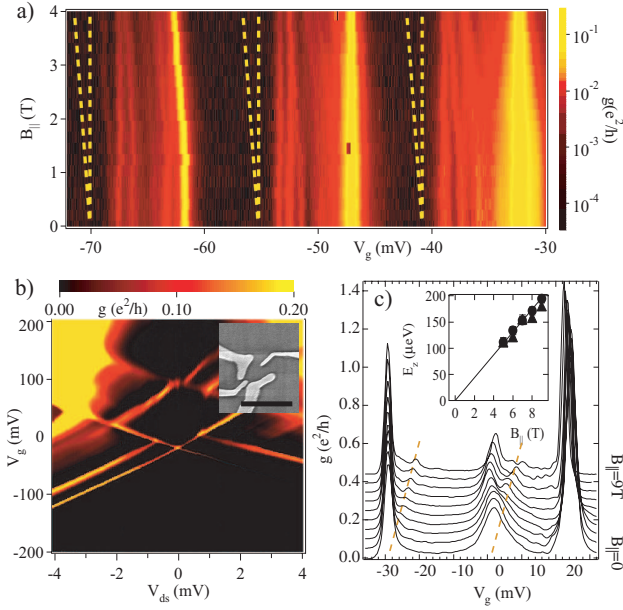


Figure 2.6: (a) Color plot of the differential conductance of Coulomb blockade peaks at  $V_{ds} = 400\mu V$ , as a function of  $V_g$  and  $B_{\parallel}$  ( $B_{\perp}$  held constant at  $-110mT$ ) for the quantum dot shown in Fig. 1. (All  $V_g$  traces were shifted to align the rightmost peak.) For comparison the dashed lines show an energy separation of  $g\mu B$ , taking  $g = 0.44$ . Splitting is only occasionally observed. (b) and (c) Similar measurements taken on a different quantum dot (micrograph shown in Fig. 2(b) inset, scale bar is  $1\mu m$ ) (b) Coulomb diamond at  $B_{\parallel} = 0$  and  $B_{\perp} = -200mT$  demonstrating that the CB peak near  $V_g = 0$  is the  $0 \rightarrow 1$  electron transition. (c) Differential conductance of the  $0 \rightarrow 1$  electron CB peak at  $V_{ds} = 1200\mu V$  from  $B_{\parallel} = 0$  to  $9T$  (curves offset for clarity, and individually rescaled to have a constant height for the rightmost peak). In contrast to (a), clear spin splitting of ground and excited states is seen for this transition (dashed yellow lines are guides to the eye). Inset: splitting as a function of  $B$  for the ground state (solid circles) and first excited state (solid triangles). Solid line shows best fit to the data, and gives a  $g$ -factor of  $0.37$ .

spin polarization of current emitted on a CB peak.

From these and other similar measurements [20, 21], we may conclude that spin is behaving in a consistent manner in a quantum dot. In the next section, I present results which do not coincide with this simple picture of spin in quantum dots.

## 2.3 Focusing measurements

One main advantage of the 2DEG based devices is high mobility of the electrons in the 2D plane. In fact, in our 2D electron gas, mean free paths as high as  $30\mu m$  are expected. This allows for devices to be ballistically coupled together. We can take the electrons that have passed through a device and move them to another, non local device to analyze some property of them. In our case, we use a focusing geometry to analyze the spin properties of *GaAs* devices. Section 2.3.1 is a reprint of [18].

### 2.3.1 Measuring Spin Polarized Current in Semiconductor Nanostructures

Abstract

We demonstrate a mesoscopic spin polarizer/analyzer system that allows the spin polarization of current from a quantum point contact in a large in-plane magnetic field to be measured. A transverse electron focusing geometry is used to couple current from an emitter point contact into a collector point contact. At large in-plane fields, with the point contacts biased to transmit only a single spin ( $g < e^2/h$ ), the voltage across the collector depends on the spin polarization of the current incident on it. Spin polarizations of  $> 70\%$  are found for both emitter and collector at  $300\text{ mK}$  and  $7\text{ T}$  in-plane field.

The detection of electron spin in mesoscopic systems has been the aim of extensive experimental efforts for many years. The ability to prepare, manipulate, and measure electron spin in solid state systems [51] provides a new tool to investigate the physics of mesoscopic structures [52]. In addition, there is hope that this may open the way for applications in spintronics and quantum information processing [53]. However, the long coherence times [54] that make electron spin interesting arise fundamentally from its weak coupling to the environment, and this makes the task of measuring spin difficult.

In this Letter we demonstrate a technique to measure spin currents by converting the problem into the easier one of measuring currents of electrical charge. At low field and low temperature, a narrow constriction in a 2D electron gas (2DEG), known as a quantum point contact (QPC) [see Fig. 2.7(a)], transmits through two spin degenerate channels, producing conductance plateaus at integer multiples of  $2e^2/h$ . When a large in-plane magnetic field is applied, the degeneracy is lifted and conductance becomes quantized in multiples of  $1e^2/h$  [Fig. 2.7(b)] [55, 56]. While the electrons emitted from an  $e^2/h$  plateau are widely believed to be spin polarized, this has not been verified experimentally to our knowledge. One key result of this Letter is the demonstration that point contacts do operate as emitters and detectors of spin current, and therefore allow the detection of spin polarization to be accomplished by simply measuring electrical resistance.

Our experiment is based on a technique known as transverse electron focusing [19], which has been used previously to study phenomena ranging from anisotropy in the band structure of metals [16, 17] and semiconductors [57, 58] to composite fermions in the fractional quantum Hall regime [59]. This device geometry [Fig. 2.7(a)] allows electrons from a spin-polarizing emitter—in this case a QPC—to be coupled into a second QPC serving as a spin-sensitive collector. A magnetic field,  $B_{\perp}$ , applied

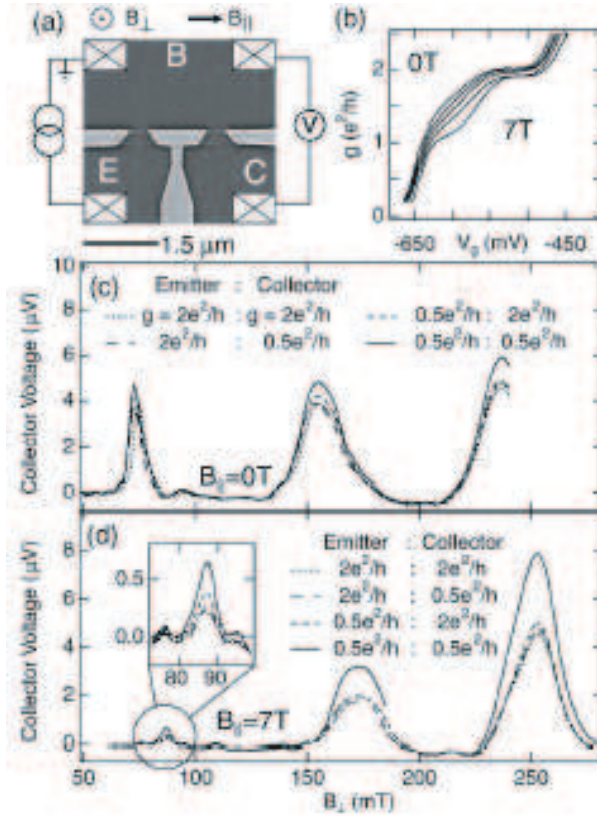


Figure 2.7: (a) SEM micrograph of a device similar to the one measured in this experiment, two quantum point contacts in a transverse focusing geometry with perpendicular ( $B_{\perp}$ ) and in-plane ( $B_{\parallel}$ ) magnetic fields oriented as shown. With a fixed current applied between emitter (E) and base (B), the voltage between base and collector (C) showed focusing peaks as a function of  $B_{\perp}$ . (b) At  $T = 300 \text{ mK}$ , both point contacts showed conductance quantized in units of  $2e^2/h$  at  $B_{\parallel} = 0$ , and in units of  $e^2/h$  at large  $B_{\parallel}$ . (c) At  $B_{\parallel} = 0$ , the collector voltage was nearly independent of the conductances of the two point contacts. The last focusing peak is cut off due to current limitations of the perpendicular field solenoid. (d) At  $B_{\parallel} = 7 \text{ T}$  the focusing peaks were enhanced only when both emitter and collector are set to  $g = 0.5e^2/h$ . The enhancement demonstrates that both emitter and detector are spin selective, by (Eq. 2.3).

perpendicular to the 2DEG plane, bends and focuses ballistic electron trajectories from the emitter to the collector, resulting in peaks in the base-collector voltage [Figs. 2.7(c) and 2.7(d)] whenever the spacing between point contacts is an integer multiple of the cyclotron diameter,  $m^*v_F/eB_\perp$ , where  $m^*$  is the effective electron mass and  $v_F$  the Fermi velocity.

The coupling efficiency between emitter and collector can be quite high in clean 2DEG materials, allowing the two QPCs to be separated by several microns. This separation is useful for measuring spin physics in mesoscopic structures because it allows spin measurements of the emitted current to be decoupled from the details of the emitting device under test, simplifying the interpretation of results. A further advantage of a focusing geometry is that spin detection occurs very quickly ( $< 10$  ps) after the polarized electrons are emitted, leaving little time for spin relaxation.

In the present experiment, the focusing signal is measured as a voltage between collector and base regions, with fixed current applied between emitter and base [Fig. 2.7(a)]. With the collector configured as a voltage probe, current injected ballistically into the collector region at the focusing condition must flow back into the base region, giving rise to a voltage  $V_c = I_c/g_c$  between collector and base, where  $I_c$  is the current injected into the collector and  $g_c$  is the conductance of the collector point contact. For this experiment both point contacts are kept at or below one channel of conductance; therefore the collector voltage may be written in terms of the transmission of the collector point contact,  $T_c$  ( $\leq 1$ ), as  $V_c = (2e^2/h)^{-1}I_c/T_c$  in the spinless case.

To analyze how spin polarization affects the base-collector voltage, we assume  $I_{\downarrow c} + I_{\uparrow c} = \alpha(I_{\downarrow e}T_{\downarrow c} + I_{\uparrow e}T_{\uparrow c})$ , where  $I_e$  is the emitter current, and  $\alpha$  is a spin-independent efficiency parameter reflecting imperfections in the focusing process such as scattering from impurities ( $0 < \alpha < 1$ ). In the absence of spin effects ( $T_{\uparrow c} = T_{\downarrow c}$ ), one then

expects  $V_c$  to be independent of  $g_c$ , although different settings of the point contact may in practice affect  $\alpha$ . Because  $I_e$  is fixed,  $V_c$  is also independent of the emitter conductance,  $g_e$ .

Taking into account different transmissions for the two spin channels, however, one expects the voltage on the collector to double if both emitter and collector pass the same spin, or drop to zero if the two pass opposite spins. This conclusion assumes that a spin polarized current injected into the collector region will lose all polarization before flowing out again. Under these conditions, the collector voltage generally depends on the polarization of the emitter current  $P_e = (I_\uparrow - I_\downarrow)/(I_\uparrow + I_\downarrow)$  and the spin selectivity of the collector  $P_c = (T_\uparrow - T_\downarrow)/(T_\uparrow + T_\downarrow)$  in the following simple way:

$$V_c = \alpha \frac{h}{2e^2} I_e (1 + P_e P_c). \quad (2.3)$$

(We have, including spin,  $V_c = (I_{c\uparrow} + I_{c\downarrow})/g_c$ . Since  $I_{c\sigma} \sim I_{e\sigma} T_{c\sigma}$  and  $g_c = (T_{c\uparrow} + T_{c\downarrow})(e^2/h)$ , the collector voltage is  $V_c \sim (I_{e\uparrow} T_{c\uparrow} + I_{e\downarrow} T_{c\downarrow})/(T_{c\uparrow} + T_{c\downarrow})$ .) Note from Eq. 2.3 that colinear and complete spin polarization ( $P_e = 1$ ) and spin selectivity ( $P_c = 1$ ) gives a collector voltage twice as large as when *either* emitter or collector are not spin polarized.

The focusing device was fabricated on a high-mobility two-dimensional electron gas (2DEG) formed at the interface of a GaAs/Al<sub>0.36</sub>Ga<sub>0.64</sub>As heterostructure, defined using Cr/Au surface depletion gates patterned by electron-beam lithography, and contacted with nonmagnetic (PtAuGe) ohmic contacts. The 2DEG was 26 nm from the Si delta-doped layer ( $n_{Si} = 2.5 \times 10^{12} \text{ cm}^{-2}$ ) and 102 nm below the wafer surface. Mobility of the unpatterned 2DEG was  $5.5 \times 10^6 \text{ cm}^2/Vs$  in the dark, limited mostly by remote impurity scattering in the relatively shallow structure, with an estimated background impurity level  $< 5 \times 10^{13} \text{ cm}^{-3}$ . With an electron density of  $\sim 1.3 \times 10^{11} \text{ cm}^{-2}$ , the transport mean free path was  $\sim 45 \mu m$ , much greater than the distance (1.5  $\mu m$ )

between emitter and collector point contacts. The Fermi velocity associated with this density is  $v_F = 2 \times 10^7 \text{ cm/s}$ , consistent with the observed  $\sim 80 \text{ mT}$  spacing between focusing peaks.

Measurements were performed in a  $^3\text{He}$  cryostat with a base temperature of  $300 \text{ mK}$ . A conventional superconducting solenoid was used to generate in-plane fields,  $B_{\parallel}$ , and a smaller superconducting coil wound on the refrigerator vacuum can allowed fine control up to  $\sim 250 \text{ mT}$  of the perpendicular field,  $B_{\perp}$  [60].  $B_{\parallel}$  was oriented along the axis between the two point contacts, as shown in Fig. 2.7(a).

Independent ac current biases of  $1 \text{ nA}$  were applied between base and emitter ( $17 \text{ Hz}$ ), and base and collector ( $43 \text{ Hz}$ ), allowing simultaneous lock-in measurement of the emitter conductance (base-emitter voltage at  $17 \text{ Hz}$ ), collector conductance (base-collector voltage at  $43 \text{ Hz}$ ), and the focusing signal (base-collector voltage at  $17 \text{ Hz}$ ). The base-collector current bias was found to have no effect on the focusing signal. Additionally, the focusing signal was found to be linear in base-emitter current for the small currents used in this measurement.

The qualitative behavior of the focusing peaks did not change upon thermal cycling. Although all of the data presented in this paper comes from a single device, the results were confirmed in a similar device on the same heterostructure. Statistics leading to estimates of typical polarization values discussed at the end of the paper were gathered over five settings of point contact voltages (for fixed conductance) for each of the three focusing peaks. Data from the three focusing peaks showed consistent behavior.

Spin polarized emission and detection were measured by comparing the height of the focusing peak for various conductances of the emitter and collector point contacts. At  $B_{\parallel} = 0$ , where no static spin polarization is expected, the focusing signal was found to be nearly independent of the conductances of both emitter and collector point contacts,

as shown in Fig. 2.7(c). In contrast, at  $B_{\parallel} = 7 T$ , the focusing signal observed when both the emitter and collector point contacts were set well below  $2e^2/h$  was larger by a factor of  $\sim 1.7$  compared to the signal when either emitter or collector was set to  $2e^2/h$ , as seen in Fig. 2.7(d). Equation 2.3 predicts a factor of 2 enhancement for fully spin polarized emission and aligned, fully spin selective, detection.

To normalize for overall variations in transmission through the bulk from the emitter to the collector, the focusing signal can be expressed as a ratio normalized by the value when both the emitter and collector are set to  $2e^2/h$ . We denote the point contact settings as  $(x : y)$  where  $x$  is the conductance of the emitter and  $y$  is the conductance of the collector, both in units of  $e^2/h$ . Ratios are then denoted  $(x : y)/(2 : 2)$ .

Figures 2.8 and 2.9 show the focusing signal ratios for the third focusing peak ( $B_{\perp} \sim 230 - 250 mT$ ), chosen because its height and structure in the  $(2 : 2)$  condition were less sensitive to  $B_{\parallel}$  and small variations in point contact tuning compared to the first and second peaks. Although all curves shown in this paper was for the third focusing peak, spin polarization extracted from the first and second focusing peaks gave similar results.

Figure 2.8(a) shows that only the ratio  $(0.5 : 0.5)/(2 : 2)$  grows with  $B_{\parallel}$ , reaching a value  $\sim 2$  at  $7T$ , while the other ratios,  $(2 : 0.5)/(2 : 2)$  and  $(0.5 : 2)/(2 : 2)$ , are essentially independent of in-plane field, as expected from Eq. 2.3 if no spin selectivity exists when the conductance is  $2 e^2/h$ . At  $B_{\parallel} = 0$ , we find  $(0.5 : 0.5)/(2 : 2) \sim 1.4$ , rather than the expected 1.0, for this particular cooldown. As discussed below, these ratios fluctuate somewhat between thermal cycles.

Temperature dependencies of the  $(0.5 : 0.5)/(2 : 2)$  ratio are shown in Fig. 2.8(b) for a different cooldown. At  $B_{\parallel} = 7T$ , the ratio  $(0.5 : 0.5)/(2 : 2)$  decreases from  $\sim 2.2$  at  $T = 300 mK$  to the zero-field value of 1.4 above  $2K$ . Note that  $2K$  is roughly the

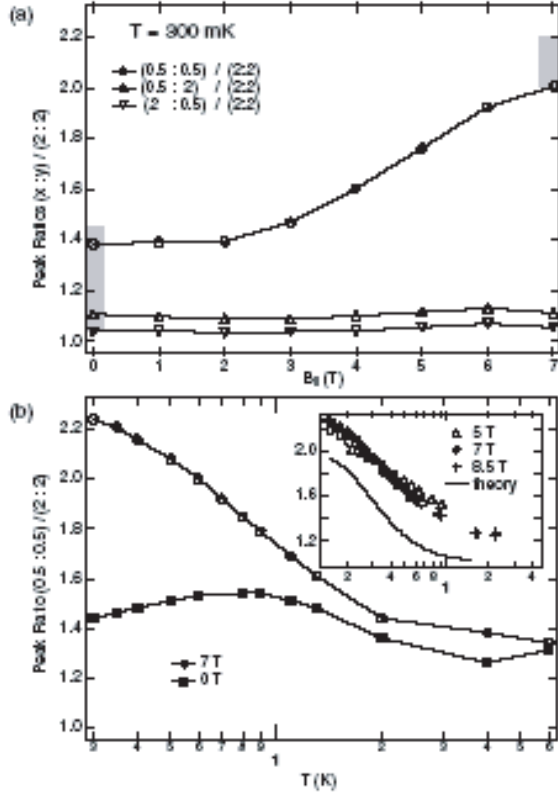


Figure 2.8: (a) The height of the third focusing peak as a function of  $B_{\parallel}$  for different conductances of the point contacts ( $x : y$ ), where  $x$  is the emitter conductance and  $y$  is the collector conductance (in units of  $e^2/h$ ), all normalized by the  $(2 : 2)$  focusing peak height. According to Eq. (2.3), a factor of two in the ratio indicates fully spin polarized emission and detection. Grey shaded boxes indicate typical ranges (see text) of  $(0.5 : 0.5)/(2 : 2)$  ratio. (b) Temperature dependence of the ratio of focusing signals  $(0.5 : 0.5)/(2 : 2)$  for  $B_{\parallel} = 7 T$  and  $0 T$ . (a) and (b) are from different cooldowns. Inset: Ratio  $(0.5 : 0.5)/(2 : 2)$  for  $B_{\parallel} = 5, 7$ , and  $8.5 T$  plotted as a function of the scaled temperature  $kT/g\mu B_{\parallel}$ . The solid curve is the prediction of a simple model (see text) that accounts for only thermal broadening in the leads.

temperature at which  $g\mu B_{\parallel}/kT \sim 1$ , using the GaAs g-factor  $g = -0.44$ . At  $B_{\parallel} = 0$ , the ratio  $(0.5 : 0.5)/(2 : 2)$  remains near 1.4, with only a weak temperature dependence up to  $6K$ .

The inset of Fig. 2.8(b) shows that the focusing data at several  $B_{\parallel}$  scale to a single curve when plotted as a function of  $kT/g\mu B_{\parallel}$ , suggesting that both spin-polarized emission and spin-selective detection arise from an energy splitting that is linear in  $B_{\parallel}$ . A simple model that accounts roughly for the observed scaling of the focusing signal assumes that the point contact transmission,  $T(E)$ , is 0 for  $E < E_0$ , and 1 for  $E > E_0$ , where  $E$  is the electron kinetic energy and  $E_0$  is a gate-voltage-dependent threshold. Spin selectivity then results from the Zeeman splitting of the two spin sub-bands, and is reduced by thermal broadening. Except for a vertical offset of  $\sim 0.4$ , this simple model agrees reasonably well with the data [Fig. 2.8(b), inset].

Fig. 2.9(a) shows the evolution of spin selectivity in the collector point contact as a function of its conductance. At  $B_{\parallel} = 6 T$ , with the emitter point contact set to  $0.5e^2/h$ , the collector point contact is swept from  $2e^2/h$  to 0. The focusing signal increases as the collector point contact conductance is reduced below  $2e^2/h$ , saturating as the collector conductance goes below the  $1e^2/h$  spin-split plateau. The polarization saturates completely only well into the tunneling regime, below  $\sim 0.5e^2/h$ . For this reason we use emitter and collector conductances of  $0.5e^2/h$  in all figures for the spin selective cases (although the qualitative behavior of the data was essentially the same here as on the  $e^2/h$  plateau). Similar to the effect seen in Fig. 2.8(b), spin selectivity decreases with increasing temperature, approaching the zero field curve at  $1.3 K$ .

Fig. 2.9(b) shows the same measurement taken at  $B_{\parallel} = 0$ . The focusing peak rises slightly when both point contacts are set below one spin degenerate channel. Unlike at high field, however, the increase of the focusing signal is very gradual as the point

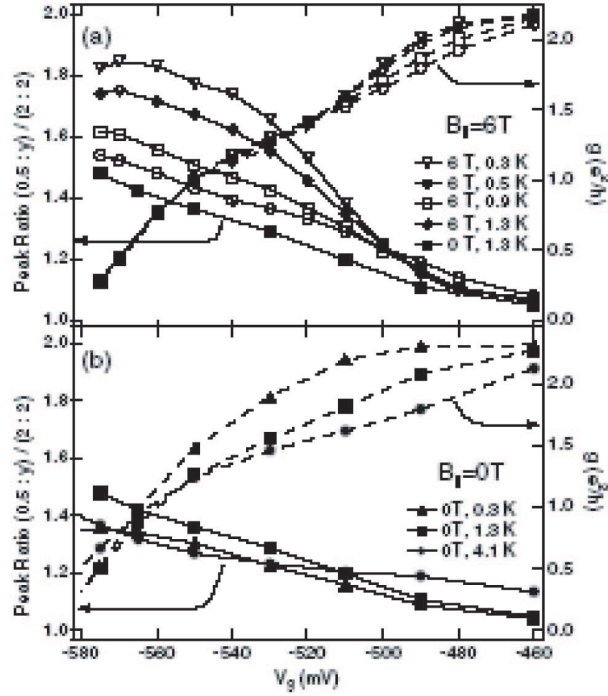


Figure 2.9: (a) Focusing signal ratio  $(0.5 : y)/(2 : 2)$  and collector conductance  $g$  at  $B_{\parallel} = 6 T$  as a function of the voltage applied to one of the collector gates, with the emitter fixed at  $g = 0.5e^2/h$ . This shows the onset of spin selectivity as the collector point contact is brought into the tunneling regime,  $g < 2e^2/h$ . (b) The same data taken at  $B_{\parallel} = 0$ , showing little temperature dependence up to 4 K. A mild 0.7 structure in the conductance becomes more prominent at 1.3 K.

contact is pinched off. In addition, temperature has only a weak effect.

As mentioned above, both the low and high field ratios  $(0.5 : 0.5)/(2 : 2)$  were typically measured to be larger than their ideal theoretical values of 1 and 2 respectively. Sampled over multiple thermal cycles, several gate voltage settings (shifting the point contact centers by  $\sim 100 \text{ nm}$ ), and different focusing peaks, the ratio at  $B_{\parallel} = 0$  varied between 1.0 and 1.6, with an average value of 1.2 and a standard deviation  $\sigma = 0.2$ . The average value of the ratio at  $B_{\parallel} = 7 \text{ T}$  was 2.1, with  $\sigma = 0.1$ . This represents an increase from low to high field by a factor of  $1.7 \pm 0.3$ , so from Eq. 1 one finds  $P_e P_c = 0.7 \pm 0.3$ . Because neither  $P_e$  nor  $P_c$  can be greater than 1, this then implies that both  $P_e$  and  $P_c$  are greater than  $0.7 \pm 0.3$ , and under the assumption that  $P_e \sim P_c$  it implies that  $P_e, P_c \geq 0.8$ .

Both point contacts display a modest amount of zero-field 0.7 structure [61, 62], as seen in Figs. 2.7(b) and 2.9(b). Although a static spin polarization associated with 0.7 structure would be consistent with our larger-than-one ratio  $(0.5 : 0.5)/(2 : 2)$  at zero field, this explanation is not consistent with an enhanced ratio found *both* at zero field and high field. Rather, we believe the enhancement is due to a slight dependence of  $\alpha$  on QPC settings in the regime  $(T_c, T_e) < 1$ . This explanation is consistent with the weak temperature dependence of the zero-field ratio up to  $4 \text{ K}$ .

An unexplained feature of our data is the relative suppression of the lower-index focusing peaks, particularly the first peak, in a large in-plane field, as seen in Figs. 2.7(c) and 2.7(d). This effect was observed over multiple thermal cycles and for all point contact positions. The effect is not readily explained as a field-dependent change in the scattering rate, as neither the bulk mobility, nor the width of the focusing peak is affected. Also, the effect is not obviously related to spin, as it occurred for both polarized and unpolarized point contacts. All peaks are included in the statistics

presented. In conclusion, we have developed a new method for creating and remotely detecting spin currents using quantum point contacts.

### 2.3.2 Measuring Spin Polarization in Quantum Dots

The spin polarization of current from the quantum dot was also measured in a transverse focusing geometry (shown in Fig. 2.4(a)). As described previously [18, 41] and section 2.3.1, the height of a focusing peak reflects the degree (and direction) of spin polarization of current from the emitter when the collector QPC is spin selective, according to the relation  $V_c = \alpha I_e (h/2e^2)(1 + P_e P_c)$ . Here  $V_c$  is the focusing peak height,  $I_e$  is the total emitter current with polarization  $P_e = (I_{\uparrow e} - I_{\downarrow e}) / (I_{\uparrow e} + I_{\downarrow e})$ , and  $P_c = (T_{\uparrow c} - T_{\downarrow c}) / (T_{\uparrow c} + T_{\downarrow c})$  is the spin selectivity of the collector. (The efficiency parameter  $\alpha$  ( $0 < \alpha < 1$ ) accounts for spin-independent imperfections in the focusing process.)

Using a Coulomb blocked quantum dot as the emitter favors the use of a voltage bias between emitter and base, rather than a current bias as used in Refs. [18, 41]. In this case, changes in the emitter current,  $I_e$ , lead to changes in the focusing peak height even when its polarization remains constant. To study spin polarization, we measure the emitter current along with the collector voltage (Figs. 2.10(a) and 2.10(b)) and use the quantity  $V_c/I_e$ , a *nonlocal* resistance, as a measure of the spin polarization of the current from the CB quantum dot when the collector is spin selective. For a spin-selective collector ( $g_c = 0.5e^2/h$ , in an in-plane field), the value of  $V_c/I_e$  should range from twice the value found in the unpolarized case ( $g_c = 2e^2/h$ ), when emitter polarization and collector selectivity are oriented in the same direction, to zero, when the spin directions are oppositely oriented.

Simultaneous focusing and conductance measurements at  $B_{\parallel} = 6T$  for both spin-

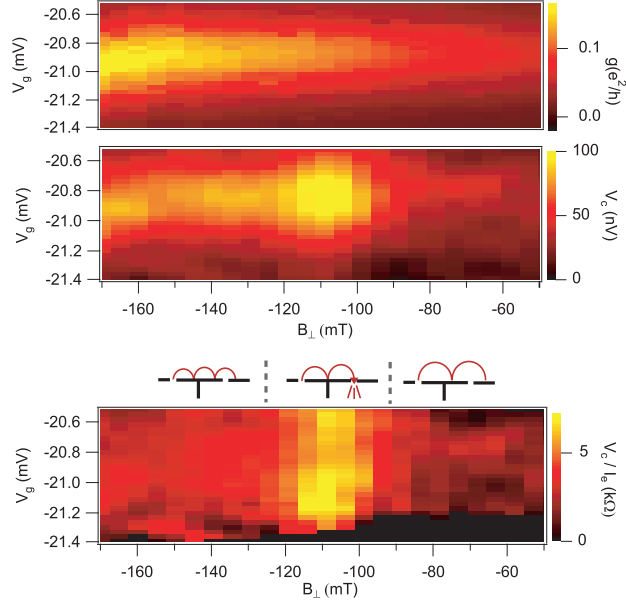


Figure 2.10: (a) Conductance of a CB peak as a function of both  $V_g$  and  $B_{\perp}$ , for the dot shown in Fig. 1(a) in a focusing geometry. (b) Base-Collector voltage,  $V_c$ , measured at the same time as the dot conductance, with  $B_{\perp} = -110\text{mT}$  set to correspond to the second focusing peak (the second peak was used because it was affected least by  $B_{\parallel}$  in this device). (c) The nonlocal resistance  $V_c/I_e$  most clearly shows the effect of focusing. The diagrams indicate the electron focusing condition for fields near the second focusing peak. The location of the focusing peak in  $B_{\perp}$  remained constant for all CB peaks studied. Data does not appear when  $g_e < 0.1e^2/h$  ( $I_e < 20\text{pA}$ ,  $V_c < 40\text{nV}$ ) because the ratio  $V_c/I_e$  becomes unreliable.

selective and spin-independent collector are presented in Figs. 2.11(a,b), as the dot is tuned from the semi-open to the weak tunneling regimes using the voltage,  $V_g$ , on the side gate. We find that the focusing signal  $V_c/I_e$  with spin-selective collector ( $g_c = 0.5e^2/h$ ) always lies above the signal with spin-independent collector ( $g_c = 2e^2/h$ ) once the dot is tuned into the weak tunneling regime. This suggests that the current emitted from the quantum dot at low conductance is always spin polarized in the same direction as the collector, over a range of gate voltage where many electrons are added.

Figure 2.11(c) shows focusing measurements for the same peaks shown Fig. 2.4, at  $B_{\parallel} = 4T$ . Spin transitions of both directions were observed based on peak motion (see Fig. 2.4) whereas spin polarization of emitted current is again found to remain nearly constant over all measured CB peaks. This observation is inconsistent with the picture of spin transitions leading to  $S_z(N + 1) = S_z(N) + s_z$  discussed earlier.

## 2.4 Future of spin in quantum dots

Although certain aspects of this data are still not described adequately by theory, data here indicates the filling of a quantum dot seems to behave relatively simply (Fig. 2.4). We note as well that there is no apparent correlation between peak height and spin transition in a large in-plane field. It was shown in Refs. [18] and [41] that the leads of a quantum dot become spin polarized in the same way as single QPC's in an in-plane field. However, a spin dependent tunnel barrier should lead to a dramatic suppression in CB peak height for spin-decreasing transitions. As seen in Fig. 2.4, this was not observed in our measurement. Taken together, these observations may indicate that spin polarization in the leads is playing a role in the spin state of the quantum dot on a CB peak.

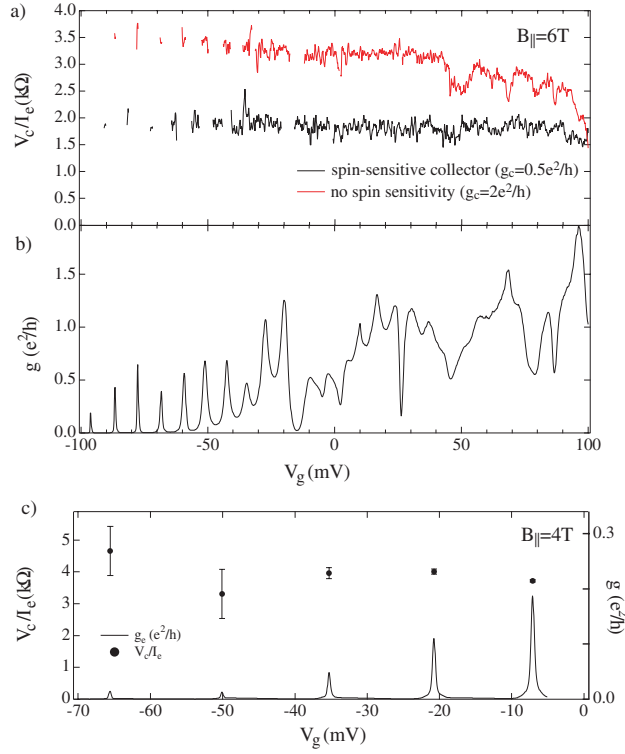


Figure 2.11: (a) Focusing signal at  $B_{\parallel} = 6T$  from the quantum dot shown in Fig. 1, with spin-selective ( $g_c = 0.5e^2/h$ , red curve) and spin-independent ( $g_c = 2e^2/h$ , black curve) collector. The polarization of current fluctuates on a typical gate voltage scale of  $V_g = 5mV$ , but these fluctuations are suppressed as  $V_g$  is reduced below  $30mV$ . At the same time, the spin selective curve rises to nearly twice the value as the curve at  $g_c = 2e^2/h$ , indicating spin polarization of emitter current (see text). (b) Conductance measured simultaneously with data in (a). (c) Focusing signal and conductance measured for the CB peaks shown in Fig. 1 ( $N + 1$  to  $N + 6$ ) at  $B_{\parallel} = 4T$  and  $g_c = 0.5e^2/h$ . Again, only small fluctuations in focusing signal are observed despite different spin transitions observed for these peaks in Fig. 1. Based on the increase of  $V_c/I_e$  to  $3.5k\Omega$  from  $1.9k\Omega$  with the spin selective collector in (a), we would have expected the focusing peak to be suppressed to  $V_c/I_e \sim 0.3k\Omega$  if the opposite polarization were generated at the emitter. (Collector selectivity depends only weakly on  $B$  at these fields and temperatures [18].)

One may also speculate the 0.7 structure found in quantum point contacts may also play a role in the spin of the electrons transported through the dot. Various theories have been proposed to describe the mysterious 0.7 structure. One current line of thought includes a Kondo effect [62](discussed in the remainder of this thesis in light of its role of transport through quantum dots). Although the role of Kondo in this case is unclear, it is worth noting the majority of these experiments took place in high magnetic field which may destroy a spin based Kondo effect. The effect of the entrance and exit leads on transport through a quantum dot is still unknown and requires further investigation.

In conclusion, we have found signatures of spin-increasing and spin-decreasing transitions in transport measurements, including spin splitting of the  $N = 0 \rightarrow 1$  transition. Measurements of polarization of the current emitted from a quantum dot in the CB regime show that the emitted current is in all cases polarized in the same direction as the QPC collector, for both spin-increasing and spin-decreasing transitions of the dot. These observations necessitate a revised picture of spin transitions in lateral quantum dot in an in-plane magnetic field.

# Chapter 3

## Kondo Effect in Quantum Dots

Matter at low temperature exists in variety of different phases, from the normal solid, liquid, gas phases or more exotic phases such as condensate or ferromagnet. In Chapter 1 of [26], Phil Anderson expresses that broken symmetries in the system lead to these states and the phase transitions between them. However, in this chapter we will concentrate on a different kind of phase transition, which Anderson elegantly describes as:

I should caution the reader that broken symmetry is not the only way in which cold matter may change its behavior qualitatively. Although the cases in which the other alternative—a continuous phase transition to a qualitatively different behavior without change of symmetry—occurs are as yet relatively rare, they are quite fascinating. The Kondo Effect is the best known: a continuous transition from magnetic to nonmagnetic behavior of a single impurity.[26]

(The Kondo problem can also be considered a crossover phenomenon rather than a phase transition, refer to [63].)

As Anderson mentions, the Kondo effect is one of the most studied, well understood problems in solid state physics. It is now common to study the classic Kondo problem (first theoretical breakthroughs occurred in the 1960's[3]) in a graduate condensed matter theory class, as I did in Professor Eugene Demler's class at Harvard University. Much of the theory in this section is adapted from the course notes. A recent revival of the Kondo effect has occurred with new and important breakthroughs in experiments, which we will briefly describe here.

Kondo effect has recently been observed in several electronic nanostructures quite different from the prototypical metal with magnetic impurities. These novel quantum dot based Kondo systems are built from materials as diverse as *GaAs/AlGaAs* heterostructures [28, 64], carbon nanotubes [65], and organometallic molecules [66, 67], indicating the generality of this effect. Among the varied ways of confining and coupling electrons, gated *GaAs/AlGaAs* nanostructures stand out for their enormous tunability and design flexibility. These same properties that made *GaAs/AlGaAs* quantum dots an excellent choice for studying a single magnetic impurity screened by nearby conduction electrons will enable the construction and study of a variety of correlated electron systems more complex than a single magnetic impurity. This will provide key insights into the theoretical framework of particular quantum impurity systems, and may help form a more complete picture of interacting electron systems in general. In this chapter, we discuss important background of Kondo effect in bulk materials. Then we introduce the dramatic role it plays quantum dot transport. We also present new results on three lead studies of quantum dots in the Kondo regime, including a measurement of the enhanced density of states out of equilibrium.

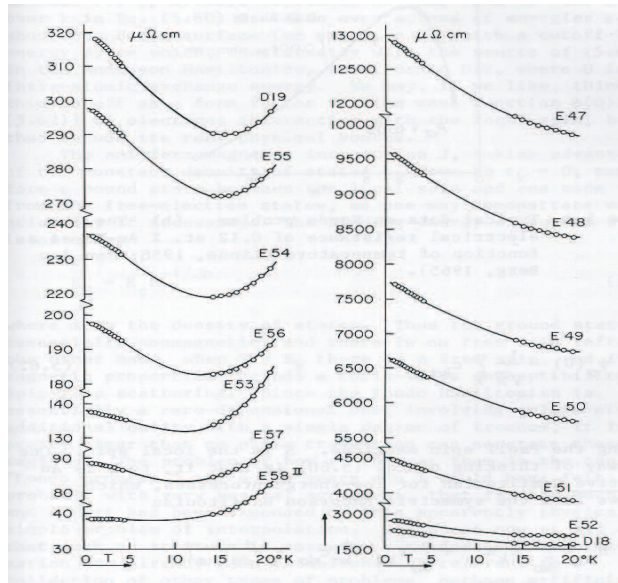


Figure 3.1: Typical data for resistivity as a function of temperature for very pure copper wires. The curves have different concentrations of magnetic (iron) impurities, ranging from 0.123 (top) to 0.0005 (bottom) atomic percentage.

### 3.1 Introduction to Kondo Effect

The Kondo problem, originally associated with clean metals, involved anomalies in resistivity, susceptibility and specific heat. In clean metals, resistivity was expected to decrease as temperature decreases due to less scattering off phonons (atoms in the lattice will vibrate less at lower temperature) until finally saturating due to disorder in the lattice. In sharp contrast, resistivity data, as in Fig. 3.1, showed a logarithmic divergence at low temperature. Coupled with this, susceptibility data indicated a transition from a magnetic state to a nonmagnetic state[26]. These observations were subsequently connected with the presence of a low concentration of magnetic impurities.

In 1964, Kondo introduced a model which included interaction between magnetic impurity atoms (atoms with a net spin) and the surrounding conduction electrons in

a perturbation theory[3]:

$$H = H_0 + H_{int} = \sum_{k,\sigma} \epsilon_k c_{k\sigma}^\dagger c_{k\sigma} + J \sum_{\sigma,\sigma'} s(r) \cdot S \quad (3.1)$$

where  $S$  is the spin of the localized magnetic impurity and  $s(r)$  is the spin of the surrounding conduction electrons a distance  $r$  from the impurity. The localized spin and delocalized conduction electrons interact through an (antiferromagnetic) coupling constant,  $J$ . The perturbation term can be written

$$H_{int} = \frac{J}{N} \sum_{k,k',\sigma\sigma'} e^{i(k-k')R_N} S \cdot c_{k\sigma}^\dagger c_{k'\sigma'} \sigma_{\sigma\sigma'} \quad (3.2)$$

where  $N$  is the number of impurities. Using the second Born approximation to calculate scattering rate and the appropriate scattering terms (those involving energy conservation) led Kondo to a correction to resistivity with logarithmic divergence in temperature[26, 68]

$$\rho' \sim b\nu(0)^2 J^3 \ln\left(\frac{D}{kT}\right), \quad (3.3)$$

where  $b$  is now concentration of impurities,  $\nu(0)$  is the density of states at the Fermi level, and  $D$  is the band width of the conduction electrons (of order the Fermi energy).

When the coupling is antiferromagnetic,  $J > 0$ , the resistivity increases logarithmically as a function of temperature decreasing. The logarithm becomes large below

$$T_K \sim e^{-\frac{1}{J\nu(0)}} \quad (3.4)$$

which sets a characteristic energy scale  $T_K$ , the Kondo temperature, for the correction to the resistivity.

The antiferromagnetic interaction forms a bound state between the conduction electrons and the localized magnetic impurity, with the bond energy  $\sim kT_K$ . The bound state is essentially nonmagnetic, as the local spin is screened by the surrounding conduction electrons by the formation of a many body spin singlet state. (The ground

state of an antiferromagnetic  $s \cdot S$  interaction is a spin singlet.) As the temperature is increased, the bond is broken and the local spin is unpaired, leading to a Curie-Weiss susceptibility. Note this behavior ( $T$  near  $T_K$ ) was derived from perturbation theory of a Fermi liquid. Although Kondo effect is a many body phenomenon, the excitations behave according to Fermi liquid theory [69].

At low temperature, the system is in a spin singlet state, however, it is still partially polarizable. The bulk conduction electrons can then indirectly interact with the Kondo bound state by scattering off of it. In fact, because the site is small and localized, only electrons with  $l = 0$  components to their momentum are important in the scattering. Analysis of the Kondo problem as a scattering problem yields a few interesting results. The Kondo effect is tied to the Fermi level of the conduction electrons. This produces a renormalized (in fact, enhanced) density of states at the Fermi level. Further, because the Kondo effect is pinned to the Fermi level, both specific heat and susceptibility are effected in a manner which allows the Wilson ratio (normalized change in susceptibility divided by normalized change in specific heat) to be the Fermi liquid value of 2.

The resistivity also behaves in a manner consistent with Fermi liquid behavior. The resistivity at low temperature is

$$\rho(T) = \rho_0 - B \left( \frac{T}{T_K} \right)^2 \quad (3.5)$$

where  $\rho_0$  is the zero temperature resistivity and  $B$  may be a universal coefficient (value of coefficient currently under debate). Notice the resistivity goes like  $T^2$ , again consistent with Fermi liquid theory ( $1/E^2$ )[70]. In the language of renormalization group theory, the Kondo effect is an infinite  $J$  fixed point (as temperature is reduced, the coupling strength  $J$  flows all the way to infinite coupling)[63]. At the fixed point, the spin is completely screened, allowing it to be considered only as a spinless potential scattering center (and thus Fermi liquid behavior in both transport and thermodynamic

properties).

It is also worth noting the Kondo Hamiltonian only requires a localized cite with a two-fold degeneracy ( $SU(2)$  spinor) which is shared with the leads. In the next section, a microscopic model for a magnetic impurity (Anderson model) is presented. However, two fold degeneracy other than spin can also undergo a Kondo effect. Recently, this has been observed in both material systems [71] and nanostructures [72, 73, 74].

## 3.2 Anderson Model and the Kondo effect

The Kondo model of interaction between a magnetic impurity and surrounding conduction electrons is very successful at predicting macroscopic behavior. However, a more microscopic model is needed if one is wants to understand the origins of the antiferromagnetic interaction. The Anderson model provides valuable insight into the antiferromagnetic interaction [27].

The Hamiltonian for the Anderson model of a magnetic impurity hybridized with conduction electrons is

$$H = \sum_{\sigma} \epsilon_d n_{d\sigma} + U n_{d\uparrow} n_{d\downarrow} + \sum_{k\sigma} c_{k\sigma}^{\dagger} c_{k\sigma} + \sum_{k\sigma} \left( V_k c_{d\sigma}^{\dagger} c_{k\sigma} + H.c. \right), \quad (3.6)$$

where  $n_{d\sigma} = d_{\sigma}^{\dagger} d_{\sigma}$ . This Hamiltonian contains a single localized state (historically the  $d$  orbital of a magnetic impurity) for the first term and a Fermi sea of electrons for the third term. The localized site is spin degenerate and thus could contain 0, 1 or 2 electrons. Anderson noticed, however, that although the site could contain 0 – 2 electrons, it may be energetically favorable to contain only a single electron due to the strong Coulomb repulsion of electrons confined tight to the local site. He included this as a interaction energy,  $U$ , that must be paid to place two electrons on the site, which is contained in the second term.

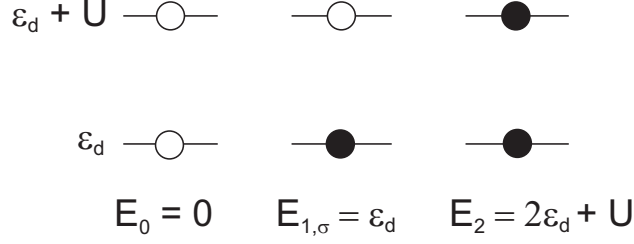


Figure 3.2: Possible charge configurations for the Anderson impurity model.

The energy for the three possible charge states of the localized site are shown in Fig. 3.2. If the ground state corresponds to single occupation of the localized site, then the site will contain a net spin-1/2, which occurs when  $\epsilon_d < \epsilon_F$  and  $\epsilon_d + U > \epsilon_F$ .

The last term in Eq. 3.6 is an interaction term, which allows an electron to hop off the localized cite into the Fermi sea and a new electron to hop back on the localized cite from the Fermi sea. These processes can be described by second order perturbation theory, as shown in Fig. 3.3. In Fig. 3.3(a), the perturbation term is

$$\Delta H = - \sum_{k,k',\sigma,\sigma'} \frac{V_k^* V_{k'}}{U + \epsilon_d - \epsilon_{k'}} c_{k,\sigma}^\dagger c_{k',\sigma'} c_{d,\sigma} c_{d,\sigma'}^\dagger \quad (3.7)$$

In Fig. 3.3(b), the perturbation term is

$$\Delta H = - \sum_{k,k',\sigma,\sigma'} \frac{V_k^* V_{k'}}{\epsilon_k - \epsilon_d} c_{k',\sigma'} c_{k,\sigma}^\dagger c_{d,\sigma'}^\dagger c_{d,\sigma} \quad (3.8)$$

Notice these terms are second order processes that change the state of the system by temporarily involving an excited state. However, the initial and final states must have equal energy. The only place an electron can be readily added and removed is from the Fermi level, so the sum only include  $k = k_F$ . By adding equation 3.7 and 3.8 *coherently* and explicitly writing the spin operators, one can transform these terms into the Kondo Hamiltonian by using the Schrieffer-Wolff transformation.

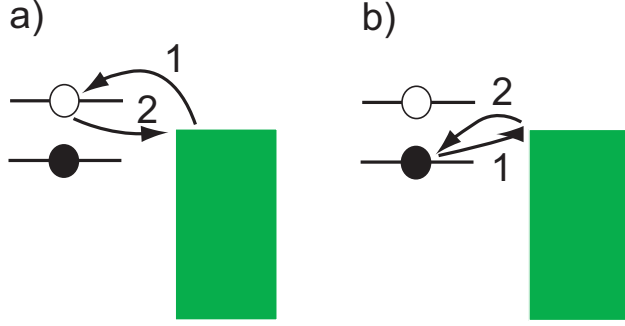


Figure 3.3:  $2^{nd}$  order perturbation processes in the Anderson model. In (a), the electron process is shown, and in (b), the hole process is shown.

With this model, the antiferromagnetic interaction term,  $J$ , is a sum of terms like

$$J \sim \frac{V_k^* V_{k'}}{\epsilon_F - \epsilon_d}, \quad (3.9)$$

which makes the parameters which determine  $J$  more approachable. The numerator of the equation 3.9 is a coupling between the local moment and the Fermi sea. It can be expressed as a tunnel rate,  $|t|^2 = V_k^* V_k$ . The denominator is a simple energy difference between the localized site and the Fermi level. In metals with magnetic impurities, these parameters are not measurable and thus were used as phenomenological parameters. In the next section, we demonstrate that new measurements not only allow these parameters to be measured, but also allow them to be tuned.

$T_K$  can be parameterized in terms of the Anderson model. By rewriting the depth of the impurity level in slightly different terms  $\epsilon_0 = \epsilon_d - \epsilon_F$  for the electron process and  $\epsilon_0 + U = U + \epsilon_d - \epsilon_F$  for the hole process, and the coupling to the leads as  $\Gamma = \pi\nu(0) |V|^2$  yields  $T_K$  in a more useful form [75],

$$T_K \sim e^{\pi\epsilon_0(\epsilon_0+U)/\Gamma U} \quad (3.10)$$

$\epsilon_0$  is negative in this form and  $\epsilon_0 + U$  is positive, so the overall exponential is negative as in Eq. 3.4. This form will be very useful for quantum dot measurement in the rest

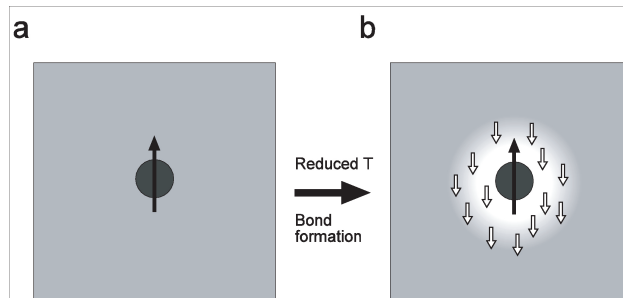


Figure 3.4: Drawing of increased scattering at low temperature due to Kondo effect.

of the dissertation.

Although abstract, the model applies well to magnetic impurities in metals. A magnetic impurity, for example iron, has 26 electrons. Some electrons will be donated to the conduction band of the metal, depending on the host metal properties. One or a few will remain in its outermost valence orbital, and this electron is then localized and energetically near the Fermi level. The magnetic impurity orbital then contains an electron and is spin degenerate. Spin is conserved in the host metal, so the Anderson Hamiltonian and the processes associated with it is valid.

Why does this increase resistance? The localized state described in the Anderson model will have a large zero point energy (tightly confined). The total energy of the system can be reduced if the localized electron is allowed to spread out, which occurs through bond formation with the conduction electrons. This effectively increases the size of the scattering center, and thus the amount of scattering, leading to an increase in resistance at low temperature, as shown in Fig. 3.4.

### 3.3 Quantum Dots as Artificial Impurities

As mentioned in section 2.1, the constant interaction model is very useful in describing a quantum dot. Using the same model as shown in Fig. 3.5(a), the quantum dot may also be mapped onto the Anderson model. The quantum dot provides a remarkable system to study a single, tunable magnetic impurity.

In fact, both the tunnel rate,  $\Gamma$  and the depth of the impurity level  $\epsilon_d$  (which determines  $\epsilon_0$  for the electron process and  $U + \epsilon_0$  for the hole process) are tunable with gates *sw1*, *sp*, and *sw2*. We use gate *sp* to change the energy of the quantum dot, and thus effect the depth of the level  $\epsilon_d$ , effecting  $\epsilon_0$  and  $\epsilon_0 + U$ . While both *sw1* and *sw2* also capacitively couple to the electrostatic energy of the dot, these gates also have a large influence on the tunnel rate into and out of the dot,  $\Gamma$ . The electrostatic energy of the dot is a linear function of gate voltage, while the tunnel rate into and out of the dot is an exponential function of the gates forming the barrier. Thus, in the quantum dot system, the depth of the impurity level can easily be tuned finely, while the tunnel rate is more delicate. The control of these parameters allows unprecedented control of the Anderson Hamiltonian, and in fact the antiferromagnetic coupling constant  $J$  from the Kondo model. From equations 3.10 and 3.4,

$$J\nu(0) = -\frac{\Gamma U}{\pi\epsilon_0(\epsilon_0 + U)}. \quad (3.11)$$

In order for Kondo effect to be observed, temperature must be smaller than  $T_K$ . Since  $T_K$  is exponentially dependent on  $\Gamma$  (Eq. 3.10), the dot must be well coupled to the leads (large  $\Gamma$ ). The Kondo regime in semiconductor quantum dots was pioneered by Goldhaber-Gordon in 1996 [28], and has since become an active area of research for many experimental and theory groups across the world.

Typical data for the Kondo effect is shown in Fig. 3.6. Varying gate *sp* not only

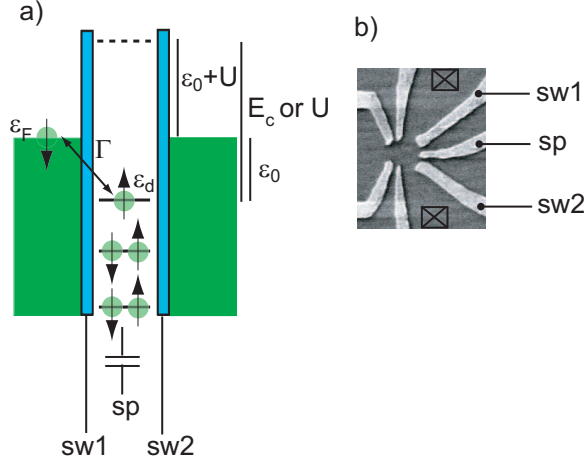


Figure 3.5: Drawing of quantum dot with Anderson model parameters. The charging energy,  $E_c$ , will be called  $U$  in the remaining dissertation when Kondo effect is important in the dot and  $E_c$  when Kondo effect is unimportant in the dot. The parameters of the Anderson model are  $\epsilon_d$  and  $\Gamma$ , which are controlled by  $sw1$ ,  $sw2$ , and  $sp$ . In (b), a scanning electron microscope image similar to the device measured is shown.

changes the depth of the impurity level, in these semiconductor quantum dot we can change number of electrons also. In Fig. 3.6, three consecutive electron numbers are shown corresponding to alternating even and odd electron number in the quantum dot. When there is a stable number of odd electrons in the quantum dot, the Kondo effect is clear. Instead of conductance near zero as in both the even CB valleys, conductance in the odd valley is dramatically enhanced, in this case  $g > e^2/h$ , completely masking the CB peaks. (The CB peaks are located at the location of each arrow in Fig. 3.6(a).)

The Fermi liquid Kondo state can be described as a normal Fermi sea superposed with a resonance (leading to Fermi liquid behavior described in section 3.1. Using this model, the enhanced conductance in the Kondo valley can be understood within scattering theory. Scattering an incoming electron wave off of a potential can be described as a phase shift,  $\delta_{l,\sigma}$ , (where  $l$  is the angular momentum index of the incoming

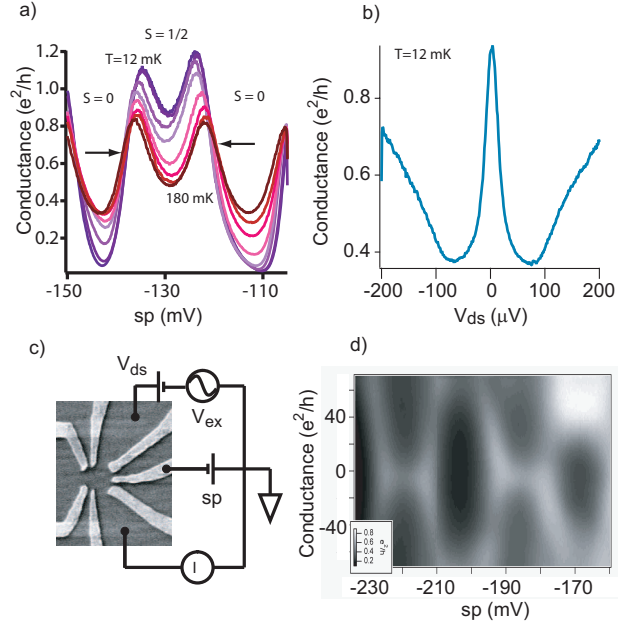


Figure 3.6: (a) Conductance trace for quantum dot at different temperatures in the Kondo regime. The CB valleys which rise in conductance as a function of temperature contain an even number of electrons and most likely have no net spin  $S = 0$ . In contrast, the odd electron valley,  $S = 1/2$ , conductance is very large at low temperature and actually decreases at temperature increases. In (b), the associated zero bias anomaly is shown for  $sp = -129\text{mV}$ . The general measurement setup is shown again in (c). In (d), a color plot of conductance as a function of both  $sp$  and  $V_{ds}$  is shown, although for slightly different gate voltages than (a) and (b).

wave and  $\sigma$  is the spin). According to the Landauer formula, conductance can be described as a transmission problem with the appropriate phase shift,

$$g = \frac{e^2}{h} T_{max} T_{\sigma}^{L \rightarrow R} = \frac{e^2}{h} \frac{4\Gamma_L \Gamma_R}{(\Gamma_L + \Gamma_R)^2} \sin^2(\delta_{l,\sigma}) \quad (3.12)$$

where  $T_{max}$  is the maximum conductance due to asymmetric coupling of the leads,  $\Gamma_L$  and  $\Gamma_R$ . When  $\Gamma_L = \Gamma_R$ ,  $T_{max} = 1$  and the conductance is maximum.

Amazingly, only a single phase shift is needed to describe low temperature transport through the quantum dot, even when a complex many-body Kondo state has formed. The Friedel sum rule allows the phase shift to be calculated. It states the change in number of electrons from the lattice must be equal to the excess charge of the impurity,

$$\Delta N = \frac{1}{\pi} \sum_{l,\sigma} (2l+1) \delta_{l,\sigma} \quad (3.13)$$

When considering a quantum dot as the impurity scatterer,  $\Delta N$  can be characterized as the occupation of the dot,  $n$ . The quantum dots studied here are connected to the Fermi reservoirs via single mode leads, so we explicitly need only to consider the  $l=0$  case. The Friedel sum rule now becomes tractable,

$$n_{\sigma} = \frac{1}{\pi} \delta_{0,\sigma} \quad (3.14)$$

First consider a Lorentz broadened resonance (CB peak). At the resonance, occupation of localized site can be 0 or 1. At the charge degeneracy point, occupancy,  $n_{\sigma}$ , takes the value 1/2.  $n_{\sigma} = n_{\uparrow} + n_{\downarrow}$  and  $n_{\downarrow} = n_{\uparrow}$  (spin degeneracy), so  $n_{\uparrow} = n_{\downarrow} = 1/4$ . Now,  $T_{\downarrow}^{L \rightarrow R} = \sin^2(\pi/4) = 1/2$  (same for  $T_{\uparrow}^{L \rightarrow R}$ ). Thus,  $g = (\frac{1}{2} + \frac{1}{2})e^2/h = e^2/h$  for symmetric coupling (maximum conductance of a CB peak). In contrast, in a Kondo valley,  $n = 1$  and  $n_{\uparrow} = n_{\downarrow} = \frac{1}{2}$ . Thus,  $T_{\uparrow} = T_{\downarrow} = \sin^2(\pi/2) = 1$ , so  $g_{max} = 2e^2/h$ . In the case of a quantum dot, the Kondo effect actually enhances conductance, the exact opposite of metals.

In the quantum dot, all current that flows must transmit through the quantum dot. Considering the Anderson model and Fig. 3.5, screening of the local moment occurs through exchange events with the leads. These exchange events include the localized electron hopping off to the right and a new electron hopping on from the left. Thus, enhanced scattering due to Kondo effect enhances transport across the quantum dot.

Although the two leads in Fig. 3.5 are physically separated, they can be straightforwardly transformed into only a single Fermi reservoir like the original Anderson Hamiltonian, Eq. 3.6. The Hamiltonian describing Fig. 3.5 is

$$H = \sum_{\sigma} \epsilon_d n_{d\sigma} + U n_{d\uparrow} n_{d\downarrow} + \sum_{k\sigma} \epsilon_k a_{k\sigma}^{\dagger} a_{k\sigma} + \sum_{k\sigma} \epsilon_k b_{k\sigma}^{\dagger} b_{k\sigma} + \sum_{k\sigma} \left( V_a c_{d\sigma}^{\dagger} a_{k\sigma} + H.c. \right) + \sum_{k\sigma} \left( V_b c_{d\sigma}^{\dagger} b_{k\sigma} + H.c. \right)$$

where now  $a_{k\sigma}^{\dagger}$  corresponds to adding an electron to the right reservoir and  $b_{k\sigma}^{\dagger}$  corresponds to adding an electron to the left reservoir, and the coefficients  $V_a$  and  $V_b$  are constants of hybridization for the right and left reservoirs, respectively. Glazman [76] provided the appropriate rotation

$$\alpha_{k\sigma} = u a_{k\sigma} + v b_{k\sigma} \quad \beta_{k\sigma} = u b_{k\sigma} - v a_{k\sigma} \quad (3.15)$$

where

$$u = V_a/V, \quad v = V_b/V, \quad V = (|V_a|^2 + |V_b|^2)^{1/2}. \quad (3.16)$$

With this rotation, two different fermion species (or screening channels) now exist,  $\alpha$  and  $\beta$ . The  $\alpha$  electrons constructively interfere to have a maximum probability in the dot center (even wavefunction with respect to the dot). This species alone couples to localized moment and undergoes Kondo screening. The  $\beta$  channel is odd with respect to the local moment and thus does not couple to the moment. Since only a single conduction channel screens the spin of the quantum dot, this effect is known as a

single channel Kondo (1CK) effect. In fact, any arbitrary number of leads attached in this way can be transformed into a single screening channel.

In section 3.1, two regimes of resistivity for metals with magnetic impurities were presented: the high temperature regime ( $T \sim T_K$ ) where resistivity increases like  $\log(T)$  and the low temperature ( $T \ll T_K$ ) regime where resistivity falls to a constant value as  $\rho_0 - cT^2$ . Since Kondo effect in quantum dots enhances conductance, the exact opposite trends occurs as temperature is reduced, a  $\log(T)$  increase in *conductance* then conductance saturates like  $g_0 - cT^2$ . Exact numerical results for intermediate temperatures were provided by Costi [69]. This dependence was fit by the analytical form [77],

$$g(T) = g_0 \left( \frac{T_K'^2}{T^2 + T_K'^2} \right)^s = g_0 F(T/T_K), \quad (3.17)$$

where  $T_K' = T_K / \sqrt{2^{1/s} - 1}$  so that  $g(T_K) = G_0/2$ . The value of  $s$  sets the slope of the logarithmic part of the conductance and is predicted  $s = 0.22 \pm 0.01$  for  $S = 1/2$ . This temperature dependence is a unique characteristic of the Kondo effect.

Another hallmark feature of the Kondo effect is the enhanced density of states at the Fermi level. Because we are studying a single magnetic impurity, the local enhanced density of states can be probed because the chemical potential,  $\mu$ , of both the left and right reservoir can be controlled (see Fig. 3.7). When applying a drain source bias voltage,  $V_{ds}$ , most of the voltage is dropped across the device, shifting the chemical potential of the reservoirs with respect to each other.

Since the enhanced density of states is pinned to the Fermi level of each reservoir, enhanced conductance is observed only when the effective Fermi level of each reservoir is equal, or  $\mu_{left} = \mu_{right}$ . The enhanced density of states can then be mapped as a function of energy by applying  $V_{ds}$ , as shown in Fig. 3.6(b). The width of the zero bias anomaly (ZBA) gives an indication of  $T_K$ . In (b), the FWHM is  $\sim 15\mu V$ , corresponding

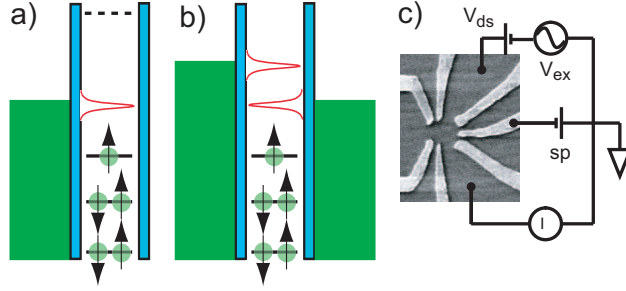


Figure 3.7: Kondo effect produces an enhanced density of states at the Fermi energy (a). Applying a d.c. source drain bias, as in (c), raises the chemical potential of one reservoir (b). The enhanced density of states of the left and right reservoir no longer align, and thus the conductance reduces, as in Fig. 3.6(b).

to  $T_K \sim 200mK$ . Due to decoherence mechanisms which occur with the application of  $V_{ds}$ , the width of the ZBA does not yield a very accurate measure of  $T_K$ . Instead, temperature dependence of the zero bias conductance is the preferred manner, which is discussed in the next section. In (d), conductance as a function of both  $sp$  and  $V_{ds}$  is shown for a complete picture of Kondo effect in a quantum dot. Here,  $sp$  varies the occupation of the quantum dot from even, odd, even, odd, even. The odd valleys have enhanced conductance at  $V_{ds} = 0\mu V$ . By adding a third, weakly coupled lead, it is possible to probe the enhanced density of states out of equilibrium, see section 3.5.

### 3.4 Kondo Effect in a Three Lead Quantum Dot

With the three lead geometry in Fig. 3.8(a), several properties of the Kondo effect can be probed. In this section, we present results for the equilibrium conductance measurements which show behavior consistent with a conductivity matrix. In addition, we show for the first time all leads of the quantum dot cooperate to form a single Kondo bond with characteristic Kondo temperature  $T_K$ , independent of the asymmetry of

coupling to various leads. This observation is consistent with the prediction of Glazman [76] mentioned in the previous section (two reservoirs (or leads) to a quantum dot cooperate to form a single Kondo effect).

In (a), a typical measurement setup is shown. An ac voltage source with excitation  $2\mu eV$  is attached to one lead and a current amplifiers is attached to each of the other two leads of the quantum dot. Conductances in Fig. 3.8 are derived by dividing current through lead by the voltage excitation. For example, in Fig. 3.8(b), the red trace is given by  $g_5 = I_5/V_{ex} = G_{21}$ , the blue trace is given by  $g_{24} = I_{24}/V_{ex} = G_{31}$ , and the black trace is given by  $g_{28} = (I_{24} + I_5)/V_{ex} = G_{11}$  (current conservation). By rotating the voltage source and current amplifiers to the various leads various conductances can be measured, Fig. 3.8(b)-(d). Exchanging the two current amplifiers between the same two leads yielded the same conductance, meaning our current amplifiers were well calibrated to each other.

The conductance traces in 3.8(b)-(d) show two Kondo valleys near  $sp = -230mV$  and  $sp = -270mV$ . The conductances, however, are dramatically different through the three leads. The conductance through a Kondo valley is expected to be effected by the asymmetry[76],

$$G_{ij} \propto \frac{\Gamma_i \Gamma_j}{\Gamma} F(T/T_K) \quad (3.18)$$

where  $\Gamma_{i(j)}$  is the coupling to the  $i$ th ( $j$ th) lead and the total coupling,  $\Gamma$  is given by  $\Gamma = \Gamma_1 + \Gamma_2 + \Gamma_3$ .  $F(T/T_K)$  is the universal function in Eq. 3.17.

In linear response theory, the conductivity of a three lead device can be described by the conductivity matrix [78, 79],

$$\begin{pmatrix} I_1 \\ I_2 \\ I_3 \end{pmatrix} = \begin{pmatrix} -G_{11} & G_{12} & G_{13} \\ G_{21} & -G_{22} & G_{23} \\ G_{31} & G_{32} & -G_{33} \end{pmatrix} \begin{pmatrix} V_1 \\ V_2 \\ V_3 \end{pmatrix} \quad (3.19)$$

The values of the conductivity matrix at every point in  $sp$  are provided by Fig. 3.8(b)-(d) or (f)-(h). The conductivity matrix has two important properties. First, current conservation requires the columns to sum to zero, eg.  $G_{11} = G_{21} + G_{31}$ . We force this constraint by the definition of  $G_{11}$  above. There is a second constraint on the matrix. If all voltages are set to the same value, no current should flow. This forces each row of the matrix to sum to zero also, for example  $G_{11} = G_{12} + G_{13}$ . The extent to which this is obeyed is shown in Fig. 3.8(e) and (i). The normalized difference,  $(G_{11} - (G_{12} + G_{13}))/G_{11}$ , is shown over a large range in  $sp$  for all three rows of the matrix. For most values of  $sp$ , the error in the conductivity matrix is less than 20%. As expected, linear response theory works whether an even number (no Kondo effect) of electrons or an odd number of electrons (Kondo effect) exist in the quantum dot.

Although the conductance through a particular set of leads is proportional to the asymmetry between the leads, Eq. 3.18, the temperature dependence,  $F(T/T_K)$ , and specifically  $T_K$  is not expected to be dependent on the leads measured. This is because  $T_K$  is determined by the total coupling to the leads,

$$T_K \sim e^{\epsilon_0(\epsilon_0+U)/\Gamma U} \quad (3.20)$$

where  $\Gamma$  is the total coupling  $\Gamma = \sum_i \Gamma_i$  to all  $i$  leads.

In Fig. 3.9, we demonstrate a three lead quantum dot has single valued  $T_K$  independent of the leads measured through. In order to minimize the effects of voltage dividing due to the three lead geometry, we ground one of the leads through  $1G\Omega$  (the other two leads serve as source and drain). The lead grounded though  $1G\Omega$  still participates in Kondo screening, however very little current flows through that lead. Conductance as a function of temperature is then measured, as in Fig. 3.9(a), then rotated for Fig. 3.9(b) and (c). We did confirm switching the source and drain leads while leaving the  $1G\Omega$  lead unchanged yielded the same conductance trace.

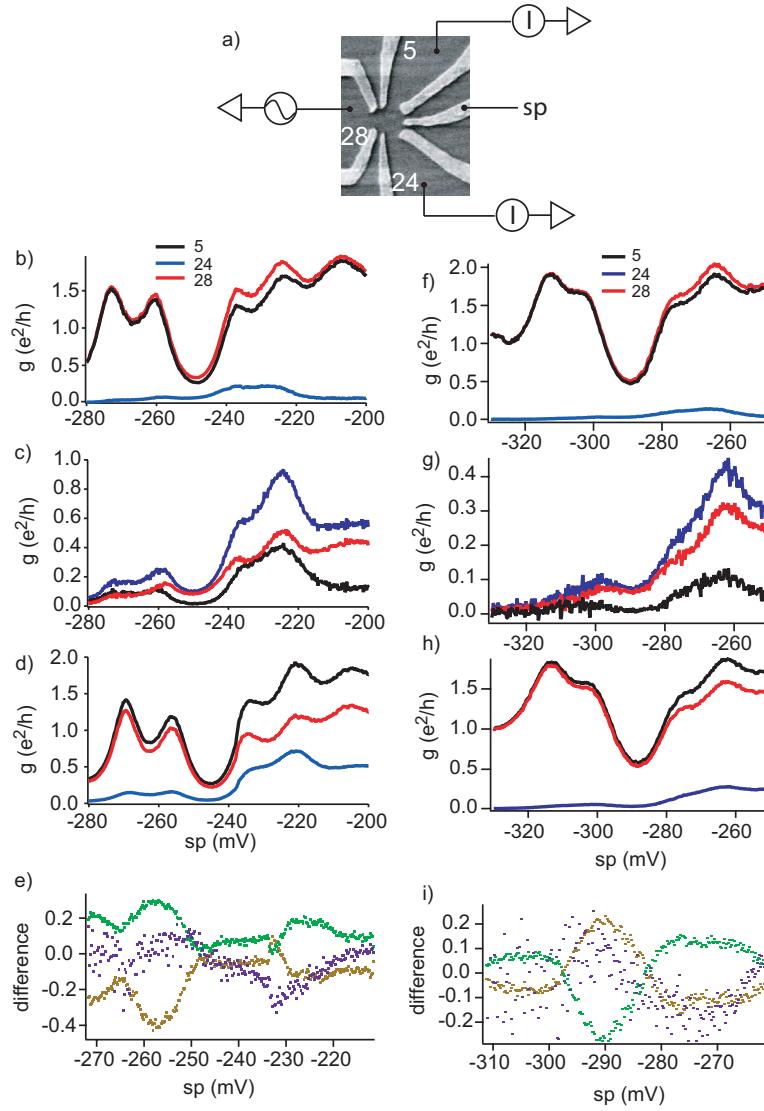


Figure 3.8: In (a), a voltage source is attached to one lead (on reservoir 28 in this case) and two currents are measured (reservoir 24 and 5 in this case). This exact measurement is shown in (b), the red curve corresponds to the conductance through lead 5 (defined in text), the blue curve corresponds to the conductance through lead 24, and the black curve is the conductance through lead 28, which is just the sum of the two conductances (red and blue curves). For (c) and (d), the colors correspond to the conductance through the same leads as (a), however now the measurement setup has now rotated so the source is on lead 24 and lead 5, respectively. Here, lead 24 clearly has the smallest coupling,  $\Gamma_{24} \ll \Gamma_{28}, \Gamma_5$ . In (e), the deviation from the conductivity matrix is plotted (see text). (f)-(h) Same conductance measurements as (b)-(d) except with different gate voltages on surrounding gates. In (i) the deviation from the conductivity matrix for (f-h) is shown.

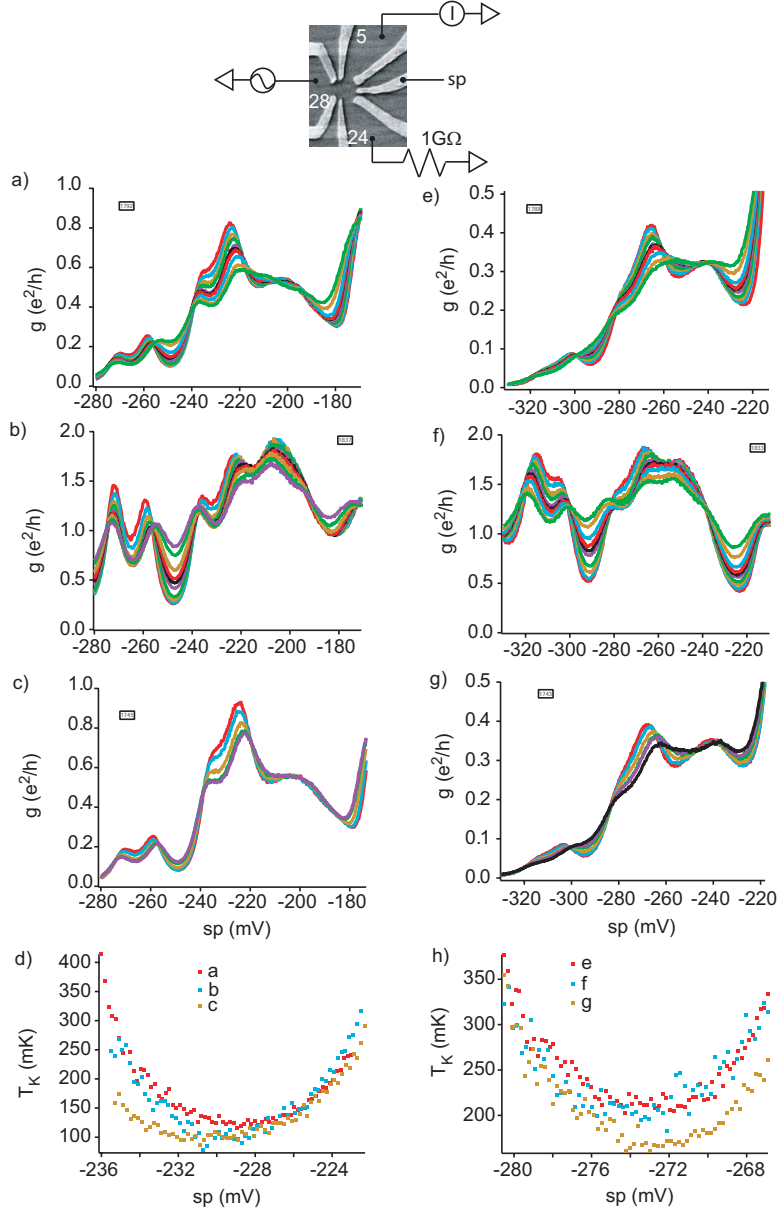


Figure 3.9: Measurement of a single bond energy  $T_K$  through three different combinations of leads. Measurement setup is shown at the top. A ac excitation of  $2\mu V$  is applied to a lead and a current amplifier is attached to another lead. The third lead is grounded through  $1G\Omega$ . Conductance is then measured as a function of temperature and  $sp$  for the three different configurations, (a)-(c), from 12mK to 150mK. In (d), the extracted  $T_K$  is shown as a function of  $sp$  for one Kondo valley. In (e)-(g), conductance as a function of  $sp$  and temperature is shown for different gate voltages on the surrounding gates. Again,  $T_K$  is independent of the two leads it is measured through.

For the fit of conductance as a function of temperature to Eq. 3.18 to converge properly, we needed to add a constant offset,

$$g(T) = g_0 F(T/T_K) + a, \quad (3.21)$$

where  $a$  is a constant as a function of temperature. Although the original paper [77] did not require a constant offset, we since have learned it is common in other groups to use Eq. 3.21 to fit data. We have found the constant offset to be dependent to the leads measured through and can be as large as half the total conductance. In these fits,  $s = 0.22$  as expected for  $S = 1/2$  ( $s$  sets the slope of the logarithm).  $g_0$ ,  $T_K$  and  $a$  are left as fitting parameters.  $a$  is also found to be relatively constant over the Kondo valley (independent of  $sp$ ), for instance in (a)  $a = 0.2$ , in (b)  $a = 0.75$  and in (c)  $a = 0.21e^2/h$  for all  $sp$ .

These measurements confirm a single valued  $T_K$  for the three lead quantum dot. The origin of the constant offset is still unknown, however it is possible it is due to charge fluctuations due to the large coupling of the dot to the leads ( $\Gamma$  near  $\Delta$ ) [80].

### 3.5 The Kondo Effect Out of Equilibrium

In this section, we show transport measurements of a small three lead *GaAs* quantum dot in the Kondo regime. In the three lead geometry, we operate with one lead more weakly coupled to its reservoir than other two, which permits it to be used as a probe of the two other, more highly coupled leads ( $\Gamma_{24} \ll \Gamma_{28}, \Gamma_5$ ). Although CB and Kondo physics is readily visible measuring through the two strongly coupled leads, measuring the same through the third, weakly coupled lead displays far different behavior from CB peak to CB peak, possibly indicating substantial differences of coupling of a wavefunction to the three leads of the quantum dot. In a CB valley with clear Kondo

behavior, we demonstrate that the third, weakly coupled lead can be used as a probe of the out of equilibrium density of states due to Kondo resonances of the other two leads.

Fig. 3.10(a) displays the measurement setup, along with typical conductance traces in Fig. 3.10(b, upper). However, when measuring through the third lead, Fig. 3.10(d, upper), we do not observe all of the features of as in Fig. 3.10(b, upper). From the previous section, features in the conductance should not be expected to appear with the same relative magnitude through the third lead. Each wavefunction of the electron entering the dot should have independent coupling to the three leads, depending mainly on whether the wavefunction has a high or low probability magnitude near each of the leads. This is expected to fluctuate randomly from wavefunction to wavefunction in a chaotic dot (the extent to which this dot is chaotic is unknown, though).

In our dot, a very striking feature in the conductance, marked by the green arrow, is completely missing from the conductance of the third lead. This occurs over a wide range in  $sw1$  and  $sw2$ . We believe this feature to be a Kondo valley based on source-drain bias measurement (although temperature dependence would be needed to confirm). However, if it is a Kondo valley, it is hard to say it contains an odd electron number based on the measurements presented (the valleys seemingly go Kondo, no Kondo, no Kondo, Kondo). Also, if the feature is Kondo, then it would correspond to two wavefunctions being extremely poorly coupled to the third lead. This may be expected, though, because in the Kondo valley, a spin degenerate state is needed, thus two consecutive wavefunctions must have the same spatial distributions.

Using the easily identifiable Kondo valley in Fig. 3.10(b) and (d), we measure enhanced density of states (DOS) out of equilibrium. Here, changing  $V_{lead3,d}$  moves the chemical potential of that lead, hence allowing us to probe the DOS of the quantum

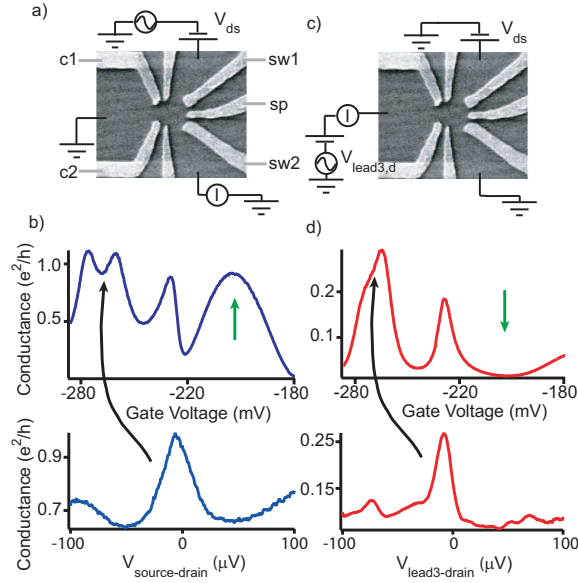


Figure 3.10: (a) SEM image of three lead device. (b, upper) Measurement of CB as a function of gate voltage ( $V_g$ ), and all measurements are performed in 150mT  $B_{\perp}$ . The measurement is set up as in (a), with zero  $V_{ds}$  and the weakly coupled lead (left lead) is grounded. (b, lower) Measurement of enhanced conductance of Kondo in the valley referenced by the black arrow. Using the same device with the same voltage on all gates, we measure the conductance through the third lead, as shown in (c). With  $V_{ds} = 0$  and  $V_{lead3,d} = 0$ , (d, upper) displays conductance as a function of ( $sp$ ). Though reduced in magnitude because the third lead is weakly coupled, many of the same features are observed. However, some, such as the feature marked with a green arrow, do not appear, see text. In (d, lower) the enhanced zero bias conductance of Kondo for the same  $sp$  as (b, lower) is shown.

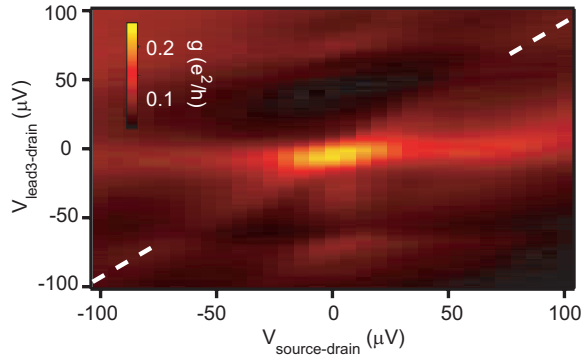


Figure 3.11: Conductance as a function of  $V_{ds}$  and  $V_{lead3,d}$  using the same measurement scheme and CB peaks as Fig. 1c and d. The ZBA of  $V_{lead3,d}$ , splits into two peaks as a function of  $V_{ds}$ , with one peak at  $V_{lead3,d} = V_{sd}$  and another at  $V_{lead3,d} = 0$ . The splitting of the ZBA displays the enhanced density of states of Kondo out of equilibrium (dashed line is a guide to the eye).

dot. In the Kondo valley at  $V_{ds} = 0$ , the conductance is dramatically enhanced at  $V_{lead3,d} \sim 0$  due to Kondo correlations creating an enhanced density of states at the Fermi level. As  $V_{ds}$  is changed from zero, the third lead will see an enhanced transport corresponding to the enhanced density of states in each of the source and drain leads, as shown in Fig 3.11. This is the first direct measure of the enhanced density of states of two different leads of a quantum dot. (Previously, one experiment has measured the Kondo effect out of equilibrium by splitting the enhanced DOS of a single lead[81].)

Noteworthy, the features at  $V_{lead3,d} = V_{sd}$  and  $V_{lead3,d} = 0$  are not the same height. This may be expected, as the coupling of the third lead to the source and drain reservoirs may be different. We expected to change the relative height of the these peaks by simply tuning  $sw1$  and  $sw2$ , however this is not the case experimentally. In fact, this is the most equal we could make the two features (this is the best case data). This may be an extension of the physics mentioned earlier, where the couplings of the third lead to the source and third lead to the drain is set more by the wavefunction than by the barrier heights. Changing  $sw1$  and  $sw2$  does not enhance the smaller peak at

$V_{lead3,d} = V_{sd}$  in any consistent manner. Although the above logic seems to describe what we see experimentally, it may seem more reasonable to consider if source is well coupled to drain, and third lead is well coupled to drain, then the source should be well coupled to the third lead due to a single valued wavefunction in the dot.

The initial goal for this experiment was to find a method to balance the Kondo coupling between the two leads, a necessity for the two channel Kondo experiment (presented in the next chapters). The relative height of the enhanced conductance of each peak at finite  $V_{ds}$  is expected to yield information about the couplings, [82] and Fig. 3.12. Because the out of equilibrium Kondo correlations in this regime do not depend highly on  $sw1$  and  $sw2$ , we abandoned this method. However, it is possible with a more open third lead, the Kondo coupling will be easier to balance and be more effected by the gates  $sw1, sw2$ .

Recently, there has been another experiment performed to measure the Kondo effect out of equilibrium [83]. However, this experiment also did not make a quantitative measure of the enhanced density of states out of equilibrium. The Kondo effect out of equilibrium is both an interesting and active area of theoretical research, so follow-up experiments should be performed for a quantitative comparison with theory.

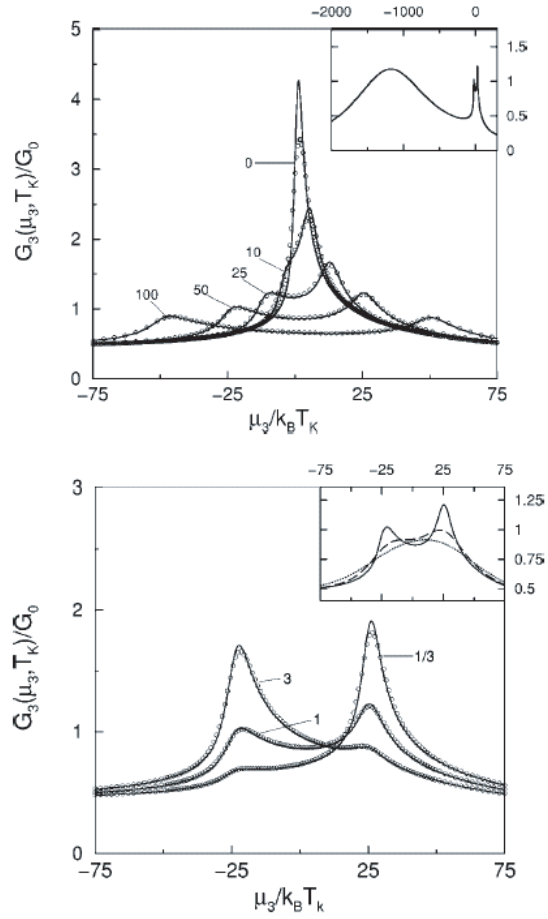


Figure 3.12: From [82]. Calculation of the conductance of a quantum dot in the Kondo regime probed with a third, weakly coupled lead as a function of  $V_{ds}$  across the two strongly coupled leads (top). At fixed finite bias (bottom), the effect of an asymmetry in the  $\Gamma$ 's is the enhance (reduce) the peak at the chemical potential of the more strongly (weakly) coupled lead.

# Chapter 4

## Background of the Single Channel and Two Channel Kondo Problem

Since the Kondo effect was first observed in *GaAs* quantum dots in 1998[28], a variety of new materials such as molecules[66, 67], nanotubes[65], and metal grains[84] have revealed signatures of the Kondo effect. In the mean time, the flexibility of *GaAs* nanostructures have allowed a variety of new, exotic Kondo effects to be studied. In section 4.1, we review some of the major experimental developments in producing and studying variety of different Kondo effects that occur in *GaAs* quantum dots and carbon nanotube quantum dots. In section 4.2, basic theory of two channel Kondo effect is presented and the differences from single channel Kondo are highlighted. Finally, in section 4.3, proposed experimental realizations of the 2CK effect in materials are discussed.

## 4.1 Prior Kondo Variants in Quantum Dots

To date, only a few examples of exotic Kondo states in nanostructures have been examined, but each has revealed exciting results. Sasaki *et al.* [85] demonstrated that a single-electron transistor with a near-degeneracy between two spin states (singlet and triplet) displays a Kondo effect. A triplet state generally involves exciting an electron from its lowest-energy orbital state to a higher orbital state. The device, shown in Fig. 4.1(a), was fabricated to have rotational symmetry, and thus degeneracy of two or more spatial states. This removed the large energy cost of forming a triplet, enabling easy experimental access to the singlet-triplet transition. In fact, near the magnetic field-tuned singlet-triplet transition the Kondo effect is much stronger than it was for the triplet alone at zero magnetic field. Presumably the enhancement is due to the multitude of possible transitions among the various spin states. This phenomenon had not been previously considered, but may provide insight into the  $S = 1$  many-body Kondo state [86].

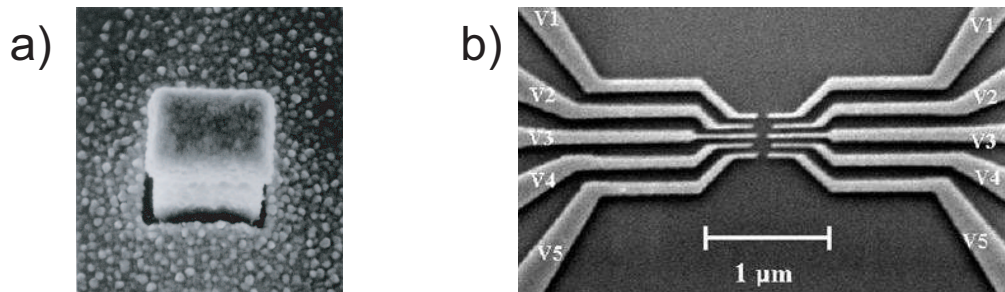


Figure 4.1: a) A vertical quantum dot was fabricated in a symmetric (square) shape so as to display near-degeneracies in its spectrum of single-particle spatial states [85]. A slight magnetic field produced singlet-triplet degeneracy, resulting in an unanticipated 'singlet-triplet' Kondo effect. b) A realization of the two-impurity Kondo effect in semiconductor nanostructures, using electrostatic gates to define a series-coupled double quantum dot [87].

The starting point for any Kondo system is a local degenerate state coupled to conduction electrons. The degeneracy usually arises from a local spin, but other discrete quantum numbers can serve just as well. Recently this was experimentally demonstrated by Schmid *et al.* [88, 89], who used two electrostatically-coupled quantum dots tuned to have a single extra electron in the double-quantum dot system, as in Fig. 4.2. This extra electron may be located on either quantum dot. Correlated tunneling events between the surrounding conduction electrons and the artificial quantum dot molecule collectively screen this electrostatic degeneracy, producing the same effect as screening excess spin in the classic Kondo system. Transport experiments revealed signatures of the classic Kondo effect, demonstrating that we may expect correlated Kondo-like behavior from a much larger variety of nanostructures, including those without a localized spin.

The achievement of a Kondo effect without spin degeneracy was also recently discovered in carbon nanotubes and single *GaAs* quantum dots [90] [91]. Though involving very different materials, they both used a single site with two degenerate orbital states as the localized ‘magnetic impurity’. Here the degeneracy stems from a spatial symmetry in the device, either associated with underlying material structure (Fig. 4.2(c)) or created by nanoscale patterning (Fig. 4.2(b)). In these experiments, a Kondo effect can occur because the local degree of freedom is also reflected in the leads. If the spin of an electron on a traditional magnetic impurity is pointed up, a nearby delocalized electron will direct its spin down in response. Similarly, if there an extra charge on the top site of Fig. 4.2(a), an electron in the leads will move to the bottom.

The unique structure of the carbon nanotube allowed an even more exotic Kondo effect to be observed. An engineered orbital degeneracy does not preclude spin degeneracy. The localized spin can be screened by the spin of surrounding delocalized

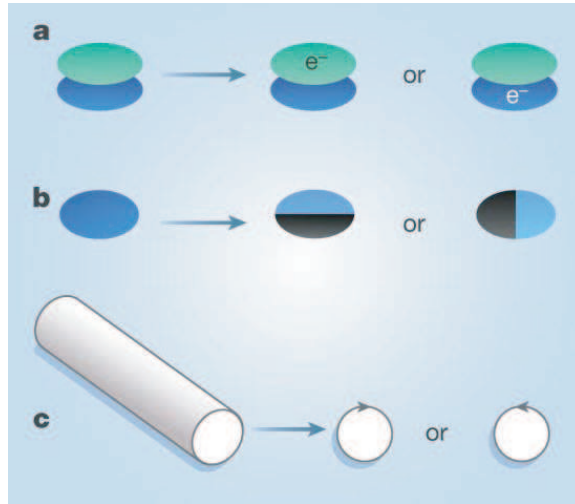


Figure 4.2: The foundation of the Kondo effect is screening of a localized two-fold degeneracy by surrounding delocalized electrons (see text). The degeneracy normally comes from spin, but with the advent of nanotechnology, researchers can create and study other types of degeneracy. In (a), an electron can reside on either of two sites, but not both simultaneously due to Coulomb repulsion [89]. In (b) and (c), a spatial symmetry produces degenerate orbital levels. In (b), the symmetry is the rotational symmetry of a circular quantum dot, defined by lithography [91]. This is analogous to the rotational symmetry of a hydrogen atom which produces degenerate p orbitals. In (c), the lattice symmetry of a nanotube gives rise to a two-fold orbital degeneracy [90]. Non-spin degeneracy may also give rise to Kondo in bulk systems.

electrons, while the local orbital state is also screened by the charge of those same delocalized electrons. Since the same delocalized electrons perform both spin and charge screening, the two degrees of freedom become intimately connected together forming a new 4-fold degenerate Kondo effect.

In an ideal nanotube, sets of four electronic states can be grouped together into a shell, much like those of atoms. All four states in a shell are degenerate, with two choices for spin and two for orbital state. Electrons can be added one at a time to the shell by fine control of the voltage on a nearby electrode. The first electron can reside in any of four states. Metal leads act like the host metal of a magnetic impurity,

producing a 4-fold Kondo system. If we add a second electron to the nanotube, the Kondo effect vanishes, suggesting that the two electrons form a unique nondegenerate ground state. The 4-fold Kondo effect returns with the addition of a third electron, since now any one of the four states can be left empty. A fourth electron completes the shell, removing all degeneracy and thus eliminating the Kondo effect.

In experiments, Kondo effect is generally identified by a distinctive logarithmic temperature dependence of resistance. The predicted (and now observed) temperature dependence of 4-fold Kondo is indistinguishable from that of conventional 2-fold Kondo, but the two systems respond very differently to magnetic field. Applying a magnetic field breaks both spin and orbital degeneracy, but the strength of the two responses is different. Thus, the state that gives rise to 4-fold Kondo splits into four: two increasing in energy and two decreasing in energy as a function of magnetic field. As described in Figure 4.3, applying a magnetic field also creates and breaks a variety of degeneracies among nanotube electron states. In all, Jarillo-Herrero *et al.* observed four types of Kondo physics, associated with different degeneracies, in a single nanotube [90].

Other Kondo states may be explored by departing from the standard geometry of a single-electron transistor. Jeoung *et.al* [87] first created and studied a two-impurity Kondo state by joining two artificial atoms in series, as shown in Fig. 4.1b. In this “artificial molecule”, they observed signatures of Kondo effect, including a zero-bias anomaly in conductance, when the occupancy of each of the two artificial atoms was odd. Though experimentally the system behaves similarly to a classic Kondo system, theory suggests that this Kondo molecule may show an unusual stable  $\pi/4$  scattering phase shift [92].

In a more complicated device shown in Fig. 4.4, Craig *et.al* [93] also demonstrated data consistent with two impurity Kondo effect. The two impurity Kondo effect in-

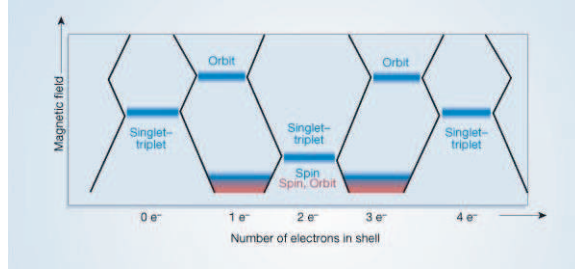


Figure 4.3: For any number of electrons in a shell of a nanotube, the low-energy states can be identified. At zero magnetic field, a shell with either one or three electrons displays a fourfold degeneracy, giving rise to a novel fourfold Kondo effect (red). Applying a magnetic field first breaks orbital degeneracy, reducing fourfold Kondo to conventional twofold spin Kondo (blue), and then destroys even the twofold spin Kondo. Higher magnetic fields can bring together electronic states that were not degenerate at zero magnetic field, producing a variety of Kondo effects for both even and odd electron occupancy. Although all these Kondo effects are twofold (blue), none emerges from conventional spin degeneracy. Their various origins are explained in [90].

volves two magnetic impurities separated by some distance. The Hamiltonian will then look like two independent magnetic impurities interacting with the same reservoir,

$$H_{2imp} = J_1 s(r - r_1) \cdot S_1 + J_2 s(r - r_2) \cdot S_2, \quad (4.1)$$

where  $J_1$  ( $J_2$ ) is the antiferromagnetic interaction with magnetic impurity  $S_1$  ( $S_2$ ) and  $s(r - r_1)$  ( $s(r - r_2)$ ) are the spin of the surrounding conduction electrons participating in screening. The two magnetic moments,  $S_1$  and  $S_2$ , can interact through the conduction electrons if the magnetic impurities are close enough together. This interaction is known as RKKY interaction and is described by the Hamiltonian

$$H_{RKKY} = K S_1 \cdot S_2 \quad (4.2)$$

This interaction arises from interacting the two Kondo screening clouds, however the sign of the RKKY interaction depends on the distance between the impurities. (In fact,

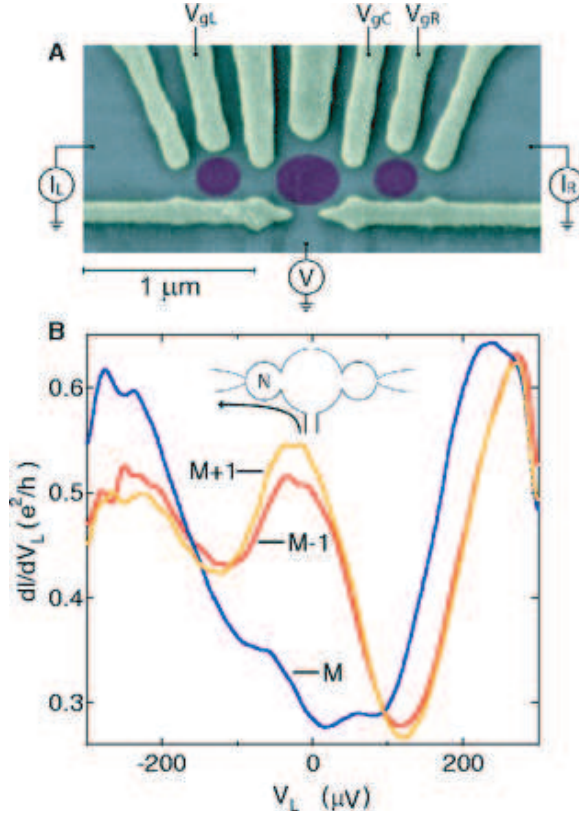


Figure 4.4: Possible realization of RKKY in two quantum dots. In (a), a scanning electron microscope image of the device is shown. With both quantum dots behaving like artificial magnetic impurities, the enhanced conductance at the Fermi level measured through one quantum dot can be suppressed adding an electron to the right dot.

the sign of the interaction oscillates between antiferromagnetic and ferromagnetic with period of half the Fermi wavelength.)

There is then a competition between two different states – Eq. 4.1 suggests the two magnetic moments may be screened separately by the conduction electrons (forming two separate spin singlet states). However, if  $K > J$ , (say  $J = (J_1 + J_2)/2$ ) then the two magnetic impurities together form one singlet or triplet state, an RKKY correlated state. The singlet state is expected not to show features of the Kondo effect, as there is no longer a spin  $S = S_1 + S_2 = 0$ . In [93], the ratio  $K/J$  is tunable, and they observe

behavior consistent with two independent Kondo states and the RKKY correlated state. The transition between the two states (state 1:  $K > J$  RKKY, state 2:  $J > K$  Kondo) is a quantum phase transition. However, in contrast to the two channel Kondo model presented in the next section, the critical point  $K = J$  does not show non-Fermi liquid behavior.

As we have seen, researchers can unambiguously identify several-electron states in nanostructures and even manipulate those states. Electrons in nanostructures can then be mapped explicitly onto simple microscopic models, which successfully predict a variety of novel correlated-electron behavior. In coming years, expect to see researchers building realizations of more complex models and studying phenomena at the center of modern condensed matter theory, such as other quantum phase transitions [87, 93] and decoherence.

## 4.2 Properties of the Two Channel Kondo Effect

Another superficially-similar exotic Kondo system, two-channel Kondo, is predicted to exhibit a strongly-correlated non-Fermi liquid ground state [31, 37, 94]. In this section, we review the properties of the multichannel Kondo problem, emphasizing the important differences of the two channel case.

The multichannel Kondo problem was first introduced by Nozieres and Blandin in 1980 [29] and independently by Zawadowski [95]. In its most generic form, it involves a localized spin of arbitrary size coupled to an arbitrary number of conduction electron bands, or screening channels. The Hamiltonian is then just an extension of Eq. 3.2,

$$H_{int} = \frac{J}{N} \sum_{k,k',\sigma\sigma'} \sum_{\alpha=1}^M S_I \cdot c_{k\sigma\alpha}^\dagger c_{k'\sigma'\alpha} \sigma_{\sigma\sigma'} \quad (4.3)$$

where now we have added an channel index for  $M$  different (but identical) conduction

bands and the localized spin  $S_I$  can now be any integer multiple of  $1/2$ . All channels contain normal spin- $1/2$  electrons.

There are three cases for the multichannel Kondo Hamiltonian, shown in Fig. 4.5[37]. In terms of multichannel Kondo physics, case (a) and (b) are equivalent. Entropy is an important quantity used to distinguish the three cases, where entropy is given by the logarithm of the degeneracy ( $\Omega$ ) of the state,  $k \ln(\Omega)$ . The third law of thermodynamics states entropy must go to zero as temperature goes to zero. Normally there is a nondegenerate ground state for a system at zero temperature (satisfying the third law). However, in the multichannel Kondo problem, residual entropy appears and has even possibly been measured.

The normal single channel Kondo effect is represented in Fig. 4.5(a) – a spin  $1/2$  ( $S_I = 1/2$ ) coupled to single channel  $c_1$  of conduction electrons. At low temperature, the spin is completely screened, or compensated. Because the spin is completely screened, entropy tends to zero at zero temperature. The same happens for all combinations where the channels are able to exactly compensate the local spin,  $M = 2S_I$ , as illustrated in Fig. 4.5(b) for  $M = 2$  and  $S_I = 1$ .

Now, if the same two channels in Fig. 4.5(b),  $c_1$  and  $c_2$ , screen a spin- $3/2$  as in Fig. 4.5(c), an excess spin- $1/2$  is left over. This is an example of the undercompensated case,  $M < 2S_I$ . Part of the local moment is not screened, leaving excess degeneracy and thus entropy of  $k \ln(2S_I - M + 1)$ . For case Fig. 4.5(c), an extra spin- $1/2$  is unscreened with entropy  $k \ln(2)$ . Although the entropy does not tend to zero, if there are several excess local moments they can couple to each other and order ferromagnetically or antiferromagnetically to reduce the entropy to zero.

Finally, in case Fig. 4.5(d), excess spin now exists in the *conducting* channel,  $c_1$  and  $c_2$ . The magnetic moment is overcompensated by the screening channels. The amount

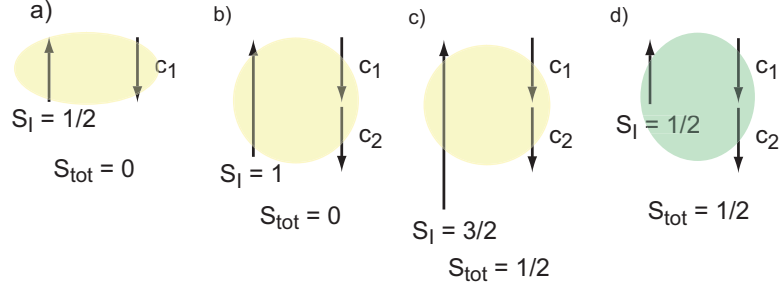


Figure 4.5: Four example cases of the multichannel Kondo effect. In the first, a local spin-1/2 ( $S_I = 1/2$ ) is coupled to a single channel ( $M = 1$ ). The local spin is completely screened by the channel, leaving  $S_{tot} = 0$  at low temperature. In (b), spin-1 is completely compensated by two conducting channels,  $c_1$  and  $c_2$ , and  $S_{tot} = 0$  as in (a). In (c) a spin-3/2 is left undercompensated by two channels, leaving a residual  $S_{tot} = 1/2$  from the local spin-1/2. In (d), a local spin-1/2 is overcompensated by two screening channels, leaving a residual  $S_{tot} = 1/2$  in the conduction channel.

of excess entropy is more complicated to calculate; the excess entropy for a spin-1/2 local moment screened by two channels Fig. 4.5(d) is a nonintuitive value  $k \ln(\sqrt{2})$ . Case Fig. 4.5(d) is known as the 2CK Kondo problem, and it does show non-Fermi liquid behavior at low temperature.

The Hamiltonian for 2CK can be written most simply as (from Eq. 4.3)

$$H_{int} = J_1 s_1(r) \cdot S + J_2 s_2(r) \cdot S, \quad (4.4)$$

which couples a single spin-1/2 local moment ( $S$ ) to two conducting channels,  $s_1(r)$  and  $s_2(r)$ . (For reference, the 1CK Hamiltonian is Eq. 3.1.) Although we have allowed the possibility for the two channels to be coupled asymmetrically to the local moment,  $J_1$  and  $J_2$ , for most of this section we will only consider the symmetric point  $J_1 = J_2$ .

There are many differences in thermodynamic quantities between compensated, Fig. 4.5(a), 1CK case and overcompensated (d) 2CK case. The spin susceptibility of the local moment for 1CK tends to zero at zero temperature as it is completely screened. In contrast, the spin susceptibility of the local moment in 2CK diverges

logarithmically as temperature reduces[37]. Similarly, the specific heat for 1CK tends to a constant value while the specific heat for 2CK again diverges logarithmically as temperature reduces.

Most importantly for this work, transport through a 2CK system differs dramatically from a 1CK system. For 1CK at zero temperature, an electron scattering off the impurity is completely described by single particle physics. At elevated temperatures, scattering of a 1CK impurity involves multiple particle hole pairs near the Fermi surface, however, they again have the expected  $T^2$  dependence of Fermi liquid theory[75]. In section 3.1, the transport consequences of 1CK was reviewed.

For 2CK, scattering near the Fermi surface is *nonexistent*[37]. Scattering is not single-particle-like nor can be composed of particle-hole pairs. Instead, there is scattering to a “different Hilbert space hidden in free field theory” described by Maldacena and Ludwig [96, 37]. The multiparticle scattered wave has a very specific cusp-like  $T^{1/2}$  temperature dependence. Recently, using conformal field theory Affleck and Ludwig have been able to provide a resistivity formula [31]:

$$\rho(T) = \frac{3n_i}{4\pi(e\nu v_F)^2} (1 + 4\sqrt{\pi T \lambda}) \quad (4.5)$$

where  $n_i$  is the number of impurities,  $v_F$  is the Fermi velocity, and  $\lambda$  is approximately the two channel Kondo temperature  $\lambda \approx T_{2CK}^{-0.5}$ .

Besides temperature dependence, the out of equilibrium properties also show interesting dependence. If transport through the system is dominated by one area containing some number of two channel Kondo impurities, applying a voltage bias greater than temperature will show the properties of 2CK out of equilibrium, as in Fig. 4.6. When the voltage bias is less than temperature, there is little effect of voltage on the conductance  $g \sim V^2$ . However, as voltage becomes large compared with temperature but still smaller than  $T_{2CK}$  ( $T < V_{ds} < T_{2CK}$ ), the conductance will also show square

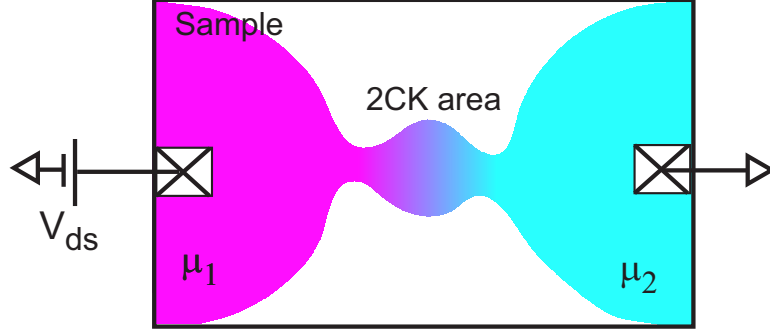


Figure 4.6: Probing the out of equilibrium properties of 2CK. If the main voltage drop occurs across the area with 2CK, the out of equilibrium properties can be probed.

root power law dependence,  $g \sim c\sqrt{V_{ds}}$ , where  $c$  is a constant.

The effect of finite voltage and finite temperature on conductance may be described by the scaling Ansatz [97]

$$g_i(V, T) = g_{i,0} + B_i T^\alpha \Gamma\left(\frac{A_i eV}{(kT)^{\alpha/\beta}}\right), \quad (4.6)$$

where  $i$  indexes the 2CK impurity,  $A_i$  and  $B_i$  are nonuniversal constants, and  $\alpha$  and  $\beta$  are exponents provided by theory. At low bias,  $g \propto \sqrt{T}$ , so  $\alpha = 0.5$ . In the case of 2CK,  $\alpha = \beta$  and the  $\Gamma(eV/kT)$  is a universal function with a specific limit at large bias,

$$\lim_{V \rightarrow \text{inf}} \Gamma\left(\frac{eV}{kT}\right) \rightarrow \left(\frac{eV}{kT}\right)^{0.5}. \quad (4.7)$$

The universal scaling function implies conductance traces at different bias and temperature collapse onto a single curve which is linear at high temperature when plotted as a function of  $(\frac{eV}{kT})^{0.5}$ , known as a scaling plot.

Non-Fermi liquid (2CK) physics (such as 2CK scaling and thermodynamic measurements) only occurs at the symmetric coupling point of Eq. 4.4,  $J_1 = J_2$ . If  $J_1 \neq J_2$ , the reservoir with the stronger coupling (larger  $J$ ) will solely screen the spin at low temperature, leading to 1CK effect with that reservoir as in Fig. 4.7(a). However, at

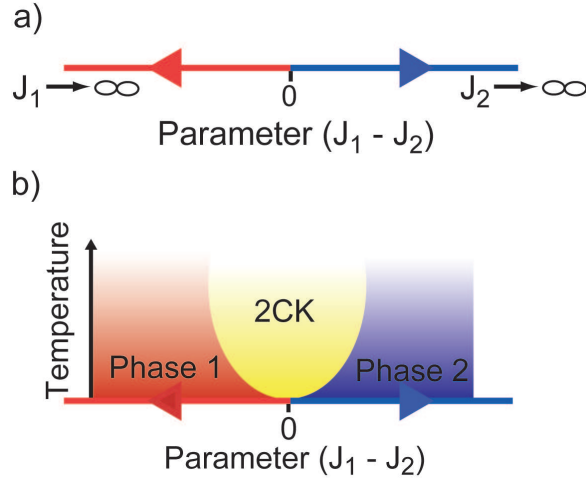


Figure 4.7: 2CK physics only occurs at symmetric coupling of the two channels,  $J_1 = J_2$ . Any asymmetry in the coupling of the two reservoirs leads to 1CK, as indicated by the flow diagram (a). At finite temperature (b), 2CK behavior can dominate material properties even when some asymmetry between the channels exists.

finite temperature, 2CK behavior can exist even with channel asymmetry, Fig. 4.7(b).

### 4.3 Previous Experimental Work into Two Channel Kondo

There are a few candidate systems in nature whose thermodynamic and transport properties are consistent with 2CK effect. So far, in this dissertation 2CK has been presented as a localized spin screened by two *independent* conducting channels. However, as mentioned in section 3.1, Kondo effect only requires a local degeneracy. To date, the local degeneracy of all proposed 2CK systems are not spin based. Instead, another local degeneracy is screened by conducting channels.

One possible realization of the 2CK system was discovered ten years ago in narrow copper constrictions, with the local degeneracy thought to be provided by atomic

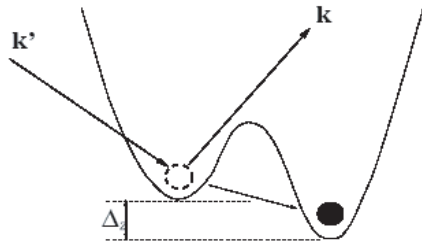


Figure 4.8: Potential profile of an atomic dislocation. The atom can sit in two different locations, providing the local degeneracy. The surrounding conduction electrons can then electrostatically screen the dislocation.

dislocations in the vicinity of the constriction [34, 35]. The local degeneracy is an atom in potential profile of Fig. 4.8 - the atom can sit on one of two sites. In the two-channel Kondo model, a local degeneracy is screened not by one but by two independent classes of conduction electrons, here distinguished by their spin (spin-up versus spin-down electrons form the two channels).

Thermodynamic measurements are not possible on a sample so small, however transport measurements reveal very striking behavior. 2CK scattering is expected to increase backscattering in this system, thus reducing conductance. In Fig. 4.9(a), voltage dependence shows very interesting cusp like behavior. In addition, the data scaled onto a single curve Fig. 4.9(b),

$$\frac{g(V, T) - g(0, T)}{T^\alpha} = F\left(\frac{eV}{kT}\right) \quad (4.8)$$

consistent with 2CK scaling of Eq. 4.6.

However, the measured electrical transport anomalies proved difficult to connect directly to theory, as each measurement was averaged over an estimated 50-100 independently-screened dislocations with different characteristic energy splittings. A vibrant controversy emerged over interpretation of the experiments [36], persisting to this day.

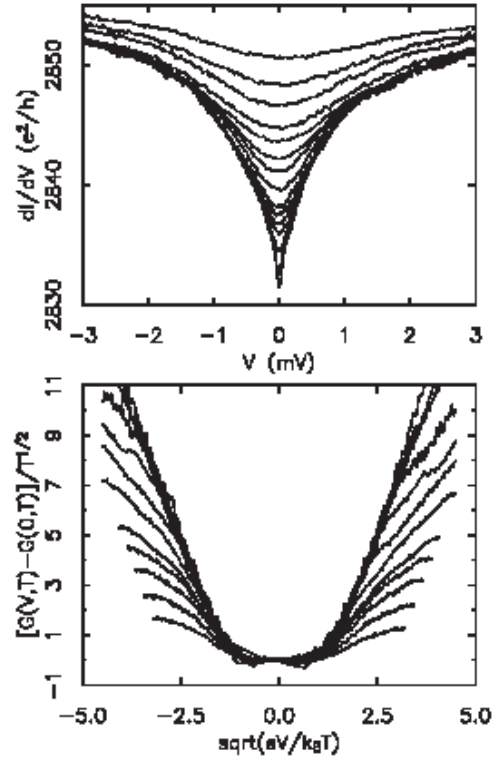


Figure 4.9: From Ralph et al.[97](a) Voltage dependence of differential conductance plotted for temperatures ranging from 100mK (bottom curve) to 5.7K (top curve). The same curves, rescaled according to Eq. 4.8 with  $\alpha = 1/2$  and plotted vs.  $(eV/kT)^{0.5}$ . The low temperature, the data collapse onto a single curve (linear for large  $(eV/kT)^{0.5}$ ).

Alloy/Compound	$T_K$	$C/T$	$\chi(T)$	$\rho(T)$	Single Ion?
$Y_{1-x}(Th_{1-y}, U_y)_xPd_3^{(*)}$	$\sim 40K$	$\ln T$	$1 - aT^{1/2}$	$1 - AT$	Yes
$Th_{1-x}U_xRu_2Si_2^{(*)}$	12K	$\ln T$	$\ln T$ ( $H \parallel c$ )	$1 + BT^{1/2}(?)$	Yes
$Th_{1-x}U_xPd_2Si_2^{(*)}$	12K	$\ln T$	$\ln T$ ( $H \parallel c$ )	$1 + BT^{1/2}(?)$	Yes
$La_{1-x}Ce_xCu_2Si_2^{(*)}$	$\sim 10K$	$\ln T$	$\ln T$	$1 - AT$	Approx.
$Th_{1-x}U_xM_2Al_3$	$\sim 20K$	$\ln T$	$\ln T(?)$	$1 - AT$	?
$Th_{1-x}U_xBe_{13}$	$\sim 10K$	$\ln T$	$1 - aT^{1/2}$	$1 + BT^{1/2}$ or $1 + AT$	Yes( $\chi(0)$ ) No( $C/T$ )
UBe <sub>13</sub>	10K	$\ln T$ at $H = 12T$	$1 - aT^{1/2}$	$1 + AT$	-
CeCu <sub>2</sub> Si <sub>2</sub>	10K	$\ln T$	?	$1 + AT$	-
PrInAg <sub>2</sub>	2K	const.	?	$AT?$	-

Figure 4.10: From [37]. Non-Fermi liquid heavy fermion alloys and compounds. This table lists the relevant properties of all non-Fermi liquid heavy fermion alloys and compounds for which a two-channel Kondo model description (in either dilute or concentrated limits) may be an appropriate starting place. The columns for specific heat, susceptibility, and resistivity indicate the low temperature behavior. All (but possibly  $CeCu_2Si_2$  and  $PrInAg_2$ ) have logarithmic in T specific heat coefficients over an extended temperature range. Those alloys marked with an asterisk show evidence for significant residual entropy at low temperatures.

Two-channel Kondo physics has also been used to explain specific heat anomalies in certain heavy fermion materials [33, 32, 98]: the unusual two-channel Kondo ground state has residual entropy even at zero temperature. Fig. 4.10 from [37] describes the thermodynamic and transport phenomenon in these compounds. However, out of equilibrium measurements are not possible due to the bulk nature of the samples. Distinctively, in all these compounds spin serves as a degeneracy for mobile rather than local electrons.

# Chapter 5

## Implementation of Two Channel Kondo Effect in Semiconductor Nanostructures

Recently the two-channel Kondo system has attracted new interest because of proposals to implement it in a modified quantum dot system [23, 25]. In this chapter, we describe the theory behind our experimental effort to create a single two-channel Kondo system, whose study may both advance many-body theory and help explain behavior of other candidate realizations of two-channel Kondo.

### 5.1 Proposal

The first proposal for 2CK in semiconductor nanostructures was made by Matveev in 1991 [99, 100]. The proposal was very simple, couple a large but finite reservoir to a (infinite) Fermi reservoir, as in Fig. 5.1(a). At the charge degeneracy points, having no excess electrons and one excess electron in the box is degenerate. This two-

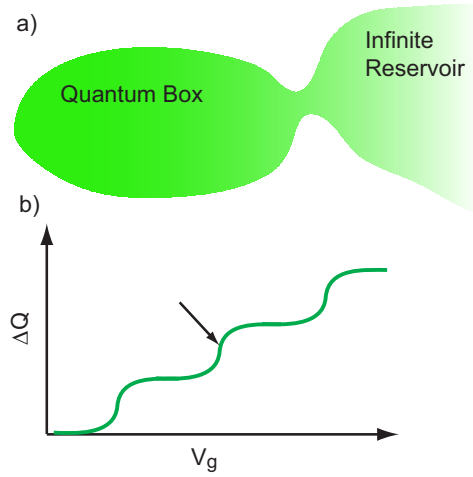


Figure 5.1: Drawing of Matveev's original proposal for 2CK behavior in nanostructures. A finite reservoir (quantum box) is coupled to an infinite Fermi reservoir. 2CK behavior was predicted to govern the behavior of the charge steps (charge degeneracy points of the finite reservoir), marked by the arrow.

fold *charge* degeneracy is then screened by the conduction electrons, with spin-up and spin-down conduction electrons forming the two independent screening channels. The 2CK behavior manifests as an extra smearing in the charge steps as in Fig. 5.1(b). A local capacitance measurement was proposed to measure the effect. Unfortunately, the quantum energy level spacing,  $\Delta$  was constrained to be less than temperature in the model, meaning the quantum box must be large. Simultaneously, the 2CK temperature is determined by the charging energy of the box - restricting the box from being too large. Zarand [101] later argued these two conflicting constraints could not be simultaneously realized in a semiconductor quantum dot.

Instead, we follow a recent proposal by Oreg and Goldhaber-Gordon [23] to implement a spin-based 2CK system in nanostructures. The two *independent* reservoirs are physically separate electron baths coupled to a local artificial magnetic impurity. The magnetic moment is a small quantum dot tuned to contain an odd number of electrons,

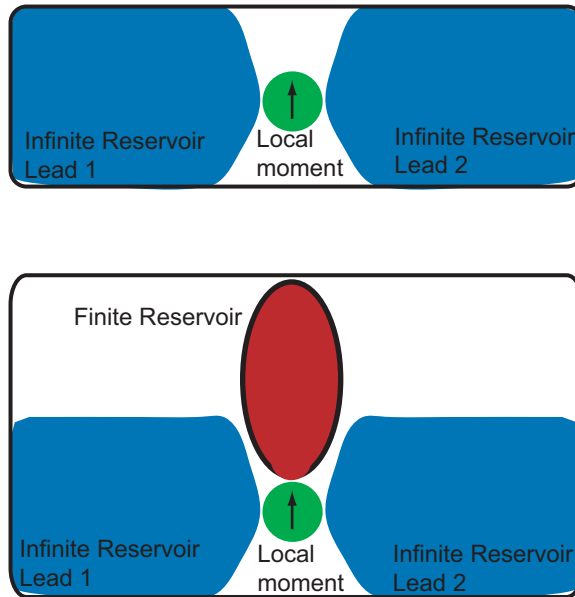


Figure 5.2: In (a), a quantum dot (green) with an odd number of electrons (excess spin  $S = 1/2$ ) is coupled to two electrical leads (blue). The two infinite reservoirs cooperate to form a 1CK effect to screen the spin. In (b), a quantum dot with  $S = 1/2$  is coupled to two electrical leads or infinite reservoirs (blue) and one finite reservoir (red). The finite reservoir also attempts to screen the excess spin-1/2, forming an independent 1CK effect (see text). The two independent channels (finite reservoir and infinite reservoirs) can be tuned to be equally coupled to the spin-1/2, forming a 2CK effect.

as in section 3.3. The spin-1/2 moment then forms the localized degeneracy for the surrounding electrons to screen.

The local moment is coupled to two electrical leads, as in Fig. 5.2(a), which are called the infinite reservoirs. The infinite reservoirs cooperate in screening the excess  $S = 1/2$  on the quantum dot, forming a 1CK effect as discussed in section 3.3. In addition, in Fig.5.2(b), a finite reservoir is coupled to the quantum dot.

Making one reservoir finite has two important consequences; the finite reservoir can be effectively represented as a quantum dot with the a quantum energy level spectrum and a charging energy (see Fig. 2.3).

At low temperature, the charging energy can forbid charge transfer to or from the

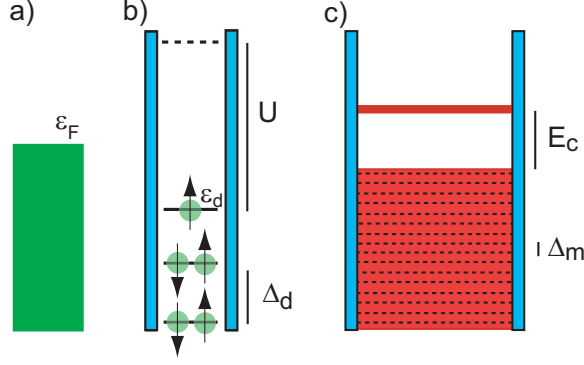


Figure 5.3: The three components of Eq. 5.1. (a) The infinite reservoir is shown filled up to a Fermi level  $\epsilon_F$ . In (b) a small quantum dot with an unpaired electron acts like a magnetic impurity. For this experiment, we do not have a single electron quantum dot, hence the quantum energy level spectrum  $\Delta_d$  is also shown. In (c) the finite reservoir is represented by a quantum dot with charging energy  $E_c$ . The energy level spectrum,  $\Delta_m$ , will not be resolved because  $\Delta_m < kT$ . Hence, the finite reservoir effectively has a continuous density of states (like (a)) with a charging energy.

finite reservoir (Coulomb blockade). The situation we will concentrate on now is for stable number of electrons remaining on the finite reservoir. The model Hamiltonian to describe the (noninteracting) system in Fig. 5.2(b) is

$$H = \sum_{k\sigma} \epsilon_{k\sigma} \alpha_{k\sigma}^\dagger \alpha_{k\sigma} + \sum_{k\sigma} \epsilon_{k\sigma} m_{k\sigma}^\dagger m_{k\sigma} + \sum_{\sigma} \epsilon_d^0 d_{\sigma}^\dagger d_{\sigma} + U n_{d\uparrow} n_{d\downarrow} + E_c (n_m - N_m)^2 \quad (5.1)$$

where the quantum dot,  $d$ , contains a singly occupied spin degenerate (good approximation for a small quantum dot ( $\Delta \gg kT$ ) with odd number of electrons), with interaction energy  $U$  and quantum confinement energy  $\epsilon_d^0$ . The finite reservoir,  $m$ , has a charging energy  $E_c$  and quantum confinement energy  $\epsilon_{k\sigma}$ . Parameter  $N_m$  sets the occupation of the finite reservoir, and can be tuned by nearby gate electrodes. The  $\alpha$  term is simply the result of rotation of the two infinite leads into a single infinite reservoir provided by Glazman and Raikh [76] and mentioned in section 3.3. These various terms are pictorially represented in Fig. 5.3.

With this Hamiltonian, it is energetically unfavorable for an excess electron to exist

on the finite reservoir. At low temperature, processes in which charge transfers from the finite reservoir to the infinite reservoir are forbidden. However, spin flips in which an electron temporarily leaves the finite reservoir into the small quantum dot (magnetic impurity) and back remain possible at low temperature. This is a fundamental criterion for the finite reservoir to become an independent screening channel. The finite reservoir and infinite reservoir screen the magnetic impurity through interaction terms [23]

$$H_{int} = \sum_{k\sigma} \left( V_m^* m_{k\sigma}^\dagger d_\sigma + H.c. \right) + \sum_{k\sigma} \left( V_\alpha^* \alpha_{k\sigma}^\dagger d_\sigma + H.c. \right) \quad (5.2)$$

where the first term allows spin flips between the magnetic impurity and finite reservoir and the second term allows spin flip events between the magnetic impurity and the infinite reservoir. There are no terms of this order which exchange electrons between the finite reservoir and the infinite reservoir (electrons which screen the magnetic impurity must return from the reservoir they originated in). According to [23, 24] this fills the requirements needed for an independent reservoir.

The finite size causes the finite reservoir to have a discrete energy level spectrum ( $\Delta_m$ ) in addition to a charging energy. However, Kondo screening we described in section 3 involves interaction of a single spin degenerate state with a continuous density of states filled to some Fermi level,  $\epsilon_F$ . We can make the discrete energy level spectrum of the large dot seem continuous by making the average energy level spacing less than temperature  $\Delta_m < kT$ . These constraints restrict the size of the finite reservoir and temperature range we can operate over. In the next section, we discuss the implementation of this into semiconductor nanostructures.

It is important to note the limit  $\Delta_m < kT$  for the finite reservoir is not universally agreed upon in the community. A less rigid constraint,  $\Delta_m < kT_K$  (single particle level spectrum less than Kondo temperature), has also been proposed to follow 2CK behavior. Since we require  $T_K > T$ , and in most cases  $T_K \geq 10T$ , the finite reservoir can

be made smaller or the temperature can be made lower and 2CK behavior will persist. At the limit of  $T_K < \Delta_m$ , other interesting effects may occur, such as the Kondo box problem where a localized magnetic moment interacts with a discrete energy level spectrum. We are far from this limit, so we do not consider those effects in our current experimental efforts.

Also, if the finite box is kept the same size ( $\Delta < kT$ ) however Coulomb blockade is relaxed (say by tuning a nearby gate electrode), the system looks like the Matveev proposal [99, 100], mentioned above. Relaxing CB means the  $N$  and  $N+1$  occupancies of the large dot become degenerate. This charge degeneracy can be screened by the conduction electrons (spin up and spin down forming the two channels), similar to the charge 2CK effect mentioned in section 4.3. However, the main difference from the Matveev proposal is now the conduction electrons must interact through the small quantum dot. If one considers the small dot as just a single level with some broadening, a stable 2CK fixed point has been shown to exist [102], which we call a charge 2CK fixed point. In fact, in recent numerical renormalization group calculations, the spin 2CK fixed point of Oreg and Goldhaber-Gordon's system [23] has been also been found and has been shown to evolve continuously (as a function of gate voltage - explained in next section) into the charge 2CK [103, 104].

## 5.2 Implementation

In order for a large quantum dot to be universally considered a finite reservoir for 1CK and 2CK effects, the constraints  $E_c > kT$  (stable charge) and  $\Delta_m < kT$  (effectively continuous density of states) should be met. However, as shown in Fig. 5.4, stable charge in a Coulomb blockade (CB) valley is nontrivial to define. For simplicity, we

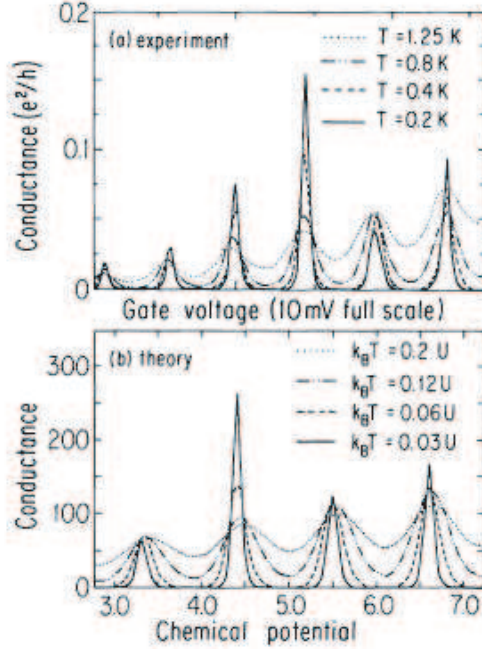


Figure 5.4: From [105]. Conductance of Coulomb blockade (CB) peaks as a function of temperature. When  $kT < E_c/10$ , there is negligible conductance in the CB valley, meaning a stable number of electrons resides in the dot.

choose to define stable charge on the finite reservoir when  $E_c > 10kT$ . As mentioned in section 2, the charging energy  $E_c = e^2/2C$  can be modeled by the self capacitance of a 2D disc,  $C \sim r$ , where  $r$  is the radius of the dot (or likewise  $\sqrt{A}$ , where  $A$  is the area of the dot). Thus, a smaller finite reservoir is preferred.

The quantum energy level spacing also increases as the area of the device reduces. The constraint  $\Delta_m < kT$  can be simultaneously met because quantum energy level spacing reduces faster than the charging energy,  $\Delta_m \sim 1/A$ , whereas  $E_c \sim 1/\sqrt{A}$ , as the device size increases. (The quantum energy level spectrum can be most easily modeled by a particle in a 2D box.)

Both  $E_c$  and  $\Delta_m$  are shown as a function of device area in Fig. 5.5. To ensure the model are reasonably accurate, data on charging energy and level spacing for a few

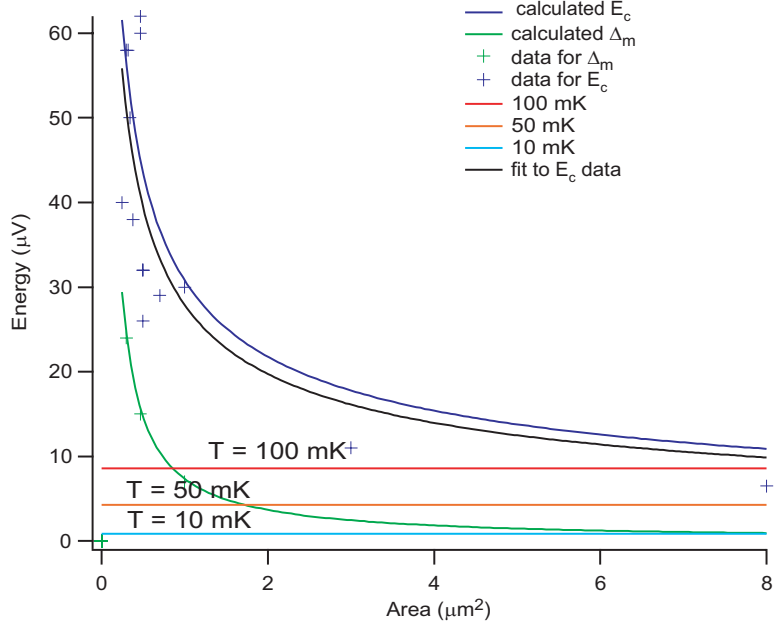


Figure 5.5: Charging energy ( $E_c$ ) and the single particle level spacing  $\Delta_m$  as a function of area  $A$  of the finite reservoir. The relevant scale for charging energy is  $E_c/10$  (see text). The solid blue curve is calculated charging energy using the self capacitance of a metal disc. The blue markers are experimental values from various papers [39, 106]. The solid black curve is a  $1/\sqrt{A}$  fit to the data points (best fit). The green curve is the  $\Delta_m$  based on calculation for spin degenerate energy levels - a reasonable approximation for these quantum dots. Energy of various temperatures are also shown. The necessary energy scale is  $E_c/10 > kT > \Delta_m$ .

different quantum dots of various size is also plotted. Several different device areas fulfill the restrictions for the finite reservoir for our experimental temperature range (dilution refrigerator has a temperature range from  $\sim 10mK$  to  $1K$ ).

We also would like the largest temperature range over which to observe 2CK effect. As discussed in section 4.2,  $g \sim \sqrt{T}$  temperature dependance of the conductance is one hallmark feature of 2CK. For a few different device sizes, the ratio of  $E_c/10kT$  and  $\Delta_m/kT$  based on the results from Fig. 5.5 are shown as a function of temperature in Fig. 5.6. For a device area of  $3\mu m^2$ , the constraint  $E_c/10kT > 1 > \Delta_m/kT$  is met from

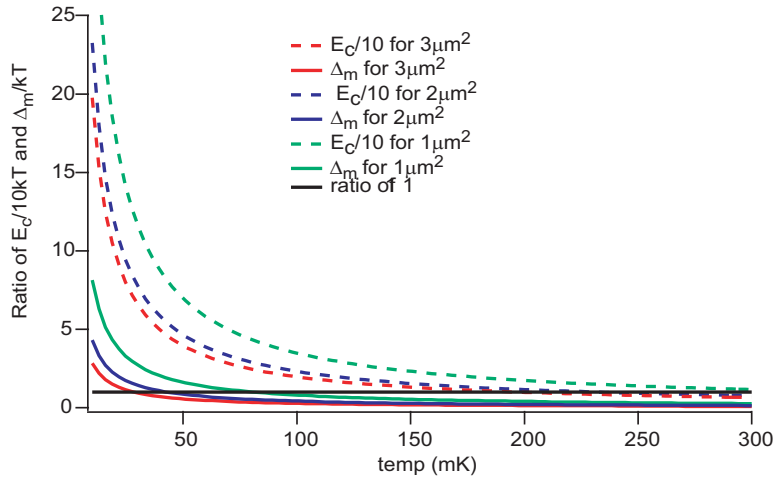


Figure 5.6: Ratio of charging energy to temperature ( $E_c/10kT$ ) and single particle level spacing to temperature ( $\Delta_m/kT$ ) for three different device area (1, 2 and 3  $\mu m^2$ ). When  $E_c/10kT > 1$ , there will be a well defined number of electrons on the quantum dot. When  $\Delta_m/kT < 1$ , the single particle level spectrum will not be resolvable.

$\sim 20mK$  to  $200mK$ , over one order of magnitude of temperature.

Based on these plots, we chose to fabricate two different area finite reservoirs,  $1.5\mu m^2$  and  $3\mu m^2$ . Scanning electron microscope images of the two different finite reservoir areas are shown in Fig. 5.7. In both Fig. 5.7(a) and (b), the finite reservoir is coupled to a small quantum dot. The small quantum dot acts like a magnetic impurity - the spin-1/2 degeneracy required for 1CK and 2CK.

In order to observe 1CK, temperature must be lower than  $T_K$ , which in the Anderson model is given by

$$T_{1CK} \sim e^{\pi\epsilon_0(\epsilon_0+U)/\Gamma U}, \quad (5.3)$$

from Fig. 5.3(b) (note  $\epsilon_0$  is always negative).  $T_K$  rises dramatically when  $\epsilon_0$  is near zero or  $-U$ . However, Kondo effect breaks down in these limits and crosses over to the mixed valence regime [77]. Note also the exponential dependence of  $T_K$  on  $\Gamma$ , the coupling between the reservoir and the localized moment. Although the device size has

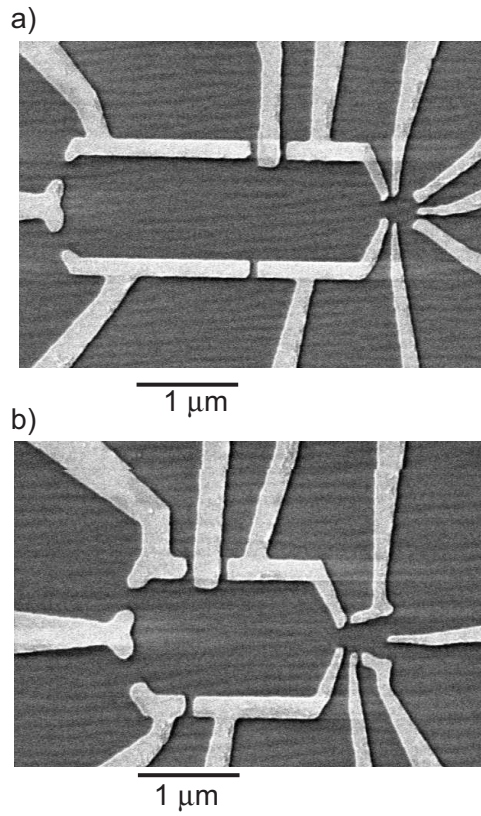


Figure 5.7: In (a), a  $3\mu\text{m}^2$  finite reservoir is fabricated. In (b), a  $1.5\mu\text{m}^2$  finite reservoir is fabricated. Each finite reservoir is coupled to a small quantum dot which serves as the magnetic impurity.

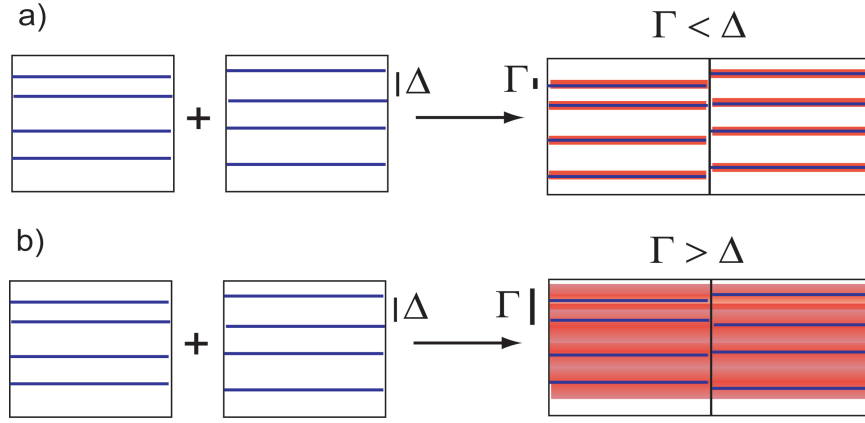


Figure 5.8: In both (a) and (b), two pieces of metal have a random distribution of energy levels due to confinement. When the pieces in (a) are connected seamlessly together, they remain two separate pieces of metal because the coupling  $\Gamma$  is less than  $\Delta$ , the mean level spacing of the individual grains. In contrast, when the metal grains in (b) are connected together,  $\Gamma > \Delta$  so they form a single fully hybridized grain.

no direct relation on  $\Gamma$ , this is the parameter in *GaAs* quantum dots which will make the largest difference in  $T_K$ .

Borrowing an argument from Thouless [107], we can show a relation between  $\Gamma$  and  $\Delta_d$  which must be maintained. Begin with two (disordered) metal grains at zero temperature. They will each have some random energy level spectrum, as shown in Fig. 5.8. The two metal grains can then be brought into contact with each other to form a single metal island. Whether the two islands remain independent or fully hybridize into a single island depends on the ratio  $\Gamma/\Delta$ .

Thouless showed that when  $\Gamma/\Delta < 1$ , the two islands will remain distinct from each other, as in (a). This is analogous to a quantum dot. The energy levels in a quantum dot will have some broadening due to the coupling to the outside world (the Fermi reservoirs in this case). If the coupling,  $\Gamma$  is less than the particle level spacing, the quantum dot will remain distinct from its leads, forming localized states needed

for Kondo effect.

If  $\Gamma/\Delta > 1$  then the islands of Fig. 5.8 hybridize together to form a single metallic region. The same should be true of a quantum dot - if the coupling to the Fermi reservoirs is greater than the single particle level spacing, there will be *delocalized* states and the quantum dot will not be distinct from the leads. Electrons will flow freely in and out of the island, and thus will not facilitate the Kondo effect.

Since  $\Gamma < \Delta$ , we are forced to make the artificial magnetic impurity small so  $\Gamma$  can be made as large as possible. In the case of the quantum dot in Fig. 5.7, the small quantum dot has a single particle level spacing of  $\Delta_d = 100\mu eV$ . We may quickly estimate a reasonable upper limit on Kondo temperature by using  $\Gamma \sim \Delta_d/2 = 50\mu eV$  and  $T_K \sim \Gamma/2 = 25\mu eV$ , meaning  $T_K$  as high as  $300mK$  may be attainable in this device. Design limitations such as the need for three leads to the small quantum dot did not allow the small the quantum dot to be fabricated as some other lateral *GaAs* quantum dots with higher  $T_K$  [28, 64].

The two screening channels are then shown in Fig. 5.9(a), the finite reservoir in red and the source and drain reservoirs in blue. The small quantum dot and large quantum dot each can have a stable number of electrons. The charge of both dots can then be described by a charge stability hexagon, shown in Fig. 5.9(b), as a function of two capacitively coupled gate voltages  $sp$  and  $bp$ . These gate voltages tune the occupancy of each dot. For 2CK, an odd number of electrons must be confined to the small quantum dot so it is an artificial magnetic impurity. The charge of the large dot must just be stable (in a CB valley).

Once this condition is met, tuning to the 2CK point is possible. The finite reservoir will have coupling  $J_m = J_{f.r.}$  and the infinite reservoirs will have coupling  $J_{i.r.}$ . Both antiferromagnetic coupling  $J_{i.r.}$  and  $J_{f.r.}$  can be controlled independently by tuning

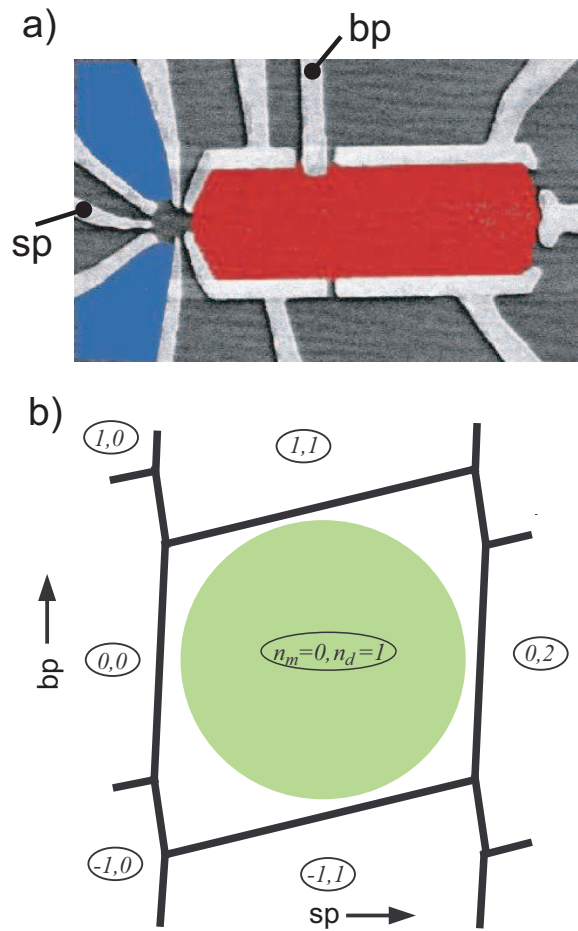


Figure 5.9: Double quantum dot system. (a) The small quantum dot is the artificial magnetic impurity when it confines an odd number of electrons,  $n_d = 1$ . The two screening reservoirs are the finite reservoir (large quantum dot, red) and the infinite reservoirs (source and drain leads, blue). A charge stability diagram can be drawn for the double quantum dot system (b). In the green region, the small quantum dot contains an odd number of electrons ( $n_d = 1$ ) and the finite reservoir contains a fixed number of electrons ( $n_m = \text{integer}$ ) - the necessary conditions for 2CK.

the tunnel rate to the reservoir and the depth of the impurity level with respect that reservoir's Fermi level, as shown in Fig. 5.10.  $J_{i.r.}$  depends on these parameters [23],

$$J_{i.r.} = \Gamma_{i.r.} \left( \frac{1}{E_2^0 - E_1^0} + \frac{1}{E_0^0 - E_1^0} \right) \quad (5.4)$$

where  $E_1^0$  corresponds to a single electron occupying the localized site and no excess electrons in the finite reservoir, and the other parameters are defined in Fig. 5.10(a).

The coupling with the finite reservoir  $J_{f.r.}$  can be described in similar terms, [23],

$$J_{f.r.} = \Gamma_{f.r.} \left( \frac{1}{E_0^1 - E_1^0} + \frac{1}{E_2^{-1} - E_1^0} \right) \quad (5.5)$$

where now the energy terms involve temporarily adding an electron to the finite reservoir ( $E_0^1$ ) or temporarily removing an electron ( $E_2^{-1}$ ) to form the Kondo bond.

In this system, we have control all parameters in Eq. 5.4 and 5.5 by applying appropriate gate voltages. The points of  $J_{i.r.} = J_{f.r.}$  can be filled into a charge stability diagram, as was accomplished by Oreg and Goldhaber-Gordon in Fig. 5.11[23]. Here, they fixed each tunnel rate  $\Gamma_{i.r.}$  and  $\Gamma_{f.r.}$  and thus the ratio  $\gamma = \Gamma_{f.r.}/\Gamma_{i.r.}$ . A combination of  $sp$  and  $bp$  can then vary all energies  $E_x^y$  from Eq. 5.4 and 5.5 (these energies can be controlled very precisely). A single charge stability hexagon can then be divided into three different phases (three distinct low temperature fixed points). Below we discuss the  $\gamma = 1.08$  phase diagram, however many ratios of  $\gamma$  produce the 2CK effect - we do not need to be able to tune the  $\Gamma_{f.r.}$  and  $\Gamma_{i.r.}$  precisely.

A pair of curves is produced where  $J_{i.r.} = J_{f.r.}$  and the 2CK effect is realized in Fig. 5.11. When probing transport through the small quantum dot, the conductance is expected to have a characteristic  $\sqrt{E}$  behavior

$$g(T, V_{ds}) \sim g_{2CK}(0, 0) - \sqrt{\max(V_{ds}, T)}. \quad (5.6)$$

Deviation from this curve will cause an asymmetry between the two channels, breaking the 2CK effect. In the shaded regions,  $J_{f.r.} > J_{i.r.}$ , meaning a 1CK effect with the

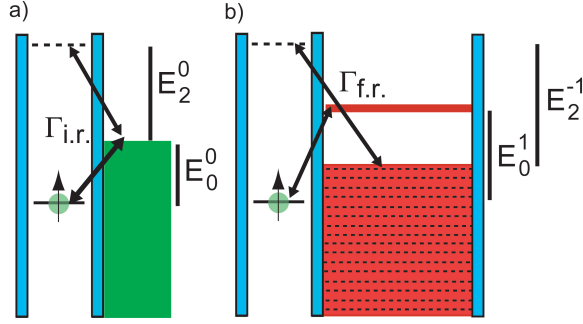


Figure 5.10: Parameters of  $J_{i.r.}$  and  $J_{f.r.}$ . In (a), tunnel rate  $\Gamma_{i.r.}$  represents the processes which involve spin flip events between the localized electron and the infinite Fermi reservoir. Kondo screening involves two processes: the electron process involve energy difference  $\Delta E_1 = E_0^0 - E_1^0$ , and the hole process is  $\Delta E_2 = E_2^0 - E_1^0$ . The subscript represents the number of electrons in the localized site and the superscript represents the number of excess electrons in the finite reservoir. For simplicity in describing the energy scales in this figure, the energy of noninteracting ground state is set equal to zero,  $E_1^0 = 0$ , so  $\Delta E_1 = E_0^0$  and  $\Delta E_2 = E_2^0$ . In (b), the parameters of  $J_{f.r.}$  are shown.  $\Gamma_{f.r.}$  represents the tunnel rate for the localized electron leaving the state and entering the finite reservoir and the corresponding hole process. Again taking  $E_1^0 = 0$ , the energy difference for the electron process is  $E_0^1$  and the hole process is  $E_2^{-1}$ .

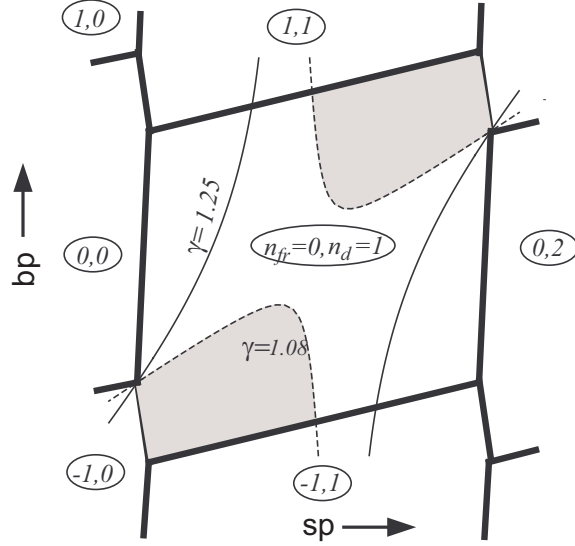


Figure 5.11: Calculation and figure from [23]. The same charge stability diagram as a function of  $bp$  and  $sp$  as shown in Fig. 5.9. The superimposed curves are '2CK lines' - curves in the charge stability diagram where  $J_{i.r.} = J_{f.r.}$ . These curves are formed by setting  $\Gamma_{f.r.}$  and  $\Gamma_{i.r.}$ , which then form the ratio  $\gamma = \Gamma_{f.r.}/\Gamma_{i.r.}$ . Then vary  $E_x^y$  from equation 5.4 and 5.5 with gates  $bp$  and  $sp$  for  $J_{i.r.} = J_{f.r.}$ . Curves of 2CK effect are shown for two different  $\gamma$ . In addition, on either side of the curve, a different quantum phase exists. For example, setting  $\gamma = 1.08$ , in either shaded region  $J_{f.r.} < J_{i.r.}$ , meaning a 1CK state will form with the finite reservoir. In contrast, in all unshaded regions the infinite reservoir has greater coupling and a 1CK Kondo state will form with that reservoir.

finite reservoir will be formed. A 1CK effect between the finite reservoir and the small quantum dot manifests itself as a suppression of conductance as temperature reduces,

$$g(T, V_{ds}) \sim [\max(V_{ds}, T)]^2 \quad (5.7)$$

Finally, in the unshaded region  $J_{i.r.} > J_{f.r.}$ , so a normal 1CK effect occurs with the small quantum dot with the expected temperature and bias dependence,

$$g(T, V_{ds}) \sim g_{1CK}(0, 0) - [\max(V_{ds}, T)]^2. \quad (5.8)$$

Increasing  $\gamma$  increases the area where  $J_{f.r.} > J_{i.r.}$  (finite reservoir wins), as shown in Fig. 5.11 for  $\gamma = 1.25$ . Likewise, reducing  $\gamma$  causes an increase in the area where the leads win, as expected. When ( $\gamma \ll 1$ ) or ( $\gamma \gg 1$ ), the whole charge stability diagram will exist in one phase or the other.

At finite temperature the relation  $J_{i.r.} = J_{f.r.}$  does not need to strictly hold for 2CK physics to be present. As shown in Fig. 5.12, finite detuning of the couplings to the finite and infinite reservoirs,  $\Delta J = J_{i.r.} - J_{f.r.}$ , will still yield 2CK effect in the device.

Also shown in Fig. 5.12 is the dependence of the conductance on  $\Delta J$ . The detuning can be changed by either gate voltage  $bp$  or  $sp$  in Fig. 5.11 to cross one of the 2CK lines. The expected conductance is then plotted in Fig. 5.12 as  $\Delta J$  moves from positive to negative.  $\Delta_T$  represents the detuning over which 2CK behavior will occur at finite temperature, derived from Fig. 5.12(left). At finite temperature, 1CK with the leads will occur when  $\Delta J > \Delta_T$  and conductance will follow equation 5.8, enhanced conductance at low temperature. Likewise, when  $\Delta J < -\Delta_T$ , 1CK with the finite reservoir will occur and conductance will be suppressed at low temperature as equation 5.7.

In the intermediate regime  $\Delta J < \Delta_T$ , 2CK physics following equation 5.6 will be present. In this regime, the conductance at low temperature and bias ( $eV_{ds}, T \ll$

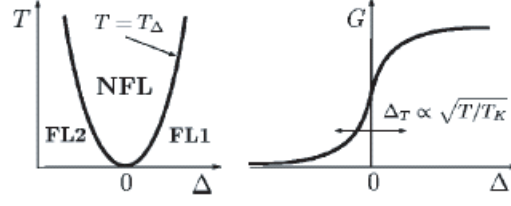


Figure 5.12: From [24] Effects of finite  $\Delta J = J_{i.r.} - J_{f.r.}$  and temperature. On the left, a phase diagram for the 2CK system is shown as a function of  $\Delta J$  and temperature. At finite temperature, finite  $\Delta J$  will still exhibit non-Fermi liquid behavior.  $T_\Delta$  is the energy scale over which 2CK behavior will dominate when  $\Delta J$  is finite. The transition across the phase diagram (tuning  $\Delta J$  from large positive to large negative) is shown on the right. The high conductance corresponds to the leads winning ( $\Delta_J > \Delta_T$ ) and the low conductance region corresponds to ( $\Delta_J < -\Delta_T$ ), the finite reservoir winning. This transition is predicted to broaden with temperature as  $\Delta_T \sim \sqrt{T/T_K}$ .

$T_{2CK}$ ) is further expected to follow the 2CK scaling form [31, 24]

$$\frac{1}{g_{1CK}(0,0)} \frac{dI}{dV} = \frac{1}{2} \left( 1 - \sqrt{\frac{\pi T}{T_{2CK}}} F_{2CK} \left( \frac{|eV|}{kT} \right) \right) \quad (5.9)$$

From this equation,  $g_{2CK}$  from equation 5.6 can be easily derived,  $g_{2CK} = \frac{1}{2} g_{1CK}(0,0)$ .

Furthermore, the function  $F_{2CK}(x)$  is a universal function with limits

$$F_{2CK}(x) = \begin{cases} 1 + cx^2 & x \ll 1 \\ \frac{3}{\sqrt{\pi}} \sqrt{x} & x \gg 1 \end{cases} \quad (5.10)$$

where  $c$  is a numerical constant near 1.  $T_{2CK}$  is not a well defined parameter in the literature. However, in this system,

$$T_{2CK} = \frac{1}{2 \log(E_c/T_K)} \frac{T_{1CK}^2}{E_c} \quad (5.11)$$

meaning a larger finite reservoir, smaller  $E_c$ , is preferable [108, 109]. With this background, we next report the creation of a 2CK effect in semiconductor nanostructures.

# Chapter 6

## Two-Channel Kondo Effect and Quantum Phase Transitions

### 6.1 Observation of the Two-Channel Kondo Effect

Some of the most intriguing problems in solid state physics arise when the motion of one electron dramatically affects the motion of surrounding electrons. Traditionally, such highly-correlated electron systems have been studied mainly in materials with complex transition metal chemistry. Over the past decade, researchers have learned to confine one or a few electrons within a nanoscale semiconductor “artificial atom”, and to understand and control this simple system in exquisite detail. In this Article, we combine such individually well-understood components to create a novel highly-correlated electron system within a nano-engineered semiconductor structure. We tune the system *in situ* through a quantum phase transition between two distinct states, one familiar and one subtly new. The boundary between these states is a quantum critical point: the exotic and previously

**elusive two-channel Kondo state, in which electrons in two reservoirs are entangled through their interaction with a single localized spin.**

The Kondo effect has become a hallmark of coherent electron transport in a variety of nanostructures ranging from lithographically-defined semiconductors [28] to carbon nanotubes [65] and molecules [66, 67]. Kondo first introduced the phenomenological Hamiltonian [3]

$$H_K = J\vec{s} \cdot \vec{S} + H_{\text{reservoir}} \quad (6.1)$$

to describe a magnetic impurity embedded in a host sea of electrons. A localized spin  $\vec{S}$  couples antiferromagnetically with strength  $J$  to spins  $\vec{s}$  of electrons in the surrounding reservoir.  $H_{\text{reservoir}}$  represents the free electrons in the reservoir. At temperatures below the Kondo temperature  $T_K$ , electrons in the reservoir screen the localized spin. The Kondo Hamiltonian was later found to be derivable from the more microscopic Anderson model, which consists of an electron bound to an impurity site in a metal host (Fig. 6.1(a)). Here, Kondo's antiferromagnetic coupling emerges from tunneling on and off the local site.

Many systems of strongly-interacting particles can be understood in the framework of Landau's Fermi liquid theory, whose basic entities, termed quasiparticles, roll most effects of interactions into changes in particle properties such as mass and energy. Although the Kondo ground state is complex, its excitations can still be described as weakly-interacting quasiparticles. Some of the most intriguing problems in solid state physics arise when this simplification cannot be applied. Examples of such highly-correlated systems include Luttinger liquids, fractional quantum Hall Laughlin liquids, high-temperature superconductors, and the two-channel Kondo system, a novel state studied experimentally in this Article.

In the two-channel Kondo (2CK) model, introduced 25 years ago by Nozières and

Blandin, and independently by Zawadowski [29, 95], a localized spin  $\vec{S}$  is antiferromagnetically coupled to two independent reservoirs of electrons according to the Hamiltonian

$$H_{2CK} = J_1 \vec{s}_1 \cdot \vec{S} + J_2 \vec{s}_2 \cdot \vec{S} + H_{\text{reservoirs}}. \quad (6.2)$$

The symmetric 2CK state is formed when the two independent channels (or reservoirs) are equally coupled to the magnetic impurity, i.e.  $J_1 = J_2$ . Each reservoir individually attempts to screen the local spin. Since they cannot both screen the spin, this is an unstable situation, resulting in a new ground state in which the local spin is only partially screened. Unlike for single-channel Kondo (1CK), in the 2CK state the quasiparticle concept of Fermi liquid theory does not apply: the decay rate for a low energy excitation ( $\sim \sqrt{\epsilon}$ ) is greater than the energy  $\epsilon$  of the excitation itself. Stable low-lying excitations must thus be collective [31, 37].

Any difference in channel coupling will force the system away from the non-Fermi liquid 2CK state and toward the 1CK state associated with the more strongly-coupled reservoir. Although the symmetric 2CK state might therefore seem difficult to access, it has been invoked to explain remarkable low-energy properties of some heavy Fermion materials [33, 32, 98], and glassy metals [34, 35, 110]. However, the connections of these experimental observations to 2CK theory remain problematic [111], in part because the microscopic electronic structure of the various materials is unclear.

In this paper, we present experimental results on an artificial impurity which is designed to display 2CK. Crucially, we can precisely control the coupling constants  $J_1$  and  $J_2$ , while maintaining the independence of the two channels. The system is built from a *GaAs/AlGaAs* heterostructure containing a low density ( $n_e = 2 \times 10^{11} e^-/cm^2$ ), high mobility ( $\mu = 2 \times 10^6 cm^2/Vs$ ) two-dimensional electron gas (2DEG) 68 nm below the surface. We follow the proposal by Oreg and Goldhaber-Gordon [23] to

produce two independent screening channels for an artificial magnetic impurity. A small gate-defined quantum dot (containing  $\sim 25$  electrons) with bare charging energy  $U \approx 1 \text{ meV}$  and average quantum energy level spacing  $\Delta \approx 100 \mu\text{eV}$  plays the role of our magnetic impurity (Fig. 6.1(d), left). Previous experiments which claim to probe 2CK [34, 35, 33, 32, 98] used a local orbital degeneracy in place of spin, freeing spin of the surrounding conduction electrons to act as the channel index. In contrast, our local degeneracy is a real spin, and we use two physically-separated reservoirs (red and blue in Fig. 6.1(d)) for the screening channels. Two leads of the small quantum dot cooperate as a single screening channel with antiferromagnetic coupling  $J_{\text{ir}}$  (“infinite reservoir”) [76]. An additional lead is made finite in size (red, Fig. 6.1(d)), so that adding or removing an electron from this reservoir is energetically forbidden at low temperature, a phenomenon known as Coulomb blockade. The area of the finite reservoir is  $\sim 3 \mu\text{m}^2$ , corresponding to a charging energy  $E_c = 100 \mu\text{eV} \approx 1 \text{ K}$ . At the base electron temperature of our dilution refrigerator – 12 mK, as determined by Coulomb blockade thermometry on the small quantum dot – we cannot resolve the quantized level spectrum of the finite reservoir. Hence, the finite reservoir has an effectively continuous density of states and can screen the magnetic impurity. Since Coulomb blockade prevents exchange of electrons with the other leads, the finite reservoir acts as a second Kondo screening channel (Fig. 6.1(e)), with antiferromagnetic coupling  $J_{\text{fr}}$  (“finite reservoir”), allowing the possibility of observing and studying 2CK. The 2CK Hamiltonian (Eq. 6.2) has three possible ground states, depending on the relative couplings to the two reservoirs: 1CK with the finite reservoir ( $J_{\text{fr}} > J_{\text{ir}}$ ), 1CK with the infinite reservoir ( $J_{\text{ir}} > J_{\text{fr}}$ ), and 2CK at the quantum critical point  $J_{\text{fr}} = J_{\text{ir}}$ .

In Fig. 6.2, we demonstrate that the small quantum dot can act as a tunable magnetic impurity and display the single-channel Kondo effect. If the small quantum

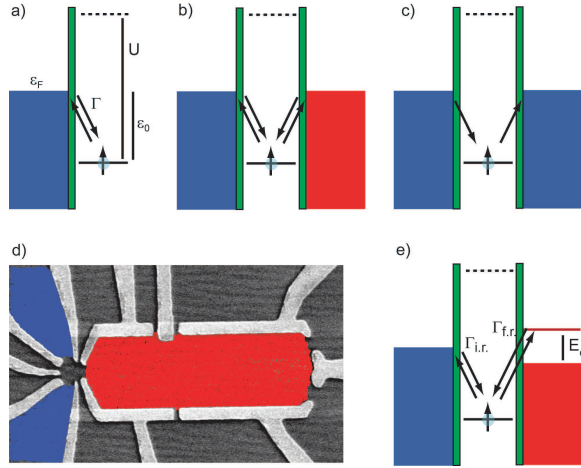


Figure 6.1: Single Channel Kondo Effect (1CK). (a) The Anderson model describes a magnetic impurity in a metal as a single spin-degenerate state (right side of green barrier) coupled to a Fermi reservoir of electrons (left). Coulomb interaction  $U$  between localized electrons favors having only a single electron in the localized state. The antiferromagnetic coupling between the localized spin and the reservoir depends on the tunneling rate  $\Gamma$ , the depth of the level  $\epsilon_0$ , and  $U$ , according to  $J \sim \Gamma U / (\epsilon_0(\epsilon_0 + U))$  [75]. At low temperature, high-order tunneling processes between the local state and the Fermi reservoirs coherently add together to screen the localized electron spin. (b) Two Channel Kondo Effect (2CK). A localized electron is now coupled to *two independent Fermi reservoirs* (blue and red). If the two independent reservoirs are equally coupled to the localized spin, each will individually attempt to screen the spin, effectively overscreening the spin and forming a highly-correlated electron state. (c) Physically separating two reservoirs does not suffice to make them independent. If a localized electron can hop off the site to the right reservoir and a new electron can hop onto the site from the left, the two reservoirs will cooperate in screening the localized spin. To create two independent screening channels, processes which transfer electrons from one reservoir to another must be suppressed. (d) Experimental Realization of 2CK. We add an additional finite reservoir (red) to an artificial magnetic impurity connected to an infinite reservoir comprised of two conventional leads (blue). (e) Coulomb blockade suppresses exchange of electrons between the finite reservoir and the normal leads at low temperature. The two reservoirs (blue and red) hence act as two independent screening channels (see Text.)

dot has an odd number of electrons, it has a net spin and acts as a magnetic impurity. With gate  $n$  de-energized ( $0 V$ ), the system has three conventional leads (blue and red in Fig. 6.1), all of which cooperate to screen the magnetic impurity with a single energy scale  $T_K$ . At temperature  $T \lesssim T_K$  the Kondo effect enhances scattering and hence conductance from one lead to another. We measure the conductance  $g \equiv dI/dV_{ds}|_{V_{ds}=0}$  between the two blue leads. As temperature is increased, the Kondo state is partially destroyed, so the conductance decreases (Fig. 6.2(b)).

The conductance as a function of temperature (e.g. Fig. 6.2(b) inset) matches the expected empirical form [77] with the addition of a constant offset  $a$ :

$$g(T) = g_0 f(T/T_K) + a \equiv \tilde{g}(T) + a. \quad (6.3)$$

$g_0 < 2e^2/h$  reflects the asymmetry of coupling to the two conventional leads that comprise the infinite reservoir. At  $c = -282 mV$ , we find that the offset  $a = 0.21e^2/h$  is constant over the Kondo valley near  $sp = -230 mV$ . At  $c = -244 mV$ , for the same number of electrons in the small dot ( $sp \sim -275 mV$ ) we again find a constant offset  $a = 0.09e^2/h$  and a strongly-varying  $T_K$ . As expected,  $T_K$  is higher for  $c = -244 mV$  because the dot is more strongly coupled to the right lead, increasing the total  $\Gamma$  of the system. All results presented in this paper are for this electron occupancy, although we have observed similar behavior in the next Kondo valley (two fewer electrons in small dot).

Having demonstrated that the small quantum dot acts as a magnetic impurity, we now begin to form the finite reservoir by applying negative gate voltage to  $n$ . Setting  $sp$  to the middle of a Kondo valley in Fig. 6.2(b) or (c), we observe enhanced differential conductance  $g(T, V_{ds}) \equiv dI/dV_{ds}$  near zero bias compared with finite  $V_{ds}$  (Fig. 6.3(b) and (e), respectively). This is a manifestation of an enhanced density of states at the Fermi level consistent with Kondo effect. Remarkably, the zero bias enhancement

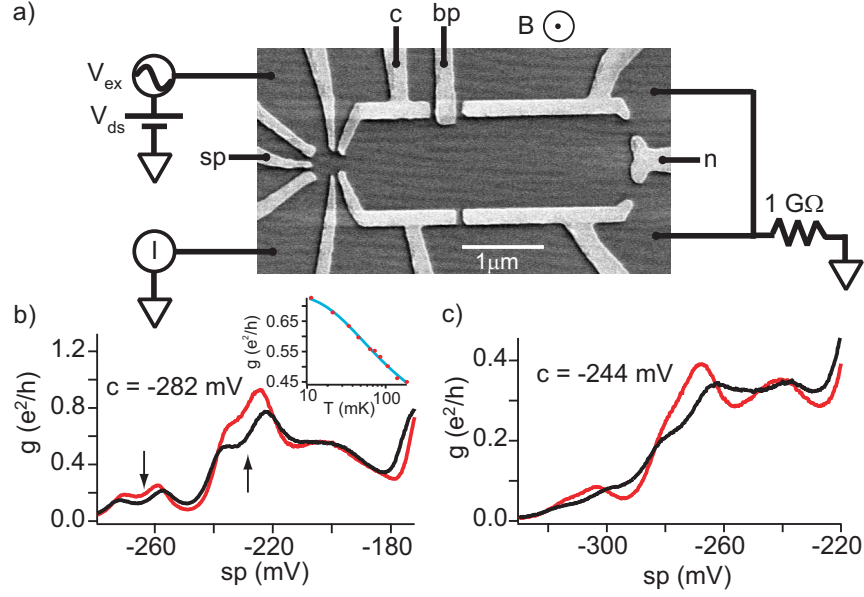


Figure 6.2: (a) Scanning electron micrograph of a device similar to that measured. The device consists of a small quantum dot (magnetic impurity, left) coupled to conventional leads (top and bottom left) and to a large quantum dot (finite reservoir, right). Electrons are depleted under every gate by application of negative voltages. In the experiments described here, voltages on gates labeled  $c$ ,  $bp$ ,  $sp$ , and  $n$  are varied. All transport measurements presented in Fig. 6.3, 6.4, and 6.5 are measured with source and drain connected as shown, in a magnetic field of  $130\text{ mT}$  normal to the plane of the 2DEG. (b) With gate voltage  $n = 0$ , the large dot opens into an infinite reservoir. Arrows mark regions where the small dot has an unpaired spin, leading to enhanced conductance at  $12\text{ mK}$  (red) compared to  $50\text{ mK}$  (black). Fitting the temperature dependence of the conductance (b inset), we find Kondo temperature ranges from  $110$  to  $300\text{ mK}$ , see Supplementary Information. In (c), the data from (b) are shown for a different strength of tunnel coupling to the right lead:  $c = -244\text{ mV}$  instead of  $-282\text{ mV}$ . From temperature dependence of (c), we find  $T_K$  ranges from  $180$  to  $320\text{ mK}$ .

changes to zero bias suppression as the reservoir becomes finite with integer occupancy (Fig. 6.3(f)), signaling that a single-channel Kondo state has formed solely with the finite reservoir. This occurs for  $J_{\text{fr}} > J_{\text{ir}}$ , as shown in more detail below. With slightly weaker coupling to the finite reservoir (Fig. 6.3(c),  $J_{\text{ir}} > J_{\text{fr}}$ ), the Kondo state is formed solely with the infinite reservoirs, again provided that the finite reservoir has integer occupancy. The width in  $V_{ds}$  of the enhancement and suppression denoted by arrows in Fig. 6.3(c) and (f), respectively, are remarkably similar, indicating that the characteristic energy scale  $T_K$  is the same in the two cases (cf. Fig (5(e))).

In Fig. 6.4, we provide further evidence that, with the finite reservoir formed, two independent 1CK states can exist depending on the relative coupling of the small dot to the two reservoirs. We have fine control over the occupancy of both the finite reservoir and the small dot with gates  $bp$  and  $sp$ , as shown in Fig. 6.4(a) and more completely in Supplementary Information. Conductance ( $g(T) \equiv g(0, T)$ ) at weak coupling to the finite reservoir ( $J_{\text{ir}} > J_{\text{fr}}$ ) fits the expected empirical form of Eq. (4). In fact, we fix the offset  $a = 0.21e^2/h$ , as determined with the finite reservoir unformed. Fig. 6.4(c) shows that the conductance  $g(T)$  at many points in  $(sp, bp)$  (Fig. 6.4(a)) can be collapsed onto a universal curve. The differential conductance  $g(V_{ds}, T)$  of a 1CK system is further expected to follow a specific form as a function of both bias and temperature [112]. For substantially asymmetric coupling to the two conventional leads that form the infinite reservoir ( $g_0 \ll 2e^2/h$ ),

$$\frac{g(0, T) - g(V_{ds}, T)}{T^\alpha} = \kappa \left( \frac{eV_{ds}}{kT} \right)^2, \quad (6.4)$$

where the exponent  $\alpha = 2$  is characteristic of 1CK, and  $\kappa = (g_0/T_K^\alpha)(3/(2\pi^2))$ . This equation describes the low-energy Fermi-liquid behavior, at an energy scale substantially below  $kT_K$ . For a channel-asymmetric 2CK system,  $T_K$  is replaced by a crossover

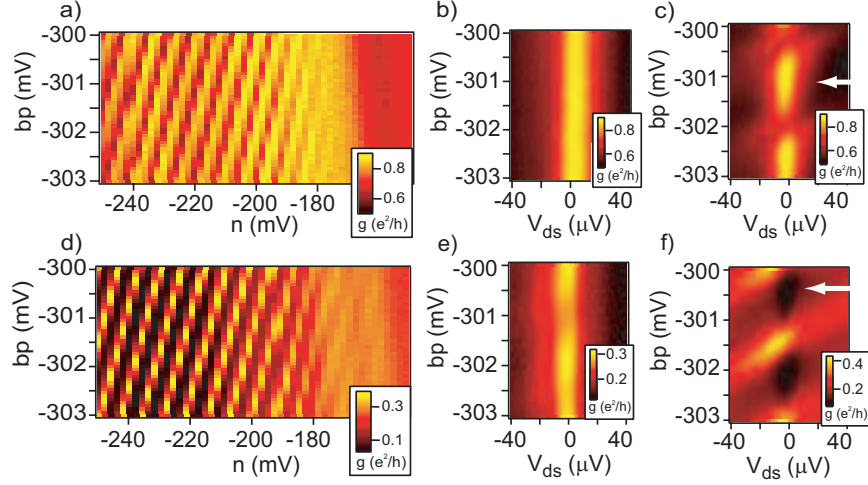


Figure 6.3: The formation of two competing 1CK states with two different reservoirs. (a)  $sp$  is set so that the small dot has an unpaired spin (middle of a Kondo valley), and  $c$  is set to  $-282\text{ mV}$ . Conductance is shown as a function of  $n$  and  $bp$ . With  $n > -180\text{ mV}$ , varying  $bp$  has little effect on the conductance. As  $n$  is made more negative, the reservoir becomes finite and a series of stripes in the conductance map reflects Coulomb blockade in the finite reservoir (see Supplementary Information for explanation of the modulation.) In (b) and (c), differential conductance as a function of bias ( $V_{ds}$ ) and  $bp$  is shown for  $n = -170\text{ mV}$  and  $n = -224\text{ mV}$ , respectively. In (b), there is clear zero-bias enhancement, consistent with Kondo effect. In (c), the zero-bias enhancement (indicated by the arrow) is modulated by the charge state of the large dot. (d) Same as (a), except with stronger interdot coupling:  $c = -244\text{ mV}$ . (e) As in (b), we observe a clear zero-bias conductance enhancement for  $n = -170\text{ mV}$ . (f) However, in this case at  $n = -224\text{ mV}$  the zero-bias enhancement changes to zero-bias suppression, denoted by the arrow. Here the local spin forms a Kondo state with the finite reservoir, suppressing conductance through the small quantum dot (see Text.)

scale  $T_\Delta$ , a measure of the channel asymmetry, which goes to zero when  $J_1 = J_2$  [24]. Fig. 6.4(d) demonstrates excellent 1CK scaling at temperatures of 12, 24, 28, and 38mK, all well below  $T_K$ . A nonlinear fit to the data in Fig. 6.4(d) yields  $\alpha = 1.72 \pm 0.40$  (95% CL), consistent with  $\alpha = 2$ .

In Fig. 6.4(e-h), we demonstrate that at stronger coupling to the finite reservoir ( $J_{\text{fr}} > J_{\text{ir}}$ ) the small dot forms a Kondo state with the finite reservoir, as manifested by low-energy suppression rather than enhancement of conductance between the normal leads of the small dot. We must modify the form we use to fit the temperature dependence to reflect this inversion:

$$g(T) = g_0 (1 - f(T/T_K)) + a \equiv -\tilde{g}(T) + a + g_0. \quad (6.5)$$

We again fix the constant offset  $a = 0.09e^2/h$  to match its value before formation of the finite reservoir (Fig. 6.2(c)). Again temperature dependence at multiple points in  $(sp, bp)$  (Fig. 6.4(e)) collapse onto a single normalized Kondo form  $\tilde{g}/g_0$  vs  $T/T_K$  (Fig. 6.4(g)), providing strong evidence that a distinct 1CK state has formed with the finite reservoir. Furthermore, using the same scaling relation as above (Eq. (6.9)) the data again collapse onto a single (inverted) curve at low bias and temperature (Fig. 6.4(h)).

Having established the existence of two distinct Kondo ground states – depending on the ratio  $J_{\text{ir}}/J_{\text{fr}}$  – we next demonstrate the tunability necessary to reach the 2CK state,  $J_{\text{ir}} = J_{\text{fr}}$ . By setting the tunnel coupling to the finite reservoir to an intermediate value, we can observe *either* zero-bias enhancement or zero-bias suppression (marked by arrows in Fig. 6.5(a)), depending on the electrostatic state of the finite reservoir, which can be fine-tuned with gate  $bp$ . This is expected [23], since the antiferromagnetic coupling to a reservoir depends not only on a tunneling rate but also on the energy required to transfer an electron from the local site to that reservoir.

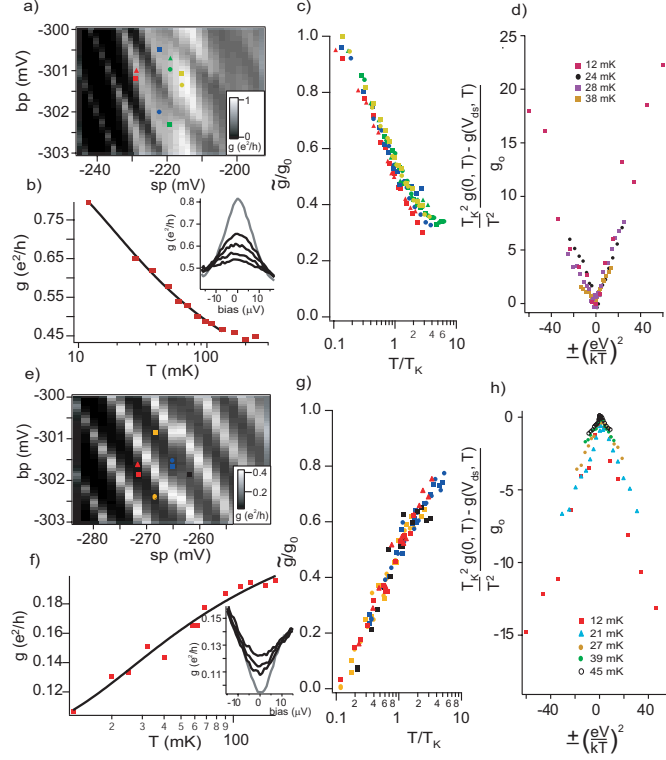


Figure 6.4: Energy dependence of Kondo effect, with the finite reservoir formed. (a) - (d) Antiferromagnetic coupling to the infinite reservoir (normal leads) is stronger than coupling to the finite reservoir:  $c = -282$  mV. (a) Conductance as a function of gates  $sp$  and  $bp$ , at  $V_{ds}=0$ . (b) Any point in  $(sp, bp)$  such that the occupancy of the small dot is odd and that of the finite reservoir is integer shows enhanced conductance at low temperature and low bias (inset: 12 mK, grey, to 60 mK), and a temperature dependence consistent with Kondo effect. (c) The normalized dependence of conductance on temperature is uniform for different points in  $(sp, bp)$  space, while  $T_K$  ranges from 50mK to 180mK.  $\tilde{g} \equiv g - a$  is the conductance with the temperature-independent offset subtracted off. (d) Plotting a specific combination of temperature and bias collapses the data for a single point in  $(sp, bp)$  space ( $T_K = 175$  mK,  $g_0 = 0.75e^2/h$ ) onto a single V-shaped curve, corresponding to the scaling relation predicted for 1CK (Eq. (6.9)). (e) - (h) Kondo effect with the finite reservoir:  $c = -244$ mV. (e) Conductance as a function of  $sp$  and  $bp$ : conductance is now suppressed rather than enhanced at low bias and temperature (cf. Fig. 6.3(f)). (f) Fitting the conductance as a function of temperature to the empirical form we expect for 1CK with the finite reservoir (Eq. 6.5) we find that  $T_K$  ranges from 30mK to 130mK. (g) We again normalize and collapse the temperature dependence at several points in  $(sp, bp)$  onto a single curve. (h) We collapse differential conductance data like those in inset (f) (12 mK, grey, to 30 mK) at a single point in  $(sp, bp)$  onto a single inverted V-shaped curve using the same temperature-bias scaling as in (d). Deviations from perfect scaling may be related to the slightly lower Kondo temperature ( $T_K = 120$ mK,  $g_0 = 0.16 e^2/h$ ).

$bp$  tunes that addition energy for the finite reservoir, modifying  $J_{\text{fr}}$  while keeping  $J_{\text{ir}}$  nearly constant. The region in  $(sp, bp)$  of suppressed conductance (red) grows rapidly with increasing coupling to the finite reservoir, as seen in Fig. 6.5(b, c, and d) for  $c = -258, -256, -254\text{mV}$ , respectively.

The evolution of  $dI/dV_{ds}$  from zero-bias enhancement to zero-bias suppression as a function of coupling gate  $c$  may be seen most clearly in Fig. 6.5(e). In no case do we observe a clear cusp at low  $V_{ds}$  ( $G \sim \text{const} - \sqrt{V_{ds}}$ ). However, combining the dependence of differential conductance on both  $V_{ds}$  and temperature in a scaling plot produces results indicative of 2CK [31, 113]:

$$\frac{g(0, T) - g(V_{ds}, T)}{T^{\alpha_2}} = \kappa_2 \Gamma\left(\frac{eV_{ds}}{kT}\right). \quad (6.6)$$

Here  $\alpha_2 = 0.5$ ,  $\kappa_2 = (g_0/2)(\pi/T_{2CK})^{\alpha_2}$ , and

$$\Gamma(x) = 1 - F_{2CK}(x/\pi) \approx \begin{cases} \frac{3}{\pi}\sqrt{x} - 1 & \text{for } x \gg 1 \\ cx^2 & \text{for } x \ll 1 \end{cases} \quad (6.7)$$

with  $c \approx 0.0758$ .  $F_{2CK}$  is found by conformal field theory [31, 24, 114], which is applicable for the case of strong asymmetry in coupling to the two conventional leads that constitute the infinite reservoir.

Figure 6.5(f) shows that data at various temperatures and biases collapse onto each other and match the conformal field theory prediction (Eq. (6.6)), which is scaled vertically by an arbitrary factor. The horizontal axis is plotted as  $(eV_{ds}/kT)^{0.5}$ , to emphasize that  $g \sim \sqrt{eV_{ds}/kT} - 1$  for  $eV_{ds}/kT \gg 1$ .

In Fig. 6.5(g) we show the same data scaled as would be appropriate for 1CK (Eq. (6.9)) instead of 2CK. As anticipated, this scaling fails completely: scaled data for different temperatures deviate from each other even near zero bias. A two dimensional nonlinear fit to the data in Fig. 6.5(f) produces a value  $\alpha_2 = 0.62 \pm 0.21$  (95% CL),

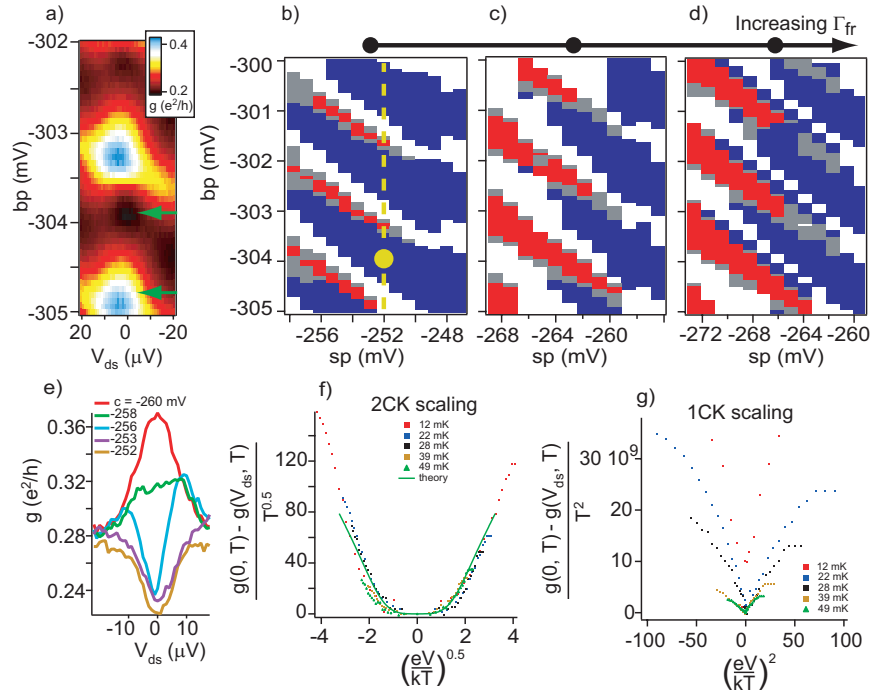


Figure 6.5: Evidence for 2CK physics. (a) Differential conductance as a function of  $bp$  and  $V_{ds}$  in the middle of a Kondo valley, with intermediate coupling to the finite reservoir  $c = -258\text{mV}$ . In contrast with Fig 6.3(c) and 6.3(f), here we observe *both* zero-bias enhanced and zero-bias suppressed conductance (marked by arrows) by fine-tuning  $bp$ . (b)-(d) At  $c = -258, -256,$  and  $-254\text{mV}$ , conductance may be either enhanced or suppressed at zero bias, depending on the fine tuning of the electrostatic potentials of the small dot and finite reservoir with gates  $sp$  and  $bp$ , respectively. Red and blue indicate regions of suppressed conductance or enhanced conductance, respectively, while gray indicates relatively flat conductance around  $V_{ds} = 0$ . Increased coupling to the finite reservoir expands the region of suppressed conductance. (e) Differential conductance near zero bias evolves with coupling  $c$  from zero-bias enhancement to zero-bias suppression. For each curve,  $sp$  sets the small dot in the middle of a Kondo valley and  $bp$  sets the finite reservoir midway between two charge degeneracy points. (f,g) Tuning  $bp$  near  $-304.7\text{mV}$  (marked by arrow in (a)), we observe that differential conductance depends on bias and temperature with scaling law  $(eV_{ds}/kT)^{0.5}$ , consistent with 2CK (f) and inconsistent with 1CK (g, which has scaling law  $(eV_{ds}/kT)^2$ ). In the Supplementary Information we show the converse, namely in the 1CK region the 2CK scaling law does not fit, while the 1CK scaling does. A two dimensional nonlinear fit to the data set used for (f) and (g) yields a critical exponent  $\alpha_2 = 0.62 \pm 0.21$

consistent with 2CK behavior up to remarkably high energies (naively, we would expect  $T_{2CK} \sim T_K^2/E_C \approx 20\text{mK}$  [?], however larger  $T_{2CK}$  values are anticipated, for example, in the presence of charge fluctuations [102].) In the Supplementary Information, we include various scaling plots with  $(eV/kT)^2$  and  $(eV/kT)^{0.5}$  to show the deviations from scaling for 2CK and 1CK.

In this paper, we have presented data consistent with two independent 1CK states, along with a study of the associated 2CK state. We have observed similar behavior upon thermally cycling the device and all gates surrounding the small quantum dot can drive the phase transition in the expected manner.

Acknowledgements:

We would like to thank Avi Schiller, Eran Lebanon, Frithjof Anders, Eran Sela, Charlie Marcus, Leonid Glazman, Karyn LeHur, and Ian Affleck for valuable discussions. EL and FA also performed NRG calculations which gave us crucial intuition regarding where we were in parameter space. Scott Roy helped us understand how to perform nonlinear fits to determine the exponents  $\alpha, \alpha_2$  for the energy dependence in both the 1CK and 2CK regimes. Support: NSF CAREER Award, US-Israel BSF Award #2004278, DIP, ISF. RMP ARO Fellowship.

## 6.2 Supplementary Information for 2CK

Measurement techniques

Measurements of differential conductance ( $g = dI/dV_{ds}$ ) were performed in an Oxford TLM dilution refrigerator. (The sample is located inside the mixing chamber.) We measured  $g$  using standard ac lockin techniques (using PAR 124a with 116 preamp) at 337 Hz with a RMS excitation ( $V_{ex}$ ) of either  $1\mu V$  or  $2\mu V$ , depending on temperature

( $eV_{ex} \leq kT$ ), and measure current with a DL Instruments 1211 preamplifier. To probe nonequilibrium properties, we also added a dc voltage bias  $V_{ds}$  to the ac voltage  $V_{ex}$  through a passive circuit. Details of the electronics and filtering are contained in ref [115].

### Determination of $T_K$

When the quantum dot has an odd number of electrons and the finite reservoir is not formed (e.g. Fig. 6.2), the quantum dot displays the usual signatures of Kondo effect. The Kondo temperature is extracted by fitting the temperature dependence of the conductance (e.g. Fig. 6.2(b) inset) to Eq. 6.3,

$$g(T) = g_0 f(T/T_K) + a, \quad (6.8)$$

where  $f(T/T_K)$  is the expected empirical form given by [77]. In Fig. S6.6(a),  $T_K$  as a function of  $sp$  is given for  $c = -282 \text{ mV}$  (corresponding to a single Kondo valley in Fig. 6.2(b)). By measuring the conductance as a function of  $sp$  and bias voltage  $V_{ds}$  in Fig. S6.6(b), we observe the Kondo-enhanced density of states at the Fermi level (marked by the arrow). In Fig. S6.6(c), the data similar to (a) are shown for a different strength of tunnel coupling to the right lead:  $c = -244 \text{ mV}$  instead of  $-282 \text{ mV}$ .

We do not have a detailed physical picture of the temperature independent constant offset  $a$  in Eq. 6.8. When left as a free fitting parameter, we find it does not vary much across a single valley, so we choose to hold it constant as  $sp$  is varied over a single valley. Meanwhile,  $T_K$  varies substantially across the valley (Fig. S6.6(a) and (c)), reaching a minimum in mid-valley as expected and observed in previous experiments [75, 77, 116]. In addition, we note the fitting function only determines the value of  $g_0$  and  $T_K$ . The main conclusions of the paper are drawn from the scaling curves from Figures 6.4 and 6.5, which do not depend on these values, just the differences in  $g$ .

### Conductance of the double dot system

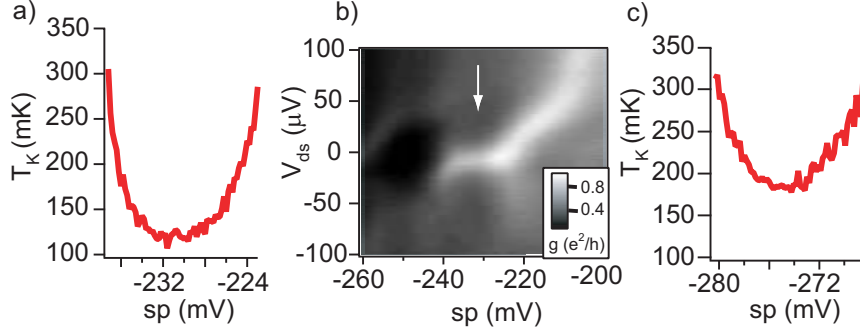


Figure 6.6: Kondo temperature of the small quantum dot without finite reservoir formed.

In Fig. S6.7(a), conductance as a function of  $sp$  and  $bp$  is measured through the small dot: current path shown in Fig. S6.7(c). The main, broad conductance features of the small dot depend only on  $sp$ , as  $bp$  is  $> 1\mu m$  away and thus has a very small capacitance to the small dot. The gate voltage  $c$  is set to have enhanced low-energy conductance in the Kondo valleys of the small dot, at around  $sp = -260\text{mV}$  and  $-285\text{mV}$ . Gates  $sp$  and  $bp$  both strongly capacitively couple to the energy of the large dot, affecting its occupancy. The diagonal stripes in the conductance of the small dot are associated with the charge degeneracy points of the large dot. Due to the large capacitive coupling between the two dots, adding an electron to the large dot discretely changes the electrostatic environment of the small dot, which changes its conductance [117]. More complex phenomena, including  $SU(4)$  [118] or two channel Kondo physics [102], may also affect the conductance near the charge degeneracy points. However, we observe very weak temperature dependence in these regimes.

In Fig. S6.7(b), the same type of data as (a) is shown for stronger coupling between the two dots, leading to suppressed low-temperature conductance in the Kondo valley at around  $sp = -280\text{mV}$ . In Fig. S6.7(e) conductance as a function of  $sp$  and  $bp$  is measured through both dots in series: current path shown in Fig. S6.7(d). The charge

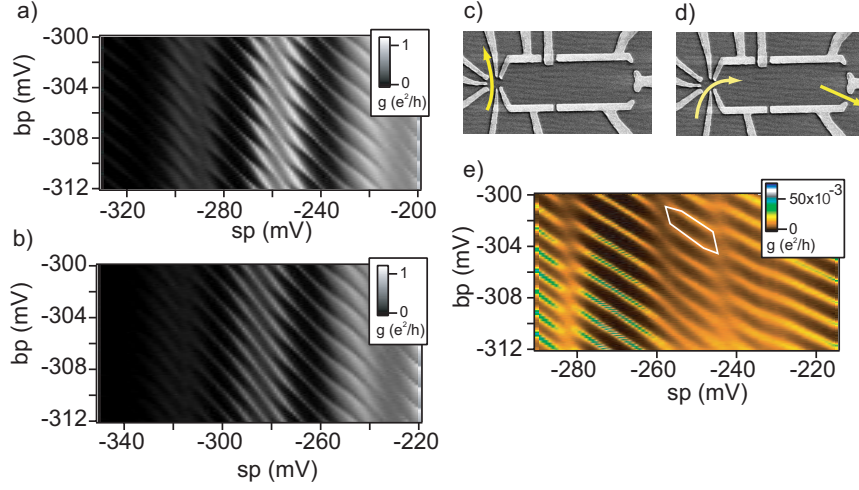


Figure 6.7: Determining the charge state of the two dots.

degeneracy points for both the large and small quantum dots are apparent from these data, allowing the charge stability hexagon to be drawn (white hexagon superimposed as a guide to the eye).

### Scaling analysis of 1CK data

In Fig. S6.8, we analyze the single channel Kondo data presented in Figure 6.4 in terms of two channel Kondo. From the Eq. 6.9,

$$\frac{g(0, T) - g(V_{ds}, T)}{T^\alpha} = \kappa \left( \frac{eV_{ds}}{kT} \right)^2, \quad (6.9)$$

with  $\alpha = 2$  is the appropriate scaling function for 1CK. In Fig. S6.8(a), we show the same scaling plot as Fig. 6.4(d) of Text for 1CK behavior, without normalizing with  $T_K$  or  $g_0$ .

In Fig. S6.8(b), the same data from Fig. S6.8(a) is scaled in a way appropriate for

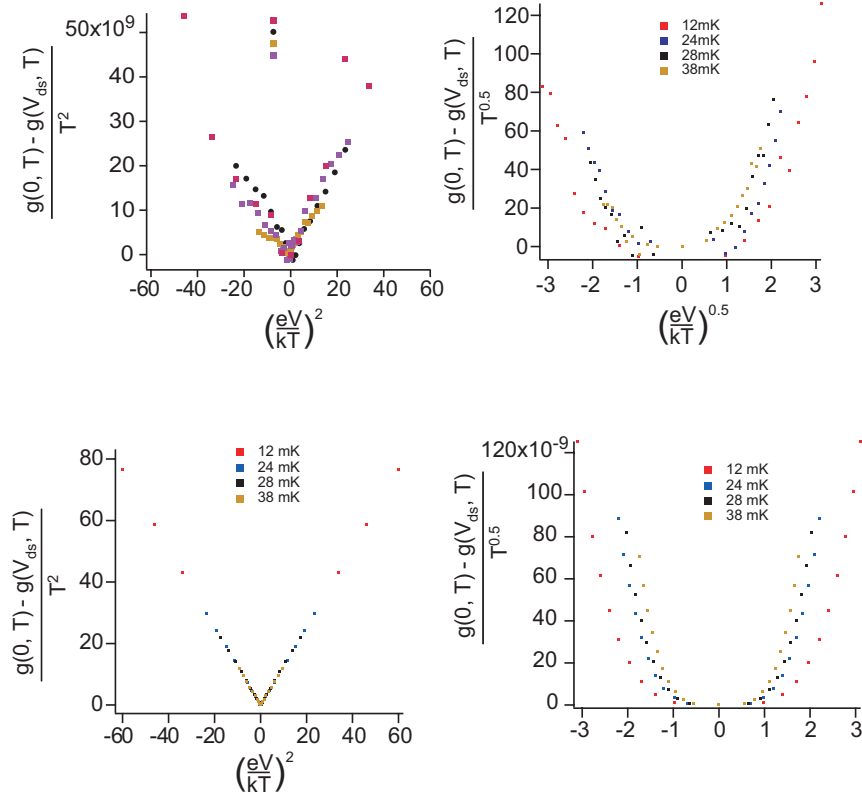


Figure 6.8: Scaling of 1CK

2CK behavior,  $\alpha = 0.5$ . In Fig. S6.8(c) and (d) we simulate data for ideal 1CK ( $\alpha = 2$ ) scaling. For Fig. S6.8(d), the same simulated data from Fig. S6.8(c) is plotted with 2CK scaling  $\alpha = 0.5$ . Comparing Fig. S6.8(b) and (d), the simulated data deviates from perfect scaling similar to the 1CK data, allowing us to visually discriminate 1CK behavior from 2CK behavior. The nonlinear fits presented in the Text quantify these observations.

# Bibliography

- [1] S.M. Sze. *Physics of Semiconductor Devices*. John Wiley and Sons, second edition, 1981.
- [2] P. W. Anderson. More is different. *Science*, 177:393 – 396, 1972.
- [3] J. Kondo. Resistance minimum in dilute magnetic alloys. *Prog. Theor. Phys.*, 32:37, 1964.
- [4] M. Taut, A. Ernst, and H. Eschrig. Two electrons in an external oscillator potential: exact solution versus one-particle approximations. *Journal of Physics B (Atomic, Molecular and Optical Physics)*, 31:2689 – 708, 1998.
- [5] P. Nozieres and D. Pines. *The Theory of Quantum Liquids*. Perseus Books, 1999.
- [6] M. Stopa. Quantum dot self-consistent electronic structure and the Coulomb blockade. *Physical Review B*, 54(19):13767 – 83, NOV 1996.
- [7] N.W. Ashcroft and N.D. Mermin. *Solid State Physics*. Saunders College Publishing, first edition, 1976.
- [8] Yu. Ye. Lozovik and V. I. Yudson. Crystallisation of a two-dimensional electron gas in magnetic field. *Zhurnal Eksperimental'noi i Teoreticheskoi Fiziki, Pis'ma v Redaktsiyu*, 22:26 – 8, 1975.

- [9] S. Kicin, A. Pioda, T. Ihn, M. Sigrist, A. Fuhrer, K. Ensslin, M. Reinwald, and W. Wegscheider. Spatially highly resolved study of afm scanning tip-quantum dot local interaction. *New Journal of Physics*, 7, 2005.
- [10] P. Fallahi, A. C. Bleszynski, R. M. Westervelt, J. Huang, J. D. Walls, E. J. Heller, M. Hanson, and A. C. Gossard. Imaging a single-electron quantum dot. *Nano Letters*, 5:223 – 6, 2005.
- [11] B. Spivak and S. A. Kivelson. Phases intermediate between a two-dimensional electron liquid and wigner crystal. *Physical Review B*, 70:155114, 2004.
- [12] B. I. Halperin, A. Stern, Y. Oreg, J. N. H. J. Cremers, J. A. Folk, and C. M. Marcus. Spin-orbit effects in a GaAs quantum dot in a parallel magnetic field. *Physical Review Letters*, 86:2106 – 9, 2001.
- [13] R. M. Potok, J. A. Folk, C. M. Marcus, V. Umansky, M. Hanson, and A. C. Gossard. Spin and polarized current from coulomb blockaded quantum dots. *Physical Review Letters*, 91:016802, 2003.
- [14] D. M. Zumbuhl, J. B. Miller, C. M. Marcus, K. Campman, and A. C. Gossard. Spin-orbit coupling, antilocalization, and parallel magnetic fields in quantum dots. *Physical Review Letters*, 89:276803 – 4, 2002.
- [15] J. B. Miller, D. M. Zumbuhl, C. M. Marcus, Y. B. Lyanda-Geller, D. Goldhaber-Gordon, K. Campman, and A. C. Gossard. Gate-controlled spin-orbit quantum interference effects in lateral transport. *Physical Review Letters*, 90:076807 – 1, 2003.

- [16] Yu. V. Sharvin and N. I. Bogatina. Electron focusing in a metal by a longitudinal magnetic field. *Zhurnal Eksperimental'noi i Teoreticheskoi Fiziki*, 56:772 – 9, 1969.
- [17] V. S. Tsoi and I. I. Razgonov. Reflection of conductivity electrons by the surface of a tungsten sample. *Zhurnal Eksperimental'noi i Teoreticheskoi Fiziki*, 74:1137 – 46, 1978.
- [18] R. M. Potok, J. A. Folk, C. M. Marcus, and V. Umansky. Detecting spin-polarized currents in ballistic nanostructures. *Physical Review Letters*, 89:266602, 2002.
- [19] H. Vanhouten, C. W. J. Beenakker, J. G. Williamson, M. E. I. Broekaart, P. H. M. Vanloosdrecht, B. J. Vanwees, J. E. Mooij, C. T. Foxon, and J. J. Harris. Coherent electron focusing with quantum point contacts in a two-dimensional electron gas. *Physical Review B*, 39:8556 – 75, 1989.
- [20] D. S. Duncan, D. Goldhaber-Gordon, R. M. Westervelt, K. D. Maranowski, and A. C. Gossard. Coulomb-blockade spectroscopy on a small quantum dot in a parallel magnetic field. *Applied Physics Letters*, 77:2183 – 5, 2000.
- [21] R. Berkovits I. L. Kurland I. L. Aleiner B. L. Altshuler J. A. Folk, C. M. Marcus. Ground state spin and Coulomb blockade peak motion in chaotic quantum dots. *Physica Scripta*, T90, 2001.
- [22] M. Greven, R. J. Birgeneau, and U. J. Wiese. Monte Carlo study of correlations in quantum spin ladders. *Physical Review Letters*, 77:1865 – 8, 1996.
- [23] Y. Oreg and D. Goldhaber-Gordon. Two-channel Kondo effect in a modified single electron transistor. *Physical Review Letters*, 90:136602, 2003.

- [24] M. Pustilnik, L. Borda, L.I. Glazman, , and J. von Delft. Quantum phase transition in a two-channel-Kondo quantum dot device. *Physical Review B*, 69:115316, 2004.
- [25] T. Kuzmenko, K. Kikoin, and T. Avishai. Two-channel kondo tunneling in triple quantum dot. *LANL preprint archives*, pages cond-mat/0211281, 2003.
- [26] P. W. Anderson. *Basic Notions of Condensed Matter Physics*. Addison-Wesley, 1984.
- [27] P.W. Anderson. Localized magnetic states in metals. *Phys. Rev.*, 124:41, 1961.
- [28] D. Goldhaber-Gordon, Hadas Shtrikman, D. Mahalu, D. Abusch-Magder, U. Meirav, and M. A. Kastner. Kondo effect in a SET. *Nature*, 391:156–159, 1998.
- [29] P. Nozieres and A. Blandin. Kondo effect in real metals. *Journal de Physique*, 41:193 – 211, 1980.
- [30] A. M. Tsvelick. The transport properties of magnetic alloys with multi-channel kondo impurities. *Journal of Physics: Condensed Matter*, 2:2833 – 40, 1990.
- [31] I. Affleck and A. W. W. Ludwig. Exact conformal-field-theory results on the multichannel Kondo effect: single-fermion Green’s function, self-energy, and resistivity. *Physical Review B*, 48:7297 – 321, 1993.
- [32] C. L. Seaman, M. B. Maple, B. W. Lee, S. Ghamaty, M. S. Torikachvili, J. S. Kang, L. Z. Liu, J. W. Allen, and D. L. Cox. Evidence for non-Fermi-liquid behavior in the Kondo alloy  $Y_{1-x}U_xPd_3$ . *Physical Review Letters*, 67:2882 – 2885, 1991.

- [33] D. L. Cox. Quadrupolar Kondo effect in uranium heavy-electron materials. *Physical Review Letters*, 59:1240 – 1243, 1987.
- [34] D. C. Ralph and R. A. Buhrman. Observations of Kondo scattering without magnetic-impurities - a point contact study of 2-level tunneling systems in metals. *Physical Review Letters*, 69:2118 – 2121, 1992.
- [35] D. C. Ralph, A. W. W. Ludwig, J. von Delft, and R. A. Buhrman. 2-channel Kondo scaling in conductance signals from 2-level tunneling systems. *Physical Review Letters*, 72:1064 – 1067, FEB 1994.
- [36] N. S. Wingreen, B. L. Altshuler, and Y. Meir. 2-channel Kondo scaling in conductance signals from 2-level tunneling systems - comment. *prl*, 75:769 – 769, 1995.
- [37] D. L. Cox and A. Zawadowski. Exotic Kondo effects in metals: magnetic ions in a crystalline electric field and tunnelling centres. *Advances In Physics*, 47:599 – 942, 1998.
- [38] S. Sachdev. Quantum phase transitions. *Physics World*, 12:33 – 8, 1999.
- [39] S. R. Patel, S. M. Cronenwett, D. R. Stewart, A. G. Huibers, C. M. Marcus, C. I. Duruoz, J. S. Harris, K. Campman, and A. C. Gossard. Statistics of coulomb blockade peak spacings. *Physical Review Letters*, 80:4522 – 5, 1998.
- [40] D. R. Stewart, D. Sprinzak, C. M. Marcus, C. I. Duruoz, and J. S. Harris. Correlations between ground and excited state spectra of a quantum dot. *Science*, 278:1784 – 8, 1997.
- [41] J. A. Folk, R. M. Potok, C. M. Marcus, and V. Umansky. A gate-controlled bidirectional spin filter using quantum coherence. *Science*, 299:679 – 82, 2003.

- [42]
- [43] D. H. Cobden, M. Bockrath, P. L. McEuen, A. G. Rinzler, and R. E. Smalley. Spin splitting and even-odd effects in carbon nanotubes. *Physical Review Letters*, 81:681 – 4, 1998.
- [44] D. C. Ralph, C. T. Black, and M. Tinkham. Gate-voltage studies of discrete electronic states in aluminum nanoparticles. *Physical Review Letters*, 78:4087 – 90, 1997.
- [45] S. Lindemann, T. Ihn, T. Heinzel, W. Zwerger, K. Ensslin, K. Maranowski, and A. C. Gossard. Stability of spin states in quantum dots. *Physical Review B*, 66:195314, 2002.
- [46] J. Weis, R. J. Haug, K. Vonklitzing, and K. Ploog. Competing channels in single-electron tunneling through a quantum dot. *Physical Review Letters*, 71:4019 – 22, 1993.
- [47] L. P. Kouwenhoven, T. H. Oosterkamp, M. W. S. Danoesastro, M. Eto, D. G. Austing, T. Honda, and S. Tarucha. Excitation spectra of circular, few-electron quantum dots. *Science*, 278:1788 – 92, 1997.
- [48] Xuedong Hu and S. Das Sarma. Generating and detecting electron spin entangled states in nanostructures. *Proceedings of the SPIE - The International Society for Optical Engineering*, 5472:107 – 15, 2003.
- [49] D. Weinmann, W. Hausler, and B. Kramer. Spin blockades in linear and nonlinear transport through quantum dots. *Physical Review Letters*, 74:984 – 7, 1995.
- [50] P. Recher, E. V. Sukhorukov, and D. Loss. Quantum dot as spin filter and spin memory. *Physical Review Letters*, 85:1962 – 5, 2000.

- [51] R. Fiederling, M. Keim, G. Reuscher, W. Ossau, G. Schmidt, A. Waag, and L. W. Molenkamp. Injection and detection of a spin-polarized current in a light-emitting diode. *Nature*, 402:787 – 90, 1999.
- [52] A. S. Sachrajda, P. Hawrylak, M. Ciorga, C. Gould, and P. Zawadzki. Spin polarized injection into a quantum dot by means of the spatial separation of spins. *Physica E*, 10:493 – 8, 2001.
- [53] D. Loss D.D. Awschalom and N. Samarth. *Semiconductor Spintronics and Quantum Computation*. Springer-Verlag, Berlin, 2002.
- [54] J. M. Kikkawa and D. D. Awschalom. Resonant spin amplification in n-type gaas. *Physical Review Letters*, 80:4313 – 16, 1998.
- [55] B. J. VanWees, L. P. Kouwenhoven, H. Vanhouten, C. W. J. Beenakker, J. E. Mooij, C. T. Foxon, and J. J. Harris. Quantized conductance of magnetoelectric subbands in ballistic point contacts. *Physical Review B*, pages 3625 – 7, 1988.
- [56] D. A. Wharam, T. J. Thornton, R. Newbury, M. Pepper, H. ahmed, J. E. F. Frost, D. G. Hasko, D. C. Peacock, D. A. Ritchie, and G. A. C. Jones. One-dimensional transport and the quantisation of the ballistic resistance. *Journal of Physics C (Solid State Physics)*, 21:L209 – 14, 1988.
- [57] G. Goldoni and A. Fasolino. Band-structure effects on coherent focusing in a two-dimensional hole gas. *Physical Review B*, 44:8369 – 72, 1991.
- [58] K. Ohtsuka, S. Takaoka, K. Oto, K. Murase, and K. Gamo. Distortion of fermi surface induced by parallel magnetic field in a two-dimensional electron gas. *Physica B: Condensed Matter*, 249-251:780 – 783, June 1998.

- [59] V. J. Goldman, B. Su, and J. K. Jain. Detection of composite fermions by magnetic focusing. *Physical Review Letters*, 72:2065 – 8, 1994.
- [60] J. A. Folk, S. R. Patel, K. M. Birnbaum, C. M. Marcus, C. I. Duruoz, and J. S. Harris. Spin degeneracy and conductance fluctuations in open quantum dots. *Physical Review Letters*, 86:2102 – 5, 2001.
- [61] K. J. Thomas, J. T. Nicholls, M. Y. Simmons, M. Pepper, D. R. Mace, and D. A. Ritchie. Possible spin polarization in a one-dimensional electron gas. *Physical Review Letters*, 77:135 – 8, 1996.
- [62] S. M. Cronenwett, H. J. Lynch, D. Goldhaber-Gordon, L. P. Kouwenhoven, C. M. Marcus, K. Hirose, N. S. Wingreen, and V. Umansky. Low-temperature fate of the 0.7 structure in a point contact: a kondo-like correlated state in an open system. *Physical Review Letters*, 88:226805, 2002.
- [63] K. G. Wilson. The renormalization group: critical phenomena and the Kondo problem. *Rev. Mod. Phys.*, 47:773–840, 1974.
- [64] S. M. Cronenwett, T. H. Oosterkamp, and L. P. Kouwenhoven. A tunable Kondo effect in quantum dots. *Science*, 281:540–544, 1998.
- [65] J. Nygard, D. H. Cobden, and P. E. Lindelof. Kondo physics in carbon nanotubes. *Nature*, 408:342 – 346, 2000.
- [66] J. Park, A. N. Pasupathy, J. L. Goldsmith, C. Chang, Y. Yaish, J. R. Petta, M. Rinkoski, J. P. Sethna, H. D. Abruna, P. L. McEuen, and D. C. Ralph. Coulomb blockade and the Kondo effect in single-atom transistors. *Nature*, 417:722 – 725, 2002.

- [67] W. J. Liang, M. P. Shores, M. Bockrath, J. R. Long, and H. Park. Kondo resonance in a single-molecule transistor. *Nature*, 417:725 – 729, 2002.
- [68] A. C. Hewson. *The Kondo problem to heavy fermions*. Cambridge Studies in Magnetism. Cambridge University Press, Cambridge, 1993.
- [69] T. A. Costi and A. C. Hewson. Transport coefficients of the Anderson model via the numerical renormalization group. *J. Physics: Cond. Mat.*, 6:2519–2558, 1994.
- [70] P. Nozières. A “Fermi liquid” description of the Kondo problem at low temperatures. *J. Low Temp. Phys.*, 17:31–42, 1974.
- [71] Y. Matsushita, H. Bluhm, T. H. Geballe, and I. R. Fisher. Evidence for charge Kondo effect in superconducting Tl-doped PbTe. *Physical Review Letters*, 94:157002, 2005.
- [72] U. Wilhelm, J. Schmid, J. Weis, and K. von Klitzing. Experimental evidence for spinless Kondo effect in two electrostatically coupled quantum dot systems. *Physica E*, 14:385 – 90, 2002.
- [73] S. Sasaki, S. Amaha, N. Asakawa, M. Eto, and S. Tarucha. Enhanced Kondo effect via tuned orbital degeneracy in a spin 1/2 artificial atom. *Physical Review Letters*, 93:017205, 2004.
- [74] P. Jarillo-Herrero, J. Kong, H. S. J. van der Zant, C. Dekker, L. P. Kouwenhoven, and S. De Franceschi. Orbital Kondo effect in carbon nanotubes. *Nature*, 434:484 – 8, 2005.
- [75] F. D. M. Haldane. Scaling theory of the asymmetric Anderson model. *Physical Review Letters*, 40:416–419, 1978.

- [76] L. I. Glazman and M. E. Raikh. Resonant Kondo transparency of a barrier with quasilocal impurity states. *JETP Letters*, 47:452–455, 1988.
- [77] D. Goldhaber-Gordon, Jörn Göres, Hadas Shtrikman, D. Mahalu, U. Meirav, and M. A. Kastner. From the Kondo regime to the mixed-valence regime in a single-electron transistor. *Physical Review Letters*, 81:5225, 1998.
- [78] A. Kumar, C. C. Eugster, T. P. Orlando, D. A. Antoniadis, M. J. Kinaret, M. J. Rooks, and M. R. Melloch. Correlation of oscillations in a quantum dot with three contacts. *Applied Physics Letters*, 66:1379 – 81, 1995.
- [79] T. Ihn K. Ensslin D. D. Driscoll A. C. Gossard R. Leturcq, D. Graf. Multi-terminal transport through a quantum dot in the Coulomb blockade regime . *Europhysics Letters*, 67:439 – 445, 2004.
- [80] L. I. Glazman, F. W. J. Hekking, and A. I. Larkin. Spin-charge separation and the Kondo effect in an open quantum dot. *Physical Review Letters*, 83:1830 – 3, 1999.
- [81] S. De Franceschi, R. Hanson, W. G. van der Wiel, J. M. Elzerman, J. J. Wijkema, T. Fujisawa, S. Tarucha, and L. P. Kouwenhoven. Out-of-equilibrium Kondo effect in a mesoscopic device. *Physical Review Letters*, 89:156801 – 1, 2002.
- [82] E. Lebanon and A. Schiller. Measuring the out-of-equilibrium splitting of the Kondo resonance. *Physical Review B*, 65(3):035308 – 4, JAN 2002.
- [83] R. Leturcq, L. Schmid, K. Ensslin, Y. Meir, D. C. Driscoll, and A. C. Gossard. Probing the Kondo density of states in a three-terminal quantum ring. *Physical Review Letters*, 95:126603, 2005.

- [84] E. K. Chan, J. A. Folk, I. L. Chuang, A. A. Houck, J. Labaziewicz. Kondo effect in electromigrated gold break junctions. *cond-mat/0410752*, 2004.
- [85] S. Sasaki, S. De Franceschi, J.M. Elzerman, W.G. van der Wiel, M. Eto, S. Tarucha, and L.P. Kouwenhoven. Kondo effect in an integer-spin quantum dot. *Nature*, 405:764, 2000.
- [86] M. Eto and Y. V. Nazarov. Enhancement of kondo effect in quantum dots with an even number of electrons. *Physical Review Letters*, 85:1306 – 1309, 2000.
- [87] H. Jeong, A. M. Chang, and M. R. Melloch. The kondo effect in an artificial quantum dot molecule. *Science*, 293:2221 – 2223, 2001.
- [88] U. Wilhelm, J. Schmid, J. Weis, and K. von Klitzing. Two electrostatically coupled quantum dots as a realization of the anderson impurity model. *PhysicaE*, 9:625 – 630, 2001.
- [89] U. Wilhelm, J. Schmid, J. Weis, and K. von Klitzing. Experimental evidence for spinless kondo effect in two electrostatically coupled quantum dot systems. *PhysicaE*, 14:385 – 390, 2002.
- [90] P. Jarillo-Herrero, J. Kong, H. S. J. van der Zant, C. Dekker, L. P. Kouwenhoven, and S. De Franceschi. Orbital Kondo effect in carbon nanotubes. *Nature*, 434:484 – 8, 2005.
- [91] S. Sasaki, S. Amaha, N. Asakawa, M. Eto, and S. Tarucha. Enhanced Kondo effect via tuned orbital degeneracy in a spin 1/2 artificial atom. *Physical Review Letters*, 93:017205, 2004.
- [92] A. Georges and Y. Meir. Electronic correlations in transport through coupled quantum dots. *Physical Review Letters*, 82:3508 – 3511, 1999.

- [93] N. J. Craig, J. M. Taylor, E. A. Lester, C. M. Marcus, M. P. Hanson, and A. C. Gossard. Tunable nonlocal spin control in a coupled-quantum dot system. *Science*, 304:565 – 7, 2004.
- [94] N. Andrei and C. Destri. Solution of the multichannel Kondo problem. *prl*, 52:364 – 367, 1984.
- [95] A. Zawadowski. Kondo-like state in a simple model for metallic glasses. *Physical Review Letters*, 45.
- [96] J. M. Maldacena and A. W. W. Ludwig. Majorana fermions, exact mapping between quantum impurity fixed points with four bulk fermion species, and solution of the "unitarity puzzle". *Nuclear Physics B*, B506:565 – 88, 1997.
- [97] J. von Delft, D. C. Ralph, R. A. Buhrman, S. K. Upadhyay, R. N. Louie, A. W. W. Ludwig, and V. Ambegaokar. The 2-channel Kondo model. review of experimental evidence for its realization in metal nanoconstrictions. *Annals of Physics*, 263:1 – 55, 1998.
- [98] M. J. Besnus, M. Benakki, A. Braghta, H. Danan, G. Fischer, J. P. Kappler, A. Meyer, and P. Panissod. Specific-heat and NMR of the Kondo system  $\text{YbPd}_2\text{Si}_2$ . *Journal of Magnetism And Magnetic Materials*, 76-7:471 – 472, 1988.
- [99] K. A. Matveev. Quantum fluctuations of the charge of a metal particle under the Coulomb blockade conditions. *Zhurnal Eksperimental'noi i Teoreticheskoi Fiziki*, 99(5):1598 – 611, 1991.
- [100] K. A. Matveev. Coulomb blockade at almost perfect transmission. *Physical Review B*, 51:1743 – 51, 1995.

- [101] G. Zarand, G. T. Zimanyi, and F. Wilhelm. Two-channel versus infinite-channel Kondo models for the single-electron transistor. *Physical Review B*, 62:8137 – 43, 2000.
- [102] E. Lebanon, A. Schiller, and F. B. Anders. Enhancement of the two-channel Kondo effect in single-electron boxes. *Physical Review B*, 68:155301, 2003.
- [103] Frithjof B. Anders, Eran Lebanon, and Avraham Schiller. Coulomb blockade and quantum critical points in quantum dots. *Physica B: Condensed Matter*, 359-361(SPEC. ISS.):1381 – 1383, 2005.
- [104] F. B. Anders, E. Lebanon, and A. Schiller. Coulomb blockade and non-Fermi-liquid behavior in quantum dots. *Physical Review B*, 70:201306, 2004.
- [105] Y. Meir, N. S. Wingreen, and P. A. Lee. Transport through a strongly interacting electron system: theory of periodic conductance oscillations. *Physical Review Letters*, pages 3048 – 51, 1991.
- [106] J. A. Folk and C. M. Marcus. Decoherence in nearly isolated quantum dots. *Physical Review Letters*, 87:206802/1 – 206802/4, 2001.
- [107] D.J. Thouless. Maximum metallic resistance in thin wires. *Physical Review Letters*, 39:1167, 1977. Scaling theory of localization.
- [108] Yuval Oreg. Private Communication, 2005.
- [109] Leonid Glazman. Private Communication, 2005.
- [110] T. Cichorek, A. Sanchez, P. Gegenwart, F. Weickert, A. Wojakowski, Z. Henkie, G. Auffermann, S. Paschen, R. Knip, and F. Steglich. Two-channel Kondo effect in glasslike ThAsSe. *Physical Review Letters*, 94:236603, 2005.

- [111] In dilute rare earth/actinide alloys, thermodynamic evidence is largely compatible with 2CK, but the inability to reconcile transport data with 2CK theory has left the final state of understanding inconclusive. In the putative atomic two-level system 2CK measured by Ralph *et al.* in narrow metal constrictions [34, 35] and more recently by Cichorek *et al.* in bulk metallic glasses [110], the transport data nicely match the expected scaling behavior, but a fundamental controversy persists about whether the original (near-degenerate but strongly-coupled two-level system) model Hamiltonian can even exist in a real physical system.
- [112] K. Majumdar, A. Schiller, and S. Hershfield. Nonequilibrium Kondo impurity: Perturbation about an exactly solvable point. *Physical Review B*, 57:2991 – 2999, 1998.
- [113] M. H. Hettler, J. Kroha, and S. Hershfield. Nonlinear conductance for the two channel Anderson model. *Physical Review Letters*, 73:1967 – 70, 1994.
- [114] J. von Delft, A. W. W. Ludwig, and V. Ambegaokar. The 2-channel Kondo model. II. CFT calculation of non-equilibrium conductance through a nanoconstriction containing 2-channel Kondo impurities. *Annals of Physics*, 273:175 – 241, 1999.
- [115]
- [116] W. G. van der Wiel, S. De Franceschi, T. Fujisawa, J. M. Elzerman, S. Tarucha, and L. P. Kouwenhoven. The Kondo effect in the unitary limit. *Science*, 289:2105 – 8, 2000.
- [117] A. C. Johnson, C. M. Marcus, M. P. Hanson, and A. C. Gossard. Coulomb-modified Fano resonance in a one-lead quantum dot. *Physical Review Letters*, 93:106803 – 4, 2004.

- [118] K. Le Hur, P. Simon, and L. Borda. Maximized orbital and spin Kondo effects in a single-electron transistor. *Physical Review B*, 69:45326, 2004.
- [119] A. B. Zorin. The thermocoax cable as the microwave frequency filter for single electron circuits. *Review of Scientific Instruments*, 66:4296 – 300, 1995.

# Appendix A

## Wiring and Filtering in Oxford

### TLM Dilution Refrigerator

In this appendix, I present the grounding and filtering scheme used for the measurements at Stanford University. This scheme produced 12mK electron temperature measured by Coulomb blockade thermometry on a *GaAs* based SET.

In Fig. A.1, a simple diagram for the filtering and shielding is presented. All digital electronics, such as the DACs (digital to analog convertor), DMM's (digital multimeter), and computers are located outside the shielded room. The DACs and the computer are connected to an APC UPS (uninterrupted power supply) unit, model 2200. If the power goes out, the UPS will last at least 1 hour with computer, monitor and DACs running.

## A.1 Oxford TLM dilution refrigerator

### A.1.1 Basics

We use a top loading dilution refrigerator with the sample in mixture. The wiring and thermal sinking from 300K to 1K is provided by Oxford. The wires then go through and are potted in a large G10 cylindrical rod separating the mixing chamber from the still, and are terminated in the sample space for the customer to modify. The sample space is in the mixing chamber, however it is immersed in the dilute phase – the phase boundary is not in the sample space. The mixing chamber is made of G10, providing no radiative protection from the 4K main He bath. (This could be corrected, though, if we were to wrap the mixing chamber in Cu tape.) The volume occupied by the sample must be near  $10.25 \text{ in}^3$  for the fridge to function properly.

### A.1.2 Thermometry and temperature control

The refrigerator has several  $RuO_2$  thermometers and resistive wire heaters. The probe has a single  $RuO_2$  thermometer and one heater. Unfortunately, the probe heater tends to short to the cold finger, so all temperature control was accomplished with the mixing chamber heater on the fridge. The probe temperature takes longer to stabilize with this heater, but that is the only disadvantage.

All thermometers were read and all heaters powered by a Lakeshore 370 AC resistance bridge (although it is not really a bridge, it is just a lockin). The external switching box was left outside the shielded room, and the lines coming into the shielded room were filtered with LC  $\pi$  filters in a feedthrough.

For temperature control, we measured the probe resistor and heated with the mixing chamber heater. Because we are not heating the probe locally, the long lag time

Heater Power ( $\mu W$ )	Heater Power ( $\mu W$ )	Temperature (mK)
5 min.	60 min.	
20	10	22
30	15	28
40	25	39
60	35	49
80	55	60

Table A.1: Heater power

involved made PID loops not work for temperature control. However, we noticed the fridge would remain very stable at a temperature with a constant amount of heat applied. The method for changing temperature we adopted was to sit at a heater value for 5 minutes, then switch to a lower heater value. After about 30 minutes, the fridge stabilized to a new temperature. Typical heater values and temperature are shown in table A.1.

## A.2 Electronics and room temperature filtering

### A.2.1 DAC properties

For the DC voltages, we use a normally 20 bit (we have measured 18 1/2 bit resolution) DAC (digital to analog convertor) board – biasDAC – developed by Jim MacArthur, director of the electronic instrument design lab at Harvard University. A single DAC board contains 4 isolated channels - high and low of each channel are isolated from each other and isolated from ground. The DAC board is powered by a floated Acopian

power supply (18V). The DAC receives its commands from the computer (IBM pc running Windows 2000) via a fiber optic cable (using RS232-to-fiber converter from B and B Electronics and fiber cable from Digikey number A11BBC-0201D-ND). In our experiments, we use 12 DAC channels, meaning we have 3 boards housed in separate metal boxes (from Lansing Enclosures). The boxes are electrically connected to the shielded room via grounding straps.

The floated DAC channels of biasDAC allow a very simple and clean grounding design. Unfortunately, they are made with a switching power supply which puts a huge amount of 400kHz and 1.2MHz noise in the system. Most room temperature filtering on the DAC lines is used to specifically filter out this noise. The noise is on both the high and low of the DAC channel. (Note: Inside the DAC board the noise reduces tremendously when the aluminum thermal sink is grounded.)

All BNC cables used in these experiments are stainless steel from Pomona. Stainless steel cables provide minimum triboelectric noise while they are resistive at DC (compared to Cu) and become lossy above 10 KHz (providing additional filtering above that frequency). (Cu coax transmits up to 2GHz.)

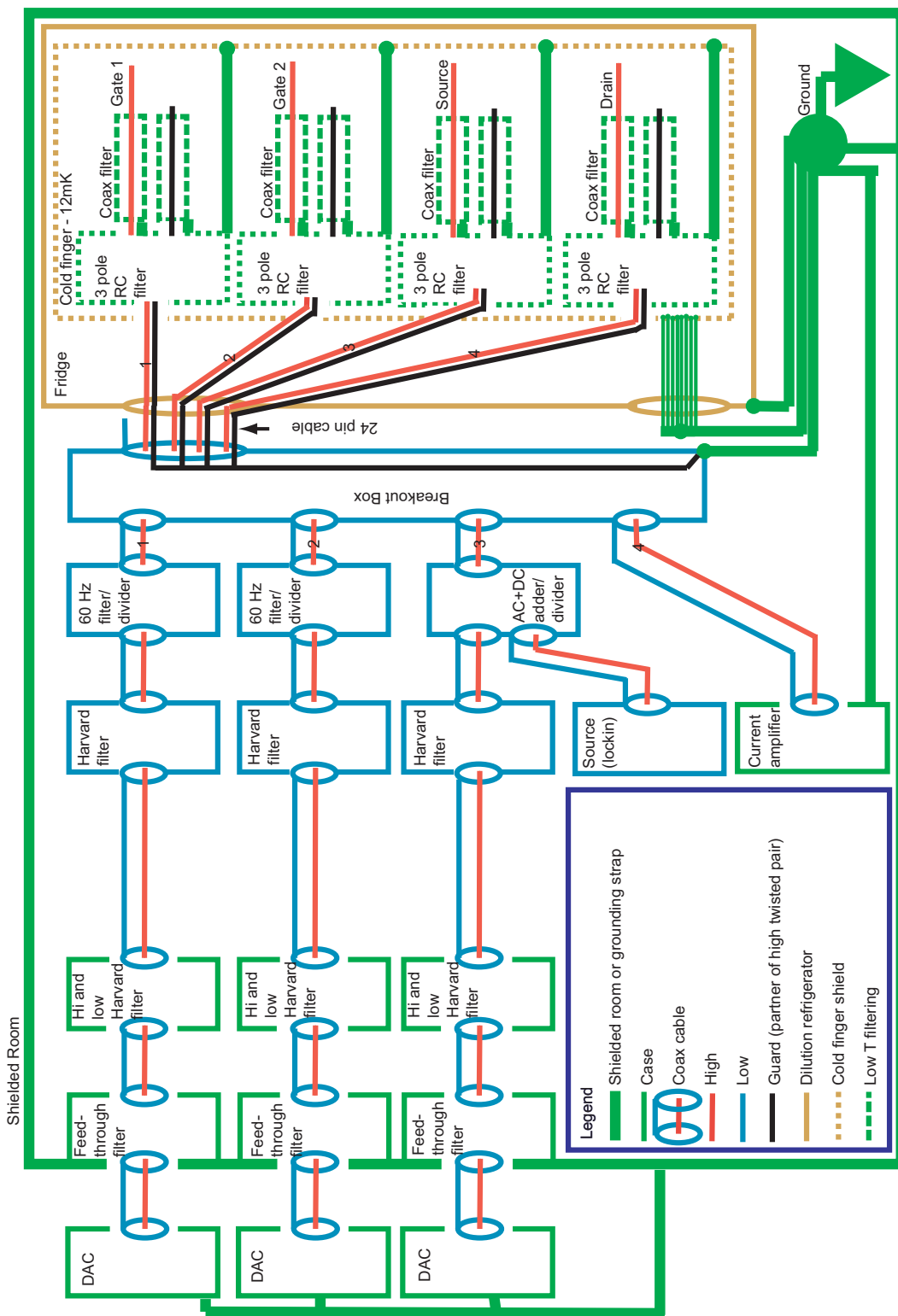


Figure A.1: Circuit diagram for the room temperature wiring and shielding.

In Fig. A.1, the various filtering and grounding elements are shown for both gate lines and the source and drain lines. The low to all DAC channels are eventually connected together are the breakout box and grounded. The system was designed to have no ground loops. Photographs of the setup are shown in Fig. A.2. In Fig. A.2(a), a rack outside the shielded room is shown with 3 DAC units and 2 DMMs. The coax cables then run through the feedthrough with pi filters and into the shielded room.

Once in the shielded room, a second set of filters (the “high and low Harvard filter”, which I have recently learned were developed at Stanford) is used to target the 400kHz and 1.2MHz noise, as shown in Fig. A.2(b). Long BNC cables run from these filters to the rack inside the shielded room (Fig. A.2(c)). In Fig. A.2(d), the high line is filtered and divided on the rack using one Harvard filter and one 60Hz filter. Notice in both Fig. A.2(c) and (d) the cables and filters are fixed in place to reduce triboelectric noise and pickup.

The entire rack is shown in Fig. A.2(e). Once filtered, short cables are used to connect to the breakout box, Fig. A.2(f).

## A.2.2 DAC filtering

In the next section, the components of the various filters from Fig. A.1 will be discussed. The feedthrough filter is shown in Fig. A.3. The feedthrough connects the high and low DAC channel to an isolated BNC. Both high and low pass through pi filters. The pi filter is a 7000pF resin filled bolt in filter from Spectrum Control, part number 51-729-312.

The high and low are then rejoined into an isolated BNC connector. They are immediately connected into another filter which also separates the high and low – the high and low Harvard filter, as shown in Fig. A.4. This filter is based on a design by

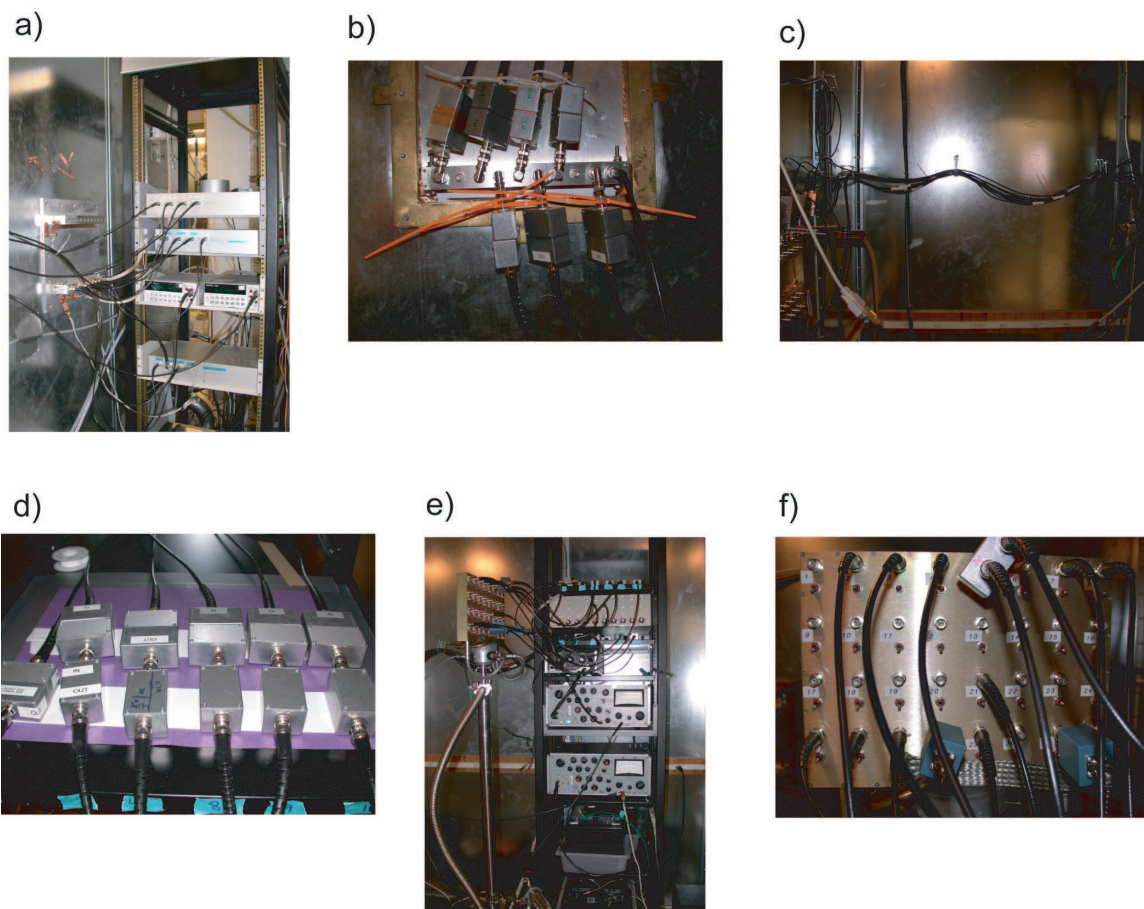


Figure A.2: Photographs of the filters and cables for the DAC lines.

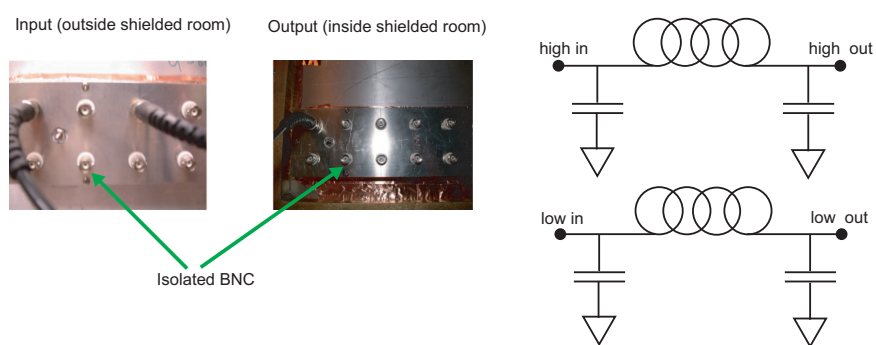


Figure A.3: Feedthrough into the shielded room with filter diagram.  $C = 7000\text{pF}$ .

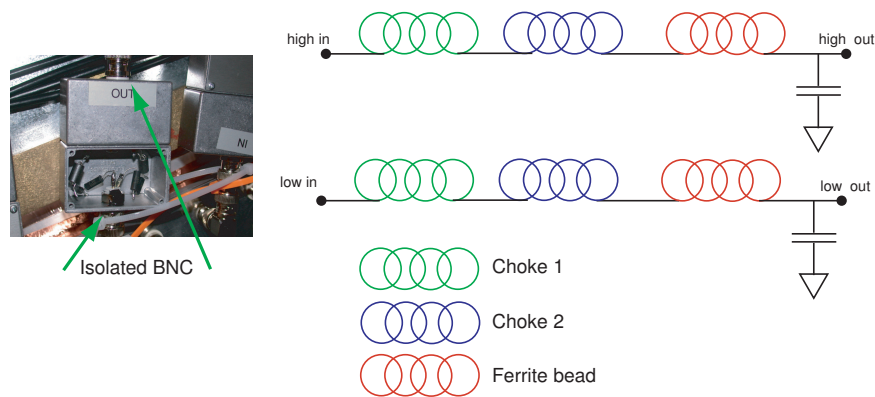


Figure A.4: Harvard filter design to filter both the high and low of the DAC. Choke 1 is  $3300 \mu H$ , choke 2 is  $1000 \mu H$ , and ferrite bead is 2.5 turns.

Brian D’Urso and Jim MacArthur at Harvard University. These filters consist of 2 RF chokes and a ferrite bead, where choke 1 is choke RF molded  $3300\mu H$  ferrite – Digi-Key M9257-ND, choke 2 is choke RF molded  $1000\mu H$  ferrite – Digi-Key M9251-ND, and ferrite bead is a choke wide band 2.5 turn – Digi-Key M2103-ND. The line is then fed through a  $100pF$  capacitor filter feedthrough, Newark part number 90F2269. Both high and low have the same components in this filter.

This filter was needed to filter the low line. Experimentally I found the low line when grounded at the breakout box would make the measurement noisy. I believe the main purpose of this filter is to reflect the  $400kHz$  and  $1.2MHz$  noise from the DAC back to the DAC. However, I have found whenever the BNC is broken out into two wires that are not coaxial, they will pick up  $60Hz$  noise, even in the shielded room. This noise is most likely from inductive or magnetic coupling.

The next set of filters is a Harvard filter on the high line, built the same as mentioned above except the low is now just the outside of the box (non isolated BNCs are used from here on), as shown in Fig. A.5. This is used to completely remove the  $400kHz$  and  $1.2MHz$  noise from the DAC.

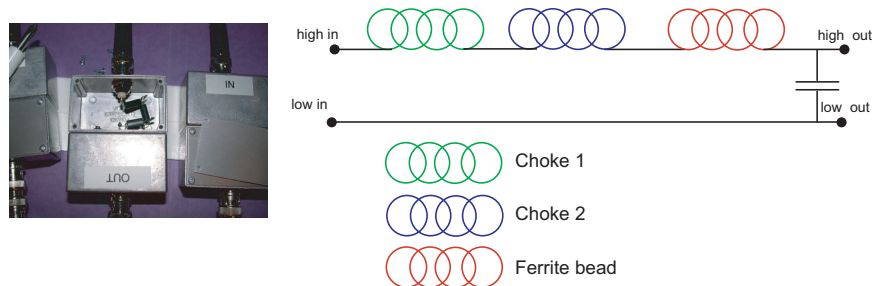


Figure A.5: Harvard filter design to filter high of DAC. Choke 1 is  $3300 \mu H$ , choke 2 is  $1000 \mu H$ , and ferrite bead is 2.5 turns.

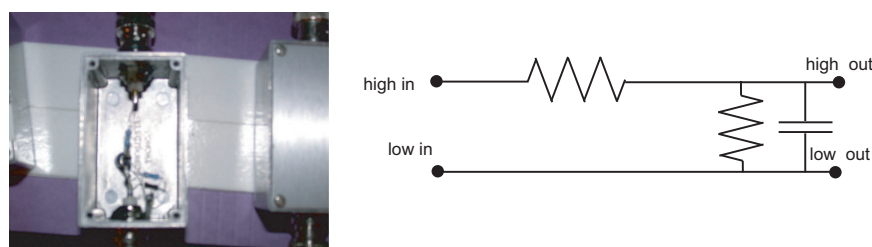


Figure A.6: Divider ( $\sim 1/10$ ) with 60 Hz filter. The divider consists of a  $2.7k\Omega$  resistor and a  $300\Omega$  resistor (both metal film) for a  $\sim 1 : 10$  division. A bipolar capacitor of  $10\mu F$  is used to set a cutoff of  $\sim 18\text{Hz}$ .

Because the filters in Fig. A.3 and A.4 pickup 60Hz, we must filter for 60Hz. In order to keep with the passive filtering trend, I simply attach a low pass RC filter with components  $2.7 \text{ k}\Omega$  and  $10\mu F$  with cutoff frequency of  $\sim 10 \text{ Hz}$ . This slightly limits the speed that the DAC can change voltages on gates. The DAC is also divided by  $\sim 10$  in order to gain resolution. We measured biasDAC to 18 1/2 bit precision over  $\pm 10V$ , which is a minimum step size of  $\sim 30\mu V$ . We improve this step size by dividing by 10, which also divides the noise by a factor of 10. (Voltage noise dominates the noise in this system.)

The DAC channels then plug into the breakout box. Once at the breakout box, all lines, whether gate lines or source drain lines, have the same filtering. So, before

continuing on the breakout box and fridge filtering, the room temperature measurement circuit (source and drain lines) is explained.

### A.2.3 Measurement electronics

In Fig. A.7, photographs of the measurement setup (inside shielded room rack) are shown. The measurement setup consists of a PAR124a lockin amplifier, which also contains a voltage source, shown in Fig. A.7(b). The current in the circuit is then amplified by a DL Instruments 1211 amplifier, as shown in Fig. A.7(c).

The PAR124a is the only equipment in the shielded room that is powered by ac from the wall socket. Although many of the input and output BNC on the PAR124a are isolated, every low is connected to the chassis of the PAR124a. To avoid ground loops, the 124a ground wire is cut as it enters the wall outlet (plugged in through a deadman). This should only be done with great care. The only ground connection for the 124a chassis is then through the voltage source output low. When the source is connected to the breakout box, the outer conductor of BNC is grounded, and thus the chassis is grounded. (There is 60Hz pickup in the amplifier due to the transformer of the 124a. In the future, I hope the transformer will be removed and placed on a different side of the shielded room or the 124a can be powered by battery.)

In order to have control of dc bias voltage also, one DAC channel (channel 0) is added to the ac signal through a passive circuit, shown in Fig. A.8. The AC is divided by  $10^5 : 1$  and has a high pass filter with corner frequency of  $\sim 10Hz$ . The dc divider depends on the resistance of the 60Hz filter before it (on DAC0 there is a  $14k\Omega$  resistor on the 60 Hz filter and no divider, making a  $1060:1$  divider –  $(39k\Omega + 14k\Omega):50\Omega$ ). The dividing is kept track of in the computer in the IngotDAC procedure. I recommend calibrating whenever you change any component in the system.

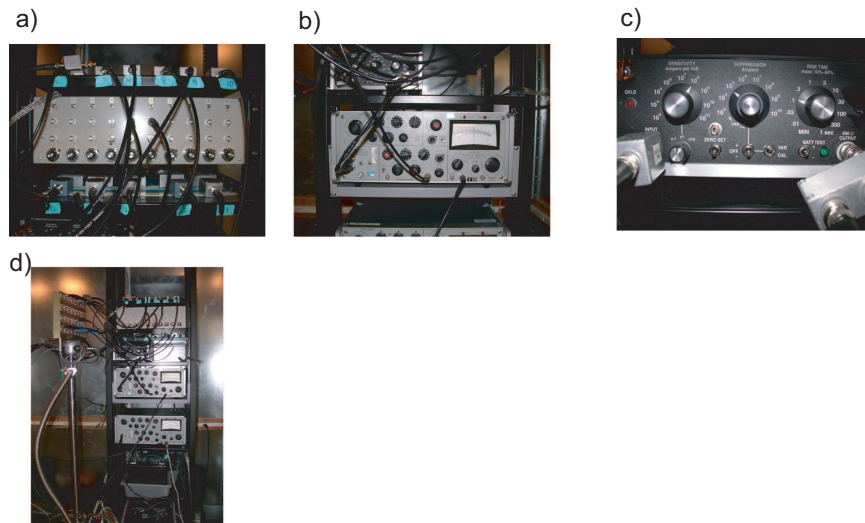


Figure A.7: Photographs of measurement circuit.

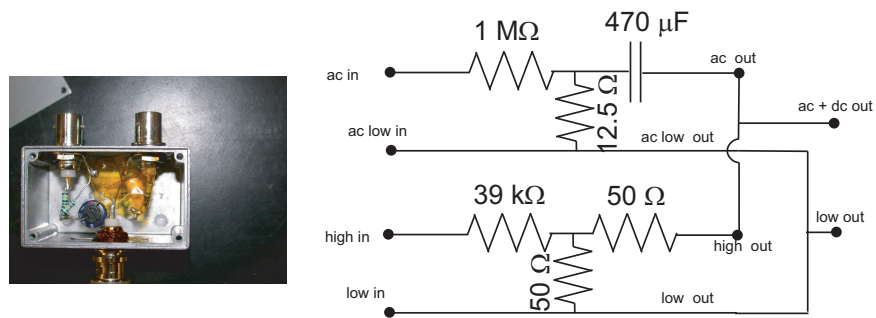


Figure A.8: Passive AC + DC adder box.

The source is then connected to the breakout box. A DL Instruments 1211 amplifier connects to the drain of the measurement, as shown in Fig. A.7(c). The amplifier has factory modification 105, which allows for external battery ( $\pm 12\text{V}$ , and  $0\text{V}$ ) and the ability to finely tune the voltage bias offset. (For any current amplifier, there is a slight ( $\sim \mu\text{V}$ ) voltage offset between the high and low input.) We power the 1211 with two deep cycle 12V batteries (85 A·h deep cycle marine lead acid batteries). In addition, the 1211 is designed to have input low and output low common, and they have a  $10\Omega$  resistance to chassis. We cut that  $10\Omega$  resistor, floating input and output low from the chassis. The 1211 chassis is then grounded to the shielded room by a grounding strap. The 1211 input low (and thus output low) is grounded when it is connected to the breakout box. Finally, the output of the 1211 is split into the inner conductor of two BNC cables and fed into a differential amplifier (A-B) on the 124a lockin. The shields of these BNC cables are not electrically connected to the 1211, but are at the same potential as the chassis of the 124a (no ground loops).

It is worth noting the batteries for the 1211 remain stable for approximately 2 weeks. Any change in voltage of the batteries effects the ( $\sim \mu\text{V}$ ) voltage bias across the input high and low (we will call input voltage). We measure the input voltage by shorting the input leads through a resistance of  $50k\Omega$  (grounding the low side with a grounding strap produces a more stable measurement). Then measure the output of the amplifier with a DC voltmeter. Zero the input voltage with the potentiometer on the 1211, which can be zeroed to better than  $1\mu\text{V}$ .

When a battery is fully charged ( $\sim 13\text{V}$ ), the input voltage drifts as the battery voltage gets rid of its initial high charge state. In order to avoid this, we do fully charge the battery with an Associated 9014 10/2 amp 6/12 volt battery charger. The battery should be charged on the slow charge for a long time (5 hrs or so) – 2A setting (this

dramatically increases the number of times the battery can be charged). As mentioned above, the battery will charge to a high charge state ( $\sim 13V$ ), which will decay to  $\sim$  a very stable 12.6 to 12.3V over time. In order to make the battery quickly decay to a stable voltage, we short the battery out through  $120 \Omega$  and measure the current. (I usually hook two batteries in series and short them simultaneously.) When the current is stable over time (around 0.2A, stable current will take about 40min - 1hr of discharge) disconnect the circuit. The voltage on the batteries should be  $\sim 12.6$  to 12.3V. When the battery has drained, the input voltage bias on the 1211 will again start to drift dramatically. This occurs around  $V_{battery} \sim 12V$  to 11.8V. Disconnect the battery and recharge when this occurs. The batteries tend to not recharge fully if you discharge to below 11.6V, so be careful so as not to waste the batteries.

Measurement wires and DAC wires are then connected to the breakout box, where the low to each channel is shorted together (see Figs. A.1 or A.2). The breakout box is then grounded through a single very large braided grounding strap. The strap is connected to the breakout box via a C-clamp (first the area of electrical connection is sanded) and to the shielded room ground via a large bolt, washer and nut. This is the ground in the system.

#### **A.2.4 Breakout box**

The breakout box is made out from an RF tight box from Compac Development, part S59012. The high of each wire has three possibilities: bus, float and ground, selected by a C and K switch, part E103SYZQE - I have found these switches have very little electrolytic action. (This is a problem with some switches.) The wiring for the high of each wire is shown in Fig. A.9.

At the breakout box, each high wire has another wire twisted with it, forming a

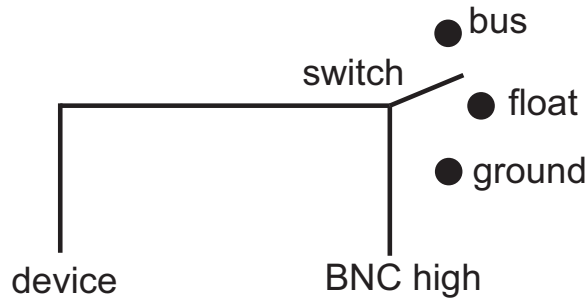


Figure A.9: Wiring in the breakout box. Effectively, the switch is now make before break (device is never floated when something is hooked up to the BNC).

twisted pair. The extra wire is grounded at the breakout box, then continues with the high wire to the bottom of the fridge (where it is left floated). This wiring may have two benefits. First, the spare wire acts like a partial shield for capacitively coupled noise (effectively, it is a grounded shield with  $\sim 50\%$  coverage). Secondly, the spare wire will act like a filter similar to the distributed coax filter, discussed below.

A short (1 ft) cable connects the breakout box to the Oxford refrigerator. The cable is double shielded 24 twisted pair from Belden Cable, with 24pin Fischer connectors on each end.

### A.2.5 Shielding at room temperature

The shielded room is the measurement circuit's main protection from capacitively coupled and radiative noise sources. Although the environment inside the shielded room is expected to be very quiet for electric fields and electromagnetic radiation, we should not expect the shielding to help with low frequency magnetically coupled noise. The coax cable provides the main protection inside the shielded room from magnetic pickup (minimize loop area). Unfortunately, in this setup we break out of perfect coax cables in the filter boxes, which do pickup noise at 60Hz. Furthermore, we currently

also have one transformer (large inductance) in the shielded room (PAR124a), which could be removed to further reduce noise.

## **A.3 Low temperature wiring and filtering**

### **A.3.1 Oxford wiring**

The Oxford probe contains four looms of sample wires, each containing 24 constantan wires of 0.1mm diameter (12 twisted pairs). The resistance of each wire is  $\sim 200\Omega$ , and there is  $245\text{ pF}$  capacitance between two wires in a twisted pair and  $90\text{ pF}$  capacitance between a wire and the probe (with the other twisted pair left floated; I did not measure with the other twisted pair grounded, the experimental situation). The wires are thermally sunk at 1K, then are potted into a G10 block which leads to the mixing chamber.

Inside the mixing chamber, I switch the wires to 0.003in (3 mil) twisted pair phosphor bronze wire. This wire is used for the connection to the pc board filters and then from the coax filters to the chip socket. All solder used is no clean solder with an organic flux that burns off when heat is applied.

### **A.3.2 PC board mounted RC filters**

The pc board filters are 3 pole RC filters designed to filter from 1 MHz to 5GHz. In order to keep in line resistance low, the resistance of each pole is chosen to be  $200\Omega$ . The resistors were metal film 0402 size from Susumu Company. At high frequency, capacitive shorts form across all metal film resistors I found. However, Susumu has data on their 0402 size resistors showing impedance stays nearly constant to 5 GHz.

The capacitances of the poles were 100pF, 10pF, and 1pF, respectively, with the

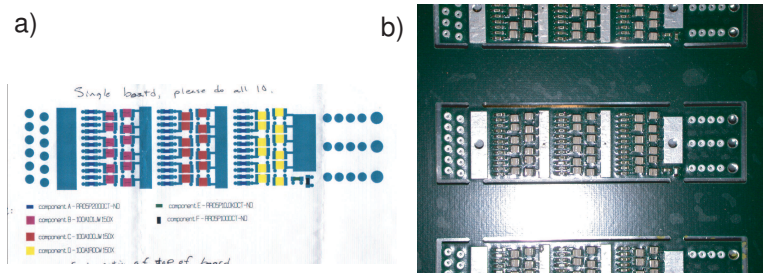


Figure A.10: Three pole RC filter on 4 layer PC board. In (a), a schematic of the top layer is shown. The second layer is a ground plane, the third layer contains the traces and the fourth layer is another ground plane. In (b), a photograph of the filter is shown.

1pF capacitance being the final pole. We use capacitors from American Technical Ceramics, 100pF part no 100A101JW150X, 10pF part no 100A100JW150X, 1pF part no 100A1R0CW150X. All are ceramic capacitors with NPO dielectric, which does not become ferroelectric at low temperature. Capacitors have stray inductances, which in turn lead to resonances in the filters. The 100pF cap has a series resonance of 1GHz, 10pF cap has a series resonance of 2GHz, and the 1pF cap has a series resonance of 9GHz.

In Fig. A.10, a schematic and photograph of the pc board filter is shown. The pc board is a four layer G10 (FR4) board, with the top layer containing copper, solder, and soldermask for the components, the second layer is a copper ground plane, the third layer contains copper traces and the fourth layer is another copper ground plane. The board was made by 4PCB.com, who I found to have excellent technical support (I highly recommend them).

In Fig. A.11, the attenuation (dBm) of the filter as a function of frequency at room temperature is shown. A BNC connector was soldered on the pc board input and output so a frequency generator and spectrum analyzer could be connected. The three traces show different shielding for the filter. Almost all frequency spikes can be

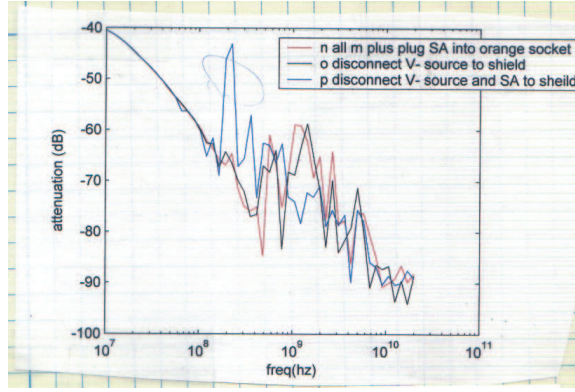


Figure A.11: Attenuation of three pole RC filter on 4 layer PC board as a function of frequency. The three different curves show different shielding schemes.

removed by proper shielding. (The resistance and capacitance did not change by more than 10% at 77K). Although the filter properties were not directly measured at low temperature.

### A.3.3 Resistive coax filters

From the pc boards, the lines enter resistive coax filters, designed to filter high frequency by acting like lossy transmission lines. A transmission line is predicted to be lossy when the skin depth  $d_s$  is smaller than the conductor,

$$d_s = \left( \frac{2\rho_{i,o}}{\mu\mu_0\omega} \right)^{0.5}, \quad (\text{A.1})$$

where  $\rho_{i,o}$  is the resistivity of the inner or outer conductor and  $\omega$  is the frequency. As the frequency increases, the wave will be able to propagate inside less area of the inner conductor, which increases the resistance of the conductor A[119],

$$r(\omega) = \left[ \left( \frac{1}{\pi d_1} \frac{\mu\mu_0\rho_i}{2} \right)^{0.5} + \left( \frac{1}{\pi d_2} \frac{\mu\mu_0\rho_o}{2} \right)^{0.5} \right] \omega^{0.5}, \quad (\text{A.2})$$

where  $d_1$  and  $d_2$  are defined in Fig. A.12. Using a resistivity of CuNi of  $3.9 \times 10^{-7} \Omega \cdot m$  for both inner and outer conductor, we find the attenuation as a function of frequency

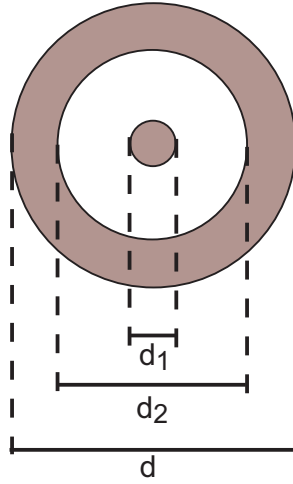


Figure A.12: Lossy coax cable for high frequency filtering. For our cable,  $d_1 = 0.081\text{mm}$ ,  $d_2 = 0.27\text{mm}$ , and  $d = 0.4\text{mm}$ , and the length is  $2\text{m}$ . The insulator is PTFE and the conductors are made of CuNi (70:30).

is

$$A(\nu) = 5.8 \times 10^{-4} \nu^{0.5} \text{ dB/m}. \quad (\text{A.3})$$

Other parameters of the coax cable are  $C = 94.78\text{pF/m}$  and characteristic impedance of  $50.22\Omega$ , and a dc resistance of the inner conductor of  $77\Omega/\text{m}$ . The cables were purchased from Coax Corporation, Japan, through the exporters Alahlam Limited in Ibaraki, Japan – contact Chikako Yamanouchi.

The attenuation of these cables was tested by soldering SMA connectors on each end and measuring transmission and reflection with a network analyzer. At room temperature, the coax were found to match both specifications and theory from 50MHz to 20GHz. Specifications for this cable are shown in table A.2

Frequency (GHz)	Attenuation (dB/m)
0.5	12
1	17
5	38
10	54
20	76

Table A.2: Attenuation of resistive coax

### A.3.4 Chip carrier and socket and the presence of magnetic materials

The chip carrier and socket are custom made to contain no magnetic materials (socket pins are made of uncoated beryllium copper). The sockets were manufactured by Plastronics and the carriers were manufactured by Kyocera. The sockets and carriers have 32 pins. The pinouts for the wires of the fridge are shown in table A.3.

Notice wires 6, 14, 22, and 30 have strange resistance values. This is because I designed these wires with low temperature (1:100) dividers on the pc boards. We never successfully had the low temperature divider work for experiments, but we did not try very hard.

In the dilution refrigerator in Charlie Marcus's lab, we noticed a Coulomb blockade peak would increase in width when the magnetic field was swept through 0T. We then replaced all magnetic materials in the refrigerator and the sample ohmic contacts with nonmagnetic metals. With this modification, we no longer observed CB peak width increasing when the magnetic field moved through 0T.

Pin number	Oxford loom number: high wire, low wire	shorted chassis-pin	chassis-pin	high-pin	high-cf	low-cf	low-pin
1	3:1,2	10	10	$\infty$	$\infty$	960	960
2	3:3,4	1924	$\infty$	960	$\infty$	960	$\infty$
3	3:5,6	1924	$\infty$	960	$\infty$	960	$\infty$
4	3:7,8	1924	$\infty$	960	$\infty$	960	$\infty$
5	3:9,10	1924	$\infty$	960	$\infty$	960	$\infty$
6	3:11,12	393	422	11000	11000	960	1060
7	3:13,14	1930	$\infty$	960	$\infty$	960	$\infty$
8	3:15,16	1930	$\infty$	960	$\infty$	960	$\infty$
9	3:17,18	1930	$\infty$	960	$\infty$	960	$\infty$
10	3:19,20	1930	$\infty$	960	$\infty$	960	$\infty$
11	3:21,22	1930	$\infty$	960	$\infty$	960	$\infty$
12	3:23,24	1930	$\infty$	960	$\infty$	960	$\infty$
13	2:1,2	dead	$\infty$	dead	$\infty$	960	$\infty$
14	2:3,4	429	431	11000	11100	960	1000
15	2:5,6	dead	$\infty$	dead	$\infty$	960	$\infty$
16	2:7,8	1930	$\infty$	960	$\infty$	960	$\infty$
17	2:9,10	1930	$\infty$	960	$\infty$	960	$\infty$
18	2:11,12	dead	$\infty$	dead	$\infty$	960	$\infty$
19	2:13,14	1930	$\infty$	960	$\infty$	960	$\infty$
20	2:15,16	1930	$\infty$	960	$\infty$	960	$\infty$
21	2:17,18	1930	$\infty$	960	$\infty$	960	$\infty$
22	2:19,20	426	427	11000	11100	960	1060
23	2:21,22	1930	$\infty$	960	$\infty$	960	$\infty$
24	2:23,24	1930	$\infty$	960	$\infty$	960	$\infty$
25	1:1,2	1930	$\infty$	960	$\infty$	960	$\infty$
26	1:3,4	1930	$\infty$	960	$\infty$	960	$\infty$
27	1:5,6	1930	$\infty$	960	$\infty$	960	$\infty$
28	1:7,8	1930	$\infty$	960	$\infty$	1047	$\infty$
29	1:9,10	1930	$\infty$	990	$\infty$	960	$\infty$
30	1:11,12	429	$\infty$	10970	11070	960	1060
31	1:13,14	1930	$\infty$	960	$\infty$	960	$\infty$
32	1:15,16	1930	$\infty$	960	$\infty$	960	$\infty$

Table A.3: Wiring of dilution refrigerator

In the Stanford refrigerator, we have nonmagnetic chip carrier and socket. However, many of the wiring components contain magnetic materials. The CuNi coax are not ferromagnetic, but they are paramagnetic. Also, many of the components of the pc board have nickel barriers to their solder terminations. We have not yet investigated the consequences of these magnetic materials on the measurements.

### **A.3.5 Shielding in the refrigerator**

All filtering at low temperature is housed inside a copper tube. We call the copper tube a cold finger, but since the entire cold finger is emersed in mixture, it is really just a radiation shield. Since  $200\text{MHz} = 10\text{mK}$ , we wanted the radiation shield many skin depths thick. This is easily accomplished using  $3/32$  inch copper.

Mixture must flow through the coldfinger, so the coldfinger is not made perfectly radiation tight. However, the input and exit to the coldfinger are bent tubes, designed to allow easy liquid flow but greatly inhibit radiation below optical frequencies.

The coldfinger is screwed into a G10 block of the probe, so it does not have any electrical connection to the rest of the cryostat. (Also, the mixing chamber is also made of G10, so there is no chance of accidental electrical touches). We ground the coldfinger (and thus the low of some of the filtering at low temperature) through 24 constantin wires (Oxford Instruments wire loom). The resistance of the loom of 24 wires is  $\sim 10\Omega$ . The optional resistance of a ground wire would be lower.

### **A.3.6 Building the coldfinger**

This section shows how the wiring was accomplished. First, the pcboards were soldered by L-tronics, as shown in Fig. A.13(a). Each pc board filters 6 wires (6 high and 6 low). In order to conserve space, the pc boards are mounted on a brass pentagon piece,

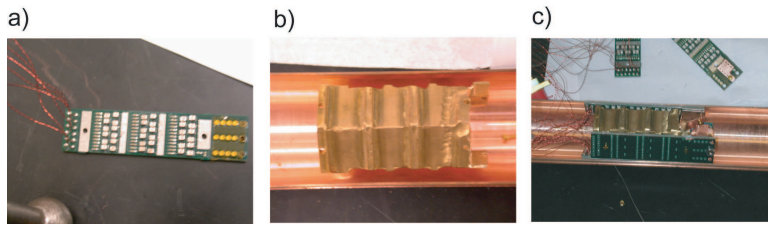


Figure A.13: PC board and the pentagon.

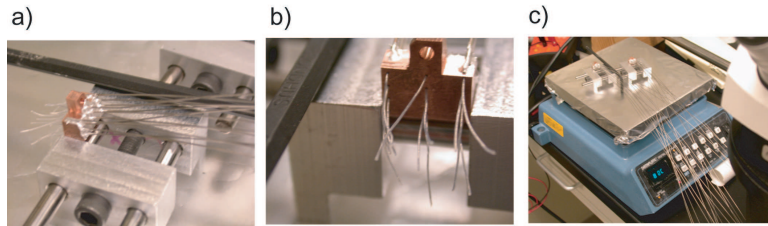


Figure A.14: Making connectors for the coaxial cables.

shown in Fig. A.13(b). As six boards are needed, five are mounted on the sides of the pentagon and the sixth is mounted inside the pentagon. This arrangement is shown to be possible in Fig. A.13(c).

In Fig. A.14, the connectors for the coaxial connectors to the pc boards are shown. The outer conductor fits halfway through the Cu block and is epoxied into place using silver epoxy from Epotek. We cure the epoxy at moderate temperature to speed the process, however not too high temperature for the PTFE to absorb a significant amount of water.

In Fig. A.15, the copper connector is attached to the pc board. The inner conductor of each wire is then soldered to the back side of the pc board.

Once the coaxial cables and pc boards are connected, they are mounted on the pentagon, as shown in Fig. A.16. The coaxial cables do not bend very much coming out of the copper connector.

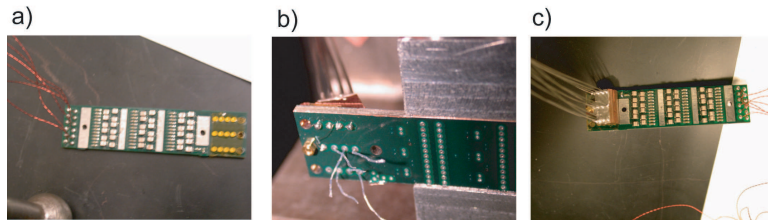


Figure A.15: Attaching the coax to the pc board.

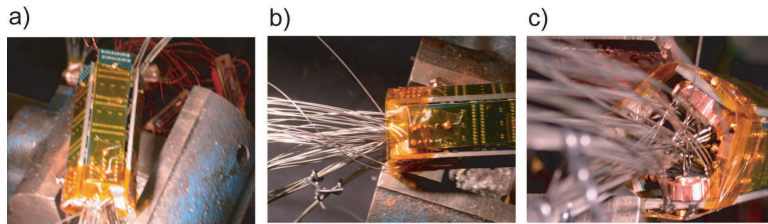


Figure A.16: PC boards mounted with the coaxial cables attached mounted on the pentagon. The coax do not have to turn to sharply to exit the pc board mount.

Once the coaxial cables leave the pc board, they are wound noninductively around a copper tube filled with copper mesh, as shown in Fig. A.17. Once the coax are wrapped into a small volume, connectors similar to the input connectors are used to break out of the coax and into a phosphor bronze wire. The phosphor bronze wire then attaches to the chip socket.

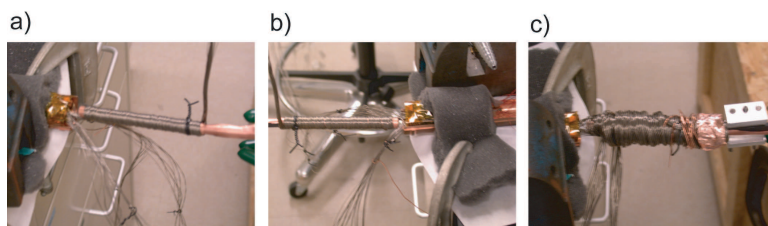


Figure A.17: Wrapping the coaxial cable noninductively into a small volume.

### A.3.7 Measurement details

In this section, a remaining measurement details are provided. When measuring the two channel Kondo effect, the typical impedance is between  $12k\Omega$  and  $1M\Omega$ . This large range makes choosing the sensitivity of the lockin and current amplifier somewhat difficult. We found the optimal amplification for the DL Instruments current amplifier to be  $10^8V/A$ . At this sensitivity, the input impedance of the amplifier is  $2k\Omega$ . The lockin amplifier could then be set to  $10mV$  sensitivity setting, which puts  $10mV$  on a  $10V$  scale, or 1:1000 voltage amplification.

The analog signal was then fed into an Agilent or HP 34401 DMM. This DMM was set to the -2 speed setting (fast), and we digitally sampled the DMM by the computer between 10 and 100 times for each data point. Averaging in the computer gained about 10% in signal to noise compared with the averaging function in the DMM.

At base temperature, we use  $1\mu V$  ac excitation for the conductance measurements. However, the voltage is applied across the sample and the filtering, wiring, and current amplifier. The low temperature wiring and filters have approximately  $1900\Omega$  of resistance (once down the fridge and back up again). The inline resistance is accounted for in software to extract the correct differential conductance.

The lines also have capacitance, which affects the response function of the fridge. Using a simplified (first order) model of the fridge in Fig. A.18, we determine that the fridge has a cutoff frequency of about  $2kHz$ . All measurements were taken below  $337Hz$ . Above this frequency at moderate device impedance ( $500k\Omega$ ), the phase of the signal was observed to deviate from perfectly in-phase. All measurements were made with input voltage and output (current) voltage in phase with each other. At  $337Hz$ , we minimized noise and maximized speed of measurement with the a DL Instruments 1211 risetime set to  $0.3ms$ , the lockin risetime of  $100ms$ , and the lockin  $Q = 50$ .

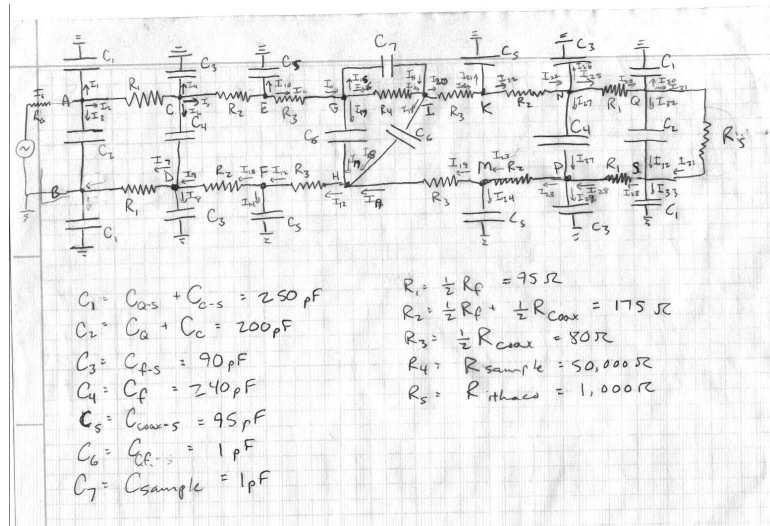


Figure A.18: First order model of measurement circuit to calculate circuit response function.

### A.3.8 Coulomb blockade thermometry

In this section, we demonstrate temperature of three Coulomb blockade peaks. We measure three different Coulomb blockade peaks from a small quantum dot ( $\Delta < kT$ , for all  $T$ ) as a function of temperature in Fig. A.19. Both CB width and height behave in the expected manner as a function of temperature.

## A.4 Appendix references

A[1] Zorin, A.B., “The thermocoax cable as the microwave frequency filter for single electron circuits”, Rev. Sci. Instrum. **66**, 4296 (1995).

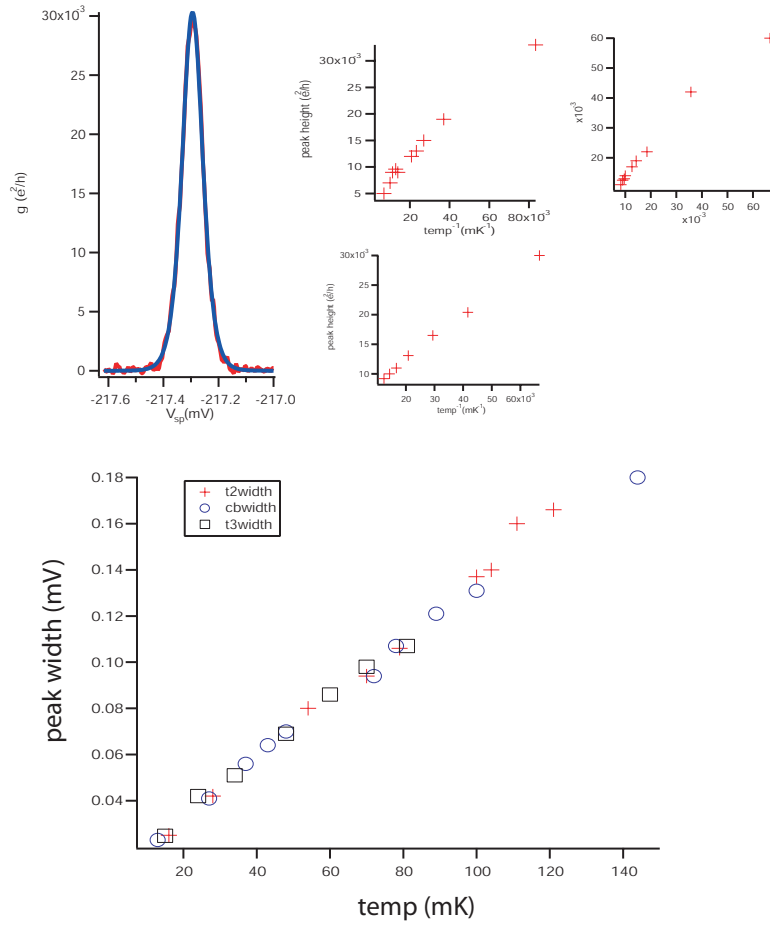


Figure A.19: Coulomb blockade peak width and height as a function of temperature.